Geometry synthesis and multi-configuration rigidity of reconfigurable structures

Thesis by
Charles Dorn

In Partial Fulfillment of the Requirements for the
Degree of
Doctor of Philosophy

CALIFORNIA INSTITUTE OF TECHNOLOGY
Pasadena, California

2022
Defended September 13, 2021

Charles Dorn
ORCID: 0000-0001-6516-2586

ACKNOWLEDGEMENTS

First and foremost, I would like to thank my advisor, Professor Sergio Pellegrino. His guidance was always inspiring, but never rigidly structured, giving me a high degree of freedom to shape my own research interests. I would also like to thank my defense and candidacy committee: Professors Kaushik Bhattacharya, Chiara Daraio, and Ravi Ravichandran. Their feedback after my candidacy helped form my research.

I would like to thank the AFOSR for providing the funding through a MURI grant that made this research possible (award number FA9550-18-1-0566 directed by Dr. Ken Goretta). I am grateful to the members of the MURI team for their feedback and collaboration, especially Robert Lang, whose incredible intuition and mastery of origami helped drive the direction of this research, and Elliott Williams, who was an amazing and enthusiastic collaborator.

I would like to thank my colleagues in the Space Structures Lab for creating a supportive and enjoyable environment. Yang Li's mentorship through the beginning of my PhD got me excited about origami and helped set the scene for my PhD research. Michael Marshall has been a great friend and colleague throughout, who was always open to discuss research ideas. A special thanks is needed to Uba Ubamanyu, Fabien Royer, Alex Wen, and Thibaud Talon, who never hesitated to offer help in the lab when I needed it. Finally, thanks to the rest of the lab for the continuous feedback and support: Brayden Aller, Gianfranco Canales, Meital Carmi, Anjini Chandra, Luke Chen, Sahangi Dassanayake, Liz De La Torre, Serena Ferraro, Terry Gdoutos, Armanj Hasanyan, Christophe Leclerc, Andrew Lee, Wen Luo, John Pederson, Antonio Pedivellano, Ozair Rajani, Harsha Reddy, Charles Sommer, Alan Truong, and Yuchen Wei.

I also want to thank the GALCIT and Caltech staff, including Christine Ramirez, Kate Jackson, Peggy Blue, Jamie Meighen-Sei, Petros Arakelian, Ali Kiani, and Paul Stovall.

I had the wonderful opportunity to spend my second year of graduate school as an exchange student at École Polytechnique; I would like to thank Nick Triantafyllidis for making this experience possible, as well as Kostas Danas and Laurence Bodelot for their mentorship.

Also, I would like to thank my past mentors, Yongchao Yang and David Mascarenas, who were the ones that first exposed me to academic research and ultimately inspired me to pursue a PhD.

I couldn't have made it through without the support from my friends, especially through the struggles of the pandemic. A special thanks goes out to Jeremy Bernstein, Phillip Buelow, Ashish Goel, Ludo Gil, Rory Williams, Pat Dowd, Joey O'Neill, and Jason O'Neal.

Finally, I would like to thank my Mom and Dad, my sisters Claire and Rachel, Nana and Papa, and Elizabeth for their support and encouragement to pursue my passions.

ABSTRACT

Reconfigurable structures are structures that can change their shapes to change their functionalities. Origami-inspired folding offers a path to achieving shape changes that enables multi-functional structures in electronics, robotics, architecture and beyond. Folding structures with many kinematic degrees of freedom are appealing because they are capable of achieving drastic shape changes, but are consequently highly flexible and therefore challenging to implement as load-bearing engineering structures. This thesis presents two contributions with the aim of enabling folding structures with many degrees of freedom to be load-bearing engineering structures.

The first contribution is the synthesis of kirigami patterns capable of achieving multiple target surfaces. The inverse design problem of generating origami or kirigami patterns to achieve a single target shape has been extensively studied. However, the problem of designing a single fold pattern capable of achieving multiple target surfaces has received little attention. In this work, a constrained optimization framework is presented to generate kirigami fold patterns that can transform between several target surfaces with varying Gaussian curvature. The resulting fold patterns have many kinematic degrees of freedom to achieve these drastic geometric changes, complicating their use in the design of practical load-bearing structures.

To address this challenge, the second part of this thesis introduces the concept of multi-configuration rigidity as a means of achieving load-bearing capabilities in structures with multiple degrees of freedom. By embedding springs and unilateral constraints, multiple configurations are rigidly held due to the prestress between the springs and unilateral constraints. This results in a structure capable of rigidly supporting finite loads in multiple configurations so long as the loads do not exceed some threshold magnitude. A theoretical framework for rigidity due to embedded springs and unilateral constraints is developed, followed by a systematic method for designing springs to maximize the load-bearing capacity in a set of target configurations. An experimental study then validates theoretical predictions for a linkage structure. Together, the application of geometry synthesis and multi-configuration rigidity constitute a path towards engineering reconfigurable load-bearing structures.

PUBLISHED CONTENT AND CONTRIBUTIONS

[1] C. Dorn, R. Lang, and S. Pellegrino, "Kirigami tiled surfaces with multiple configurations," *In preparation*.
C. Dorn conducted the research and wrote the manuscript.

[2] C. Dorn, Y. Li, and S. Pellegrino, "Structures with multiple rigid configurations due to prestress and unilateral contacts," in *International Design Engineering Technical Conferences and Computers and Information in Engineering Conference*, ASME, 2021.
C. Dorn conducted the research and wrote the manuscript.

[3] D. E. Williams, C. Dorn, S. Pellegrino, and A. Hajimiri, "Origami-inspired shape-changing phased array," in *50th European Microwave Conference (EuMC)*, IEEE, 2021. DOI: 10.23919/EuMC48046.2021.9338189.
C. Dorn designed and fabricated the mechanical part of the prototype.

TABLE OF CONTENTS

Chapter 1

INTRODUCTION

1.1 Motivation

There is a fundamental relationship between the shape of a structure and its function. Reconfigurable structures are a class of structure capable of transforming their shape to achieve multiple functions. The ability to change shape is a powerful concept that enables structures to adapt to different operating conditions or manipulate their properties on demand.

An incredibly broad range of applications is enabled by reconfigurable structures spanning many engineering disciplines. In aerospace engineering, the geometry of airplane components, such as wings and engine inlets, drives their functionality. Thus, reconfigurable components allow aerodynamic properties to be tailored to different flight conditions [1–3]. An example of a variable camber wing concept is shown in Figure 1.1a. In architecture, active facades can reconfigure for efficient thermal management in buildings [4], shown in Fig. 1.1b. Robots can benefit from shape changes to fit into small spaces [5], shown in Figure 1.1c, and reconfigurable wheels can adapt to the terrain [6]. Reconfigurable structures in electronics enable optical sensors with adaptive focusing [7, 8] and antennas that can manipulate their radiation pattern through shape change [9]. While this list is far from exhaustive, it highlights the role of reconfigurable structures as an enabling technology across many fields.

1.2 Concepts in reconfigurable structures

Echoing the wide range of applications, there are many approaches for achieving reconfigurable structures. However, there are common requirements that must be addressed by all reconfigurable structures. Generally, a reconfigurable structure must satisfy the following:

1. Geometry: the structure can achieve a set of desired *target configurations*.
2. Stiffness: the structure can hold its target configurations under loading.
3. Reconfigurability: the structure can be actuated between the target configurations.

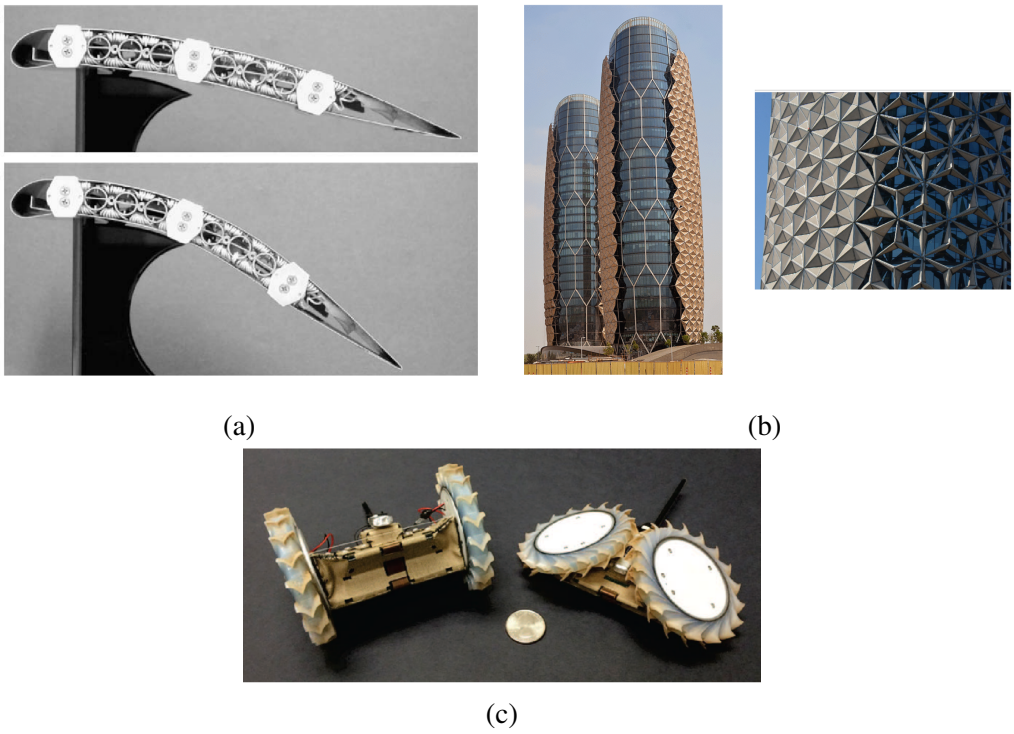

Figure 1.1: Examples of reconfigurable structures enabling multi-functionality through geometric changes. (a) Variable camber wing concept [10]. (b) Adaptive facade of the Al Bahar towers in Abu Dhabi (photos courtesy of Terri Boake). (c) NASA JPL's Puffer robot [5].

The first requirement is that the geometry of the structure can achieve a desired set of target configurations, which are driven by the application at hand. Concepts for achieving reconfiguration fall on a spectrum from smooth deformations of continuous structures to localized deformations of discrete structures. In continuous structures, target geometries are achieve through smooth deformations, for example in morphing shell structures [11] and soft robotic actuators [12]. On the other end of the spectrum, discrete structures exploit localized deformations at joints or hinges to achieve geometric changes. Variable geometry trusses, for example, can change shape through deformation localized at pin-joints [13, 14]. Another prominent concept for discrete reconfigurable structures is origami, where a network of flat plates connected by hinges exhibits localized deformation at the hinges [15]. Finally, there is a spectrum between continuous and discrete, where there are both localized and smooth deformations. This occurs, for example, in origami-inspired structures with smooth folds [16, 17] or truss structures with deformable beams [18].

The second requirement is stiffness in each target configuration, which allows each configuration to maintain its shape under loads. In any application, load-bearing capacity is relevant, though the level of stiffness required highly depends on the application. A morphing wing must withstand aerodynamic loads, so its target configurations must be sufficiently stiff. On the other hand, a soft robot may be less concerned with load-bearing capacity. Regardless, the target configurations must be maintained under some external loading, and stiffness is a crucial aspect of reconfigurable structures.

The third requirement for reconfigurable structures is the ability to reconfigure between target configurations. An actuation scheme must be capable of changing the geometry between the target configurations. Actuation concepts range from discretely placed actuators to continuously distributed actuation. Discrete actuators apply forces or displacements at a set of points throughout the structure, and can be used alongside continuous [11] or discrete [13, 14] structural geometries. Alternatively, distributed actuation can be achieved through active materials that induce deformations throughout a structure, which is the case in the morphing wing of Figure 1.1a.

These three requirements unite the many concepts in reconfigurable structures and also highlight why the design of reconfigurable structures is a difficult task. The challenge of reconfigurable structures stems from the contradiction between requirements. The ability to deform between different target configurations requires geometric freedom, which is synonymous with flexibility, contradicting the requirement of stiff target configurations.

This thesis is motivated by the challenge of developing reconfigurable structures that are load-bearing, easily reconfigured, and have substantial geometric freedom. We address these challenges in the context of a particular reconfigurable structures problem: a reconfigurable surface.

1.3 Reconfigurable surfaces

A particularly interesting and challenging reconfigurable structures problem is to create a morphing surface that can change its Gaussian curvature. Changes in Gaussian curvature require *metric-changing* geometric transformations, meaning that lengths along the surface change.

Reconfigurable surfaces enable a range of applications, from adaptive optical sensors [7, 8] to architecture [15]. One appealing application is morphing phased array

antennas, which provides inspiration for the research in this thesis. Phased arrays are arrays of antennas that collectively produce a desired radiation pattern. Traditional phased arrays have fixed geometry. However, the ability to change the shape of a phased array surface offers a means of adapting its electromagnetic properties. For example, properties such as field of view and gain can be manipulated by changing curvature. This enables antennas with multiple operating shapes, each with different properties [19].

Motivated by the high potential for application, the geometry and mechanics of reconfigurable surfaces is an emerging research area that has recently gained popularity, largely in response to recent advances in manufacturing technology. Many concepts for achieving curvature change have been explored, ranging from continuous to discrete approaches.

One approach for curvature change is to deform a continuous surface. However, changing the Gaussian curvature of a continuous surface requires stretching and therefore a soft material capable of stretching. Programmable stretching to achieve curvature change has been explored [20] and has proven useful for applications such as optical sensors [21]. Figure 1.2a shows an elastomer membrane supporting optical sensors that can stretch from a flat to hemispherical surface when pressurized.

Alternatively, discrete grids of deformable elements offer a path to reconfigurable surfaces that avoid pure stretching. Examples include grids of elastomer strips [22] (shown in Figure 1.2b) or beams [23–25], as well as architected sheets with non-periodic cut patterns [26–28]. Multi-stability offers a promising approach for achieving stiffness in multiple target configurations and simplified actuation between configurations. Examples of bi-stable reconfigurable surfaces can be found in [29] (Figure 1.2c) along with [27, 30]. However, the load-bearing capacity of multi-stable surfaces is often overlooked and may not be scalable to support large loads in engineering applications.

Finally, origami and its variants such as kirigami, which allows holes, offer a path to reconfigurable surfaces through folding. Inspired by the ancient art of origami, flat sheets can be folded into extraordinarily complex 3D shapes. Curvature-changing transformations are possible by origami-inspired folding concepts, which provides an approach for reconfigurable surfaces [32]. Figure 1.2d show an example of a fold pattern, which is a generalization of Resch's origami pattern [31], capable of folding from flat sheet into a spherical surface.

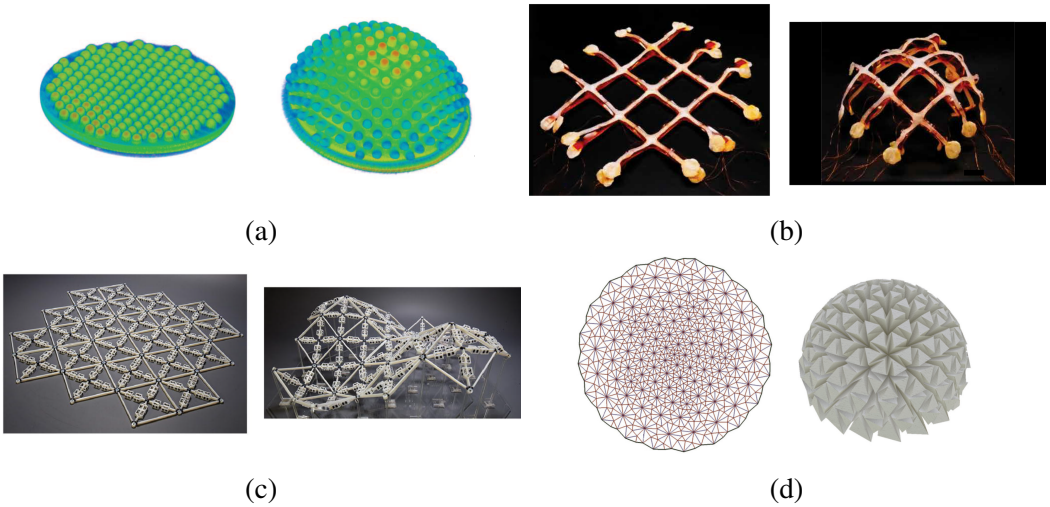

Figure 1.2: Concepts for reconfigurable surfaces. (a) X-ray tomography image of an elastomeric morphing surface that changes curvature through stretching [21]. (b) Robotic surface composed of stretchable liquid crystal elastomer strips [22]. (c) Multi-stable reconfigurable surface based on bi-stable units [29]. (d) Generalization of Resch's origami pattern [31].

Among the many concepts that have been explored to achieve curvature change, there is no single approach that is the most effective towards applications. In the emerging research area of reconfigurable surfaces, several concepts have shown potential to enable curvature change, motivating research to carry these concepts towards engineering applications where load-bearing capacity is essential. Towards maturing the collective knowledge of reconfigurable structures, metrics must be developed to assess the load-bearing capacity, which would represent a step towards designing reconfigurable surfaces for engineering applications. This thesis focuses on origami-inspired folding concepts as a means for curvature change and develops optimal design methodology and metrics for load-bearing capacity that advance the state of folding structures.

1.4 Curvature change through folding

Folding has emerged as a powerful concept for achieving curvature change. The geometry of curvature change through folding has been a prominent topic of research as origami has evolved into an engineering tool [32]. While folding itself is an isometric transformation (no stretching occurs) that cannot change the intrinsic curvature of a sheet, apparent curvature can be created where a subset of faces or vertices of a fold pattern approximate a curved surface. However, the application of folding surfaces as engineering structures is a major challenge that requires further

research into the mechanics of folding structures, particularly towards developing understanding and design methodology for achieving load-bearing capacity.

Rigid-folding origami and kirigami patterns, which are comprised of rigid faces connected by hinges, can be classified as having a single kinematic degree of freedom (DOF) or having multiple degrees of freedom. Single-DOF fold patterns, such as the Miura-ori [33], fold along a one-dimensional kinematic path (though there may be multiple branches of one-dimensional kinematic paths [34]). Single-DOF folding structures are appealing because they are easy to reconfigure, which is useful in practical applications [6, 35]. Multiple approaches have been developed for designing single-DOF fold patterns that can fold from flat sheets into a curved target surface [36–38]. However, single-DOF fold patterns are limited to configurations along a one-dimensional kinematic path. Thus, a flat sheet can be folded into a single curved surface, but achieving multiple surfaces with varying curvature is a challenge for single-DOF patterns.

Alternatively, multi-DOF fold patterns can take on a range of configurations within a multi-dimensional configuration space. Multi-DOF fold patterns capable of curvature change were explored in the early work of Resch [39, 40]. Subsequently, design tools have been developed to synthesize multi-DOF fold patterns capable of achieving arbitrary curved surfaces [31, 41, 42]. Multi-DOF patterns have the ability to achieve a range different curved surfaces with varying curvature [32], though previous research has not addressed the inverse problem of designing a single fold pattern to fold into multiple curved target surfaces. Achieving multiple target surfaces with the same fold pattern is highly appealing for applications that could exploit several different operating configurations.

Multi-DOF patterns are extremely appealing from the geometric perspective due to their potential to transform between a set of shapes with varying curvature. However, due to their high flexibility, a profound challenge is presented to apply multi-DOF fold patterns as engineering structures that can support loads and be easily reconfigured, which provides motivation for the research presented in this thesis.

1.5 Research goals and layout of thesis

This thesis develops a framework for designing reconfigurable folding structures with many kinematic degrees of freedom. Towards this overall goal, there are two research objectives. The first is to create a single fold pattern capable of achieving

multiple target surfaces with varying curvature, which is approached by exploiting the geometric freedom of multi-DOF fold patterns. The second objective is to achieve load-bearing capacity in multi-DOF structures, which is approached by embedding springs and unilateral constraints. Towards these objectives, this thesis presents two contributions that together provide a path to realizing multi-DOF fold patterns as engineering structures:

1. **Geometry synthesis of kirigami surfaces**
   An optimal design framework is presented to synthesize kirigami patterns that can take on *multiple* surfaces with varying Gaussian curvature.

2. **Multi-configuration rigidity**
   The concept of multi-configuration rigidity is developed, where a structure is held rigidly in multiple configurations due to prestress between embedded springs and unilateral constraints.

The first contribution of kirigami pattern synthesis is significant because origami and kirigami patterns are typically synthesized to fold from a flat sheet to a single three-dimensional target shape. In this work, a novel optimization-based framework to design kirigami patterns capable of achieving multiple target surfaces is presented. The resulting kirigami patterns exhibit the ability to transform between a set of surfaces with varying Gaussian curvature, but in turn they have many kinematic degrees of freedom. This introduces the challenge of how to reconfigure between target configurations and support loads in each target surface configuration.

To address the challenges associated with high kinematic freedom, the concept of multi-configuration rigidity is introduced, where the prestress between embedded springs and unilateral constraints rigidly holds a set of target configurations. Such configurations are initially rigid, capable of supporting finite loads without displacement. Upon the application of a load above some critical magnitude, the prestress is overcome and the structure can move. Multi-configuration rigidity offers a solution for introducing load-bearing capacity to structures with many kinematic degrees of freedom. Additionally, it offers a path to simplified actuation since each rigid configuration corresponds to a local energy minimum on the kinematic boundary introduced by the unilateral constraints, though the focus of this thesis is on load-bearing aspects and actuation is not studied.

The thesis is organized as follows:

Chapter 2 introduces geometry synthesis and multi-configuration rigidity through a set of introductory examples. The purpose of this chapter is to build intuition and understanding through examples. A prototype of a morphing kirigami antenna surface provides a proof-of-concept for multi-configuration rigidity, which motivates and provides direction for the research presented in the remainder of the thesis.

Chapter 3 formulates a geometry synthesis framework for kirigami surfaces that can take on multiple configurations. It is exemplified by generating a fold pattern capable of reconfiguring between six target surfaces with varying Gaussian curvature, which is realized in a physical prototype. The challenge posed by these patterns are their high number of kinematic degrees of freedom, which motivates the study of multi-configuration rigidity in subsequent chapters.

Chapter 4 proceeds to develop theoretical formulations for rigidity due to unilateral constraints and embedded springs. A lower bound on the load-bearing capacity of a rigid configuration is derived, which provides a quantitative metric to assess load-bearing capacity. This lower bound enables a systematic design process to achieve multi-configuration rigidity where load-bearing capacity is maximized in each configuration. This chapter is presented in the context of statically determinate unilateral constraints.

Chapter 5 further develops the theory and design methodology by extending the results of Chapter 4 to the statically indeterminate case. This allows for the design of multi-configuration rigidity in large structures with many unilateral constraints. This chapter culminates with an example of designing a reconfigurable surface with 18 degrees of freedom, whose geometry is generated in Chapter 3, to have two rigid configurations with maximal load-bearing capacity.

Chapter 6 presents an experimental study of a linkage that has multiple rigid configurations. Experiments are performed to measure the load-bearing capacity of rigid configurations, which validates analytical predictions for critical forces. Additionally, parameter uncertainty is shown to play a significant role in influencing load-bearing capacity, prompting a Monte Carlo analysis to quantify the effects of parameter uncertainty.

Finally, Chapter 7 concludes the thesis. The key contributions of this work are summarized and paths to future research are discussed.

Chapter 2

INTRODUCTORY EXAMPLES

Research presented in this chapter has been adapted from the following publication:

C. Dorn, Y. Li, S. Pellegrino, "Structures with multiple rigid configurations due to prestress and unilateral contacts," *ASME IDETC*, 2021.

2.1 Introduction

This chapter provides an example-focused introduction to the two core topics of this thesis: geometry synthesis of kirigami surfaces and multi-configuration rigidity. First, an intuitive overview of the concept of multi-configuration rigidity is presented, followed by an example of a single degree of freedom (DOF) linkage. Then, we present the design of a reconfigurable kirigami surface that has 24 kinematic degrees of freedom to have two rigid configurations, allowing it to support loads in each rigid configuration and to be easily reconfigured. The geometry synthesis and multi-configuration rigidity design of the 24-DOF surface follows a simplified, intuition-based process as a proof-of-concept that shapes the remainder of the thesis.

Multi-configuration rigidity is defined as when a structure with one or more internal mechanisms is made rigid in multiple configurations due to the prestress between embedded springs and unilateral constraints. In each rigid configuration, finite loads can be supported without causing displacement, but loads above some critical magnitude will overcome this prestress to move the structure.

Multi-configuration rigidity is particularly appealing for origami-inspired structures with many internal mechanisms, defined as the degrees of freedom of the structure. Practical application of origami is often limited to patterns with single or low-DOF, such as the Miura-ori [33] and other quadrilateral mesh patterns [36] since they can be reconfigured easily. However, the geometry of low-DOF structures is inherently limited by their low dimensional configuration space. In contrast, many-DOF patterns such as Resch's pattern [40], as well as the kirigami patterns synthesized in Chapter 3, have many kinematic degrees of freedom, allowing remarkable geometric changes to be achieved.

Many-DOF structures are alluring for engineering applications due to their geometric versatility, but actuation can be prohibitively complex [43]. The "brute

force" actuation strategy of simultaneously controlling a number of actuators equal to the DOFs of the structure is impractical to physically implement for many-DOF patterns. Active materials show promise for actuating many-DOF patterns, which might utilize thermal or electrical stimuli to locally activate folding [44–47], but are suited for smaller scale applications without significant load-bearing capabilities. Another approach for reconfiguring many-DOF structures is through multi-stability, as proposed in [48]. Springs are embedded throughout a structural mechanism, and the spring parameters are designed such that each target configuration corresponds to a stable equilibrium configuration. The actuation of a multi-stable structure is straightforward since transferring between stable configurations can easily be achieved. However, it may be difficult to achieve high stiffness in all stable configurations of a multi-stable structure.

Multi-configuration rigidity is different from multi-stability. Whereas multi-stable structures have analytical (smooth) energy minima at each stable configuration, in multi-configuration rigidity the kinematic boundary introduced by the unilateral constraints introduces a sharp local energy minimum for each rigid configuration. Multi-configuration rigidity offers key advantages compared to multi-stability, such as the ability to resist finite perturbation loads without significant deflection (theoretically, zero deflection).

The idea of utilizing unilateral constraints to aid in structural reconfiguration has been previously considered to control shape changes in many-DOF metamaterials [49]. Contact has been used to simplify reconfiguration of a linkage [50], and also rigidity of structures due to contact is found in bio-inspired structures such as scales [51]. Furthermore, insightful parallels can be drawn to concepts in the robotic grasping literature [52, 53], which aims to immobilize objects using unilateral contact.

To introduce multi-configuration rigidity through examples, in this chapter we study a single-DOF linkage and a 24-DOF kirigami surface. The single-DOF linkage example is presented to build intuition for the concept of multi-configuration rigidity and to draw distinctions from multi-stability. Then, a 24-DOF kirigami surface is considered by first presenting the geometry synthesis of the fold pattern. Then, through an intuitive design process, springs and unilateral contact are placed throughout the pattern to achieve two rigid configurations. A prototype of the pattern is constructed, which is outfitted with antenna tiles to create a morphing phased array antenna to demonstrate a practical application. This complex example

provides a proof of concept, showcasing that multi-configuration rigidity is a powerful tool for designing many-DOF structures that are both load-bearing and easy to reconfigure. This provides motivation for subsequent chapters that present a general geometry synthesis framework for kirigami surfaces and develop a rigorous theory for multi-configuration rigidity.

2.2 Interpretations of multi-configuration rigidity

Two interpretations of multi-configuration rigidity are provided by a robotic grasping analogy and by considering a ball moving on a hill, in two dimensions. These interpretations are generalized to higher dimension in Section 2.4 in the context of a 24-DOF structure.

The first interpretation considers a robotic grasping problem, which is useful in understanding how a single configuration is immobilized by contact. Figure 2.1a shows an object grasped by three frictionless unilateral constraints. Since the force F is present and pushes into the constraints, contact with the constraints is maintained and the object is immobilized. This is referred to as *force closure* in the grasping literature [52]. Force closure occurs when an external force acts to maintain contact with unilateral constraints to immobilize an object (note that the precise definition of force closure varies in the literature [53, 54]). When subjected to a perturbing force, the object will not move unless the perturbing force has an upward vertical component larger than F, and is thus rigid up to some finite perturbation. This grasping analogy offers a useful interpretation of structural rigidity from unilateral constraints, where F is analogous to the force in the springs, which pushes against the unilateral constraints to block any possible motion.

A second interpretation is the classical "ball on a hill" analogy, shown in Figure 2.1b, where the walls represent the unilateral constraints. Points A and C are local minima with respect to kinematically admissible positions that respect the unilateral constraints, corresponding to the hill sloping into the wall. If a perturbation force is applied to the ball, it will not move unless the weight of the ball is overcome by the force. Thus, points A and C identify two rigid configurations. In contrast, point B is a smooth local energy minimum, which corresponds to a stable equilibrium configuration.

2.3 Single-DOF example

This section presents a simple single-DOF linkage that is designed to achieve rigidity in two target configurations. Consider the four-bar linkage shown in Figure 2.2 with

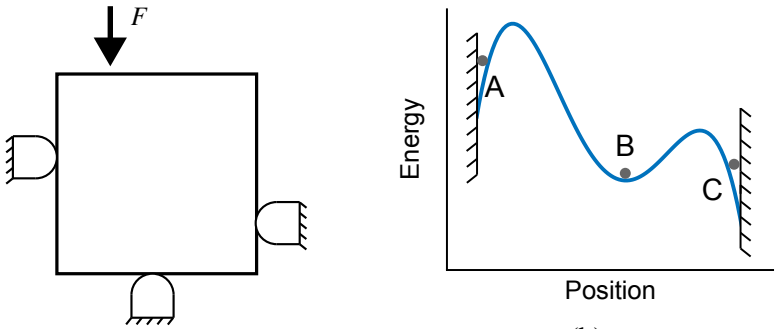

(a) (b)

Figure 2.1: Interpretations of rigidity due to unilateral constraints. (a) Object grasping analogy. The square is in *force closure*, immobilized due to contact with unilateral constraints, which is maintained due to the force F. (b) Ball on a hill analogy. Points A and C are held rigidly due to contact with the wall, while Point B is a stable equilibrium position.

bar lengths $AB = 0.8$, $BC = 1.16$, $CD = 1.3$, and $AD = 0.95$. This linkage itself represents the *skeleton* structure, which is kinematically indeterminate with one degree of freedom. The kinematics can be described in terms of a single variable, which will be taken as θ_A. An analytical relation between θ_D and θ_A, from [55], is given by

$$\theta_D = \pi - \arctan\left(\frac{A_2}{A_1}\right) \pm \arccos\left(\frac{-A_3}{\sqrt{A_1^2 + A_2^2}}\right), \tag{2.1}$$

where

$$A_1 = 2AB \cdot CD \cos\theta_A - 2AD \cdot CD \tag{2.2}$$

$$A_2 = 2AB \cdot CD \sin\theta_A \tag{2.3}$$

$$A_3 = AD^2 + CD^2 + AB^2 - BC^2 - 2AB \cdot AD \cos\theta_A. \tag{2.4}$$

The kinematic path in the space of θ_A and θ_D is plotted in Figures 2.3a and 2.4a. The two configurations shown in Figure 2.2 are taken as target configurations. The first target configuration has angles $\theta_A = -191°$ and $\theta_D = 90°$ while the second has $\theta_A = 83°$ and $\theta_D = 90°$. Note that positive values of θ_A and θ_D are shown in Figure 2.2b. Linear torsion springs of stiffness κ are introduced on joints A and D. The moments m_A and m_D in the two springs are given by

$$\begin{aligned} m_A &= -\kappa(\theta_A - \theta_A^0) \\ m_D &= -\kappa(\theta_D - \theta_D^0), \end{aligned} \tag{2.5}$$

where θ_A^0 and θ_D^0 are the rest angles of the two springs. The energy stored in the springs is

$$E = \frac{1}{2}\kappa\left(\theta_A - \theta_A^0\right)^2 + \frac{1}{2}\kappa\left(\theta_D - \theta_D^0\right)^2. \tag{2.6}$$

The rest angles of the springs constitute the two design variables in the problem, which can be designed to make the structure have two rigid (Section 2.3.1) or stable (Section 2.3.2) configurations. Since both springs have the same stiffness, the value of the stiffness does not affect the shape of the energy landscape and only acts as a scaling factor.

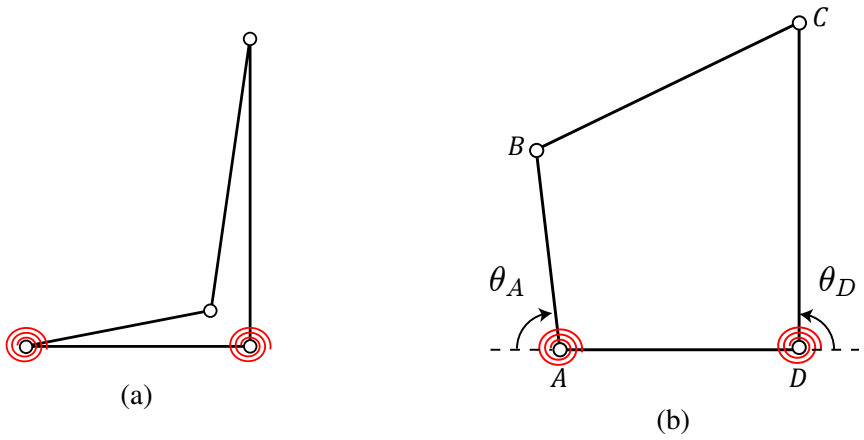

Figure 2.2: Four bar linkage geometry with torsion springs on A and D shown in red. (a) Target configuration 1 with $\theta_A = -191°$ and $\theta_D = 90°$. (b) Target configuration 2 with $\theta_A = 83°$ and $\theta_D = 90°$.

2.3.1 Multi-configuration rigidity

To achieve multi-configuration rigidity, we introduce a unilateral constraint to restrict the angle θ_D such that

$$90° - \theta_D \leq 0. \tag{2.7}$$

This constraint is *active* ($\theta_D = 90°$) in both target configurations. That is, both configurations lie on the boundary of the kinematically admissible configurations. Associated with this unilateral constraint is a reaction moment μ. The problem at hand is to design the rest angles of the torsion springs such that both target configurations are rigid due to contact with the 90° stop. Conditions for rigidity in each configuration can be derived through an equilibrium analysis.

The equilibrium conditions in the presence of constraints can be obtained using the principle of virtual work. The work of the springs through virtual angular displacements $\delta\theta_A$ and $\delta\theta_D$ is $m_A\delta\theta_A + m_D\delta\theta_D$. The work associated with the unilateral constraint is $\mu\delta\theta_D$, where μ is the reaction moment of the unilateral constraint. A compatible angular displacement must obey $\delta\theta_D = \frac{d\theta_D}{d\theta_A}\delta\theta_A$, where $\frac{d\theta_D}{d\theta_A}$ is computed by differentiating Eq. (2.1). The principle of virtual work requires the work of the springs to equal the work of the unilateral constraint, leading to

$$\left(m_A + m_D\frac{d\theta_D}{d\theta_A}\right)\delta\theta_A + \mu\frac{d\theta_D}{d\theta_A}\delta\theta_A = 0. \tag{2.8}$$

This must hold generally for any nonzero $\delta\theta_A$, which leads to the equilibrium equation

$$m_A + m_D\frac{d\theta_D}{d\theta_A} + \mu\frac{d\theta_D}{d\theta_A} = 0. \tag{2.9}$$

Additionally, the following conditions associated with the unilateral constraint must be satisfied:

$$\mu \geq 0 \tag{2.10}$$

$$\mu(\theta_D - 90^\circ) = 0. \tag{2.11}$$

Collectively, Eqs. (2.9)-(2.11) are known as the Karush-Kuhn-Tucker conditions [56]. Equation (2.9) represents a moment balance and (2.10) enforces the condition that the contact moment in the unilateral constraint must be non-negative. Finally, Eq. (2.11) requires that μ can only be nonzero if there is contact with the constraint, known as complementary slackness.

Examining Eq. (2.11), if $\mu > 0$, then θ_D must remain equal to 90° and the structure is rigid. To achieve multi-configuration rigidity, we seek values of θ_A^0 and θ_D^0 that correspond to a positive μ in both target configurations. Solving for μ in Eq. (2.9) and requiring its positivity yields

$$\mu = -\left(m_A + m_D\frac{d\theta_D}{d\theta_A}\right)\left(\frac{d\theta_D}{d\theta_A}\right)^{-1} \tag{2.12}$$

$$= \kappa\left(\theta_A - \theta_A^0 + \left(\theta_D - \theta_D^0\right)\frac{d\theta_D}{d\theta_A}\right)\left(\frac{d\theta_D}{d\theta_A}\right)^{-1} > 0. \tag{2.13}$$

Enforcing $\mu > 0$ in both target configurations leads to a system of two linear inequalities restricting θ_A^0 and θ_D^0. The solution to this system is the blue shaded

region in Figure 2.3a. Designing the rest angles in this region leads to rigidity in both target configurations.

The energy profile along the kinematic path corresponding to $\theta_A^0 = 0$ and $\theta_D^0 = -180°$, a design in the blue shaded region of Fig. 2.3a, is plotted in Figure 2.3b. Each target configuration is a sharp energy minimum, lying on the boundary of the kinematically admissible domain.

An alternative approach to the rigidity of this linkage is obtained by considering a perturbing moment acting on the structure. A rigid configuration can resist perturbing moments without any displacement, up to some finite value of the perturbation when contact is lost. Consider, for example, a counterclockwise perturbation moment $\tilde{M}_A$ applied at point A in target configuration 1. The moment balance accounting for the perturbing moment becomes

$$m_A + m_D \frac{d\theta_D}{d\theta_A} + \tilde{\mu} \frac{d\theta_D}{d\theta_A} + \tilde{M}_A = 0, \tag{2.14}$$

where $\tilde{\mu}$ is the reaction moment after the perturbing moment is applied. Solving for $\tilde{\mu}$ gives

$$\tilde{\mu} = -\left(m_A + m_D \frac{d\theta_D}{d\theta_A} + \tilde{M}_A\right)\left(\frac{d\theta_D}{d\theta_A}\right)^{-1} = \mu - \tilde{M}_A \left(\frac{d\theta_D}{d\theta_A}\right)^{-1}. \tag{2.15}$$

Here, μ is the reaction force in the absence of the perturbation from Eq. (2.12).

Assuming that the rest angles fall within the blue region of Figure 2.3a, μ is positive. Therefore, since $\frac{d\theta_D}{d\theta_A}$ is positive in configuration 1, as long as $\tilde{M}_A < \mu \frac{d\theta_D}{d\theta_A}$, the reaction $\tilde{\mu}$ is positive and θ_D must remain at 90°. In other words, the structure can rigidly resist perturbation moments up to a finite magnitude.

2.3.2 Distinction from multi-stability

It is important to distinguish between multi-configuration rigidity and multi-stability. The two concepts are similar in the sense that they both correspond to the presence of multiple local energy minima. However, multi-stability corresponds to smooth energy minima away from kinematic boundaries while multi-configuration rigidity corresponds to boundary energy minima. Due to this difference, multi-configuration rigidity has key advantages when compared to multi-stability, which can be exemplified by studying the 4-bar linkage.

We aim to compute the rest angles that lead to bi-stability in target configurations 1 and 2. At each target configuration, with respect to θ_A, the first derivative of

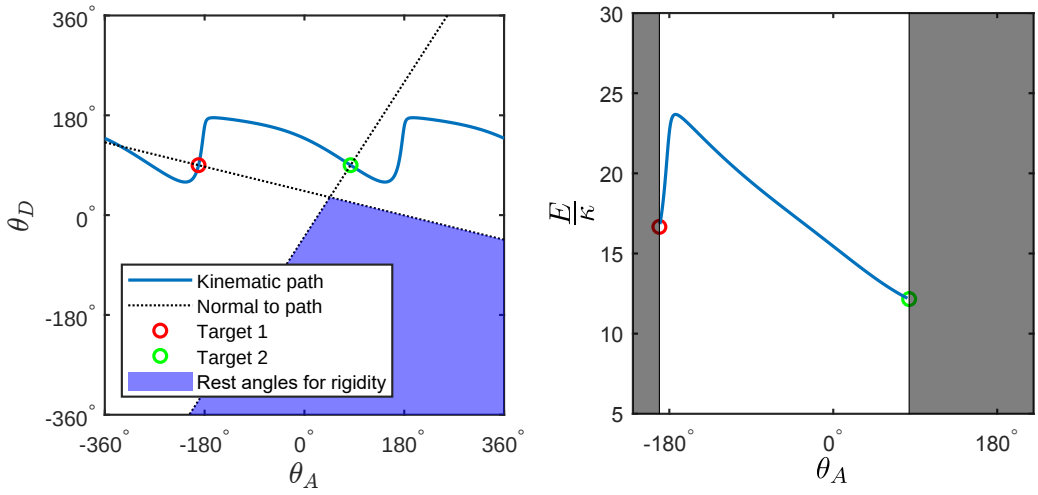

(a) (b)

Figure 2.3: Four bar linkage solution for rigidity at both target configurations. (a) Plot of the kinematic path and rest angles that lead to multi-configuration rigidity, in $\theta_A\theta_D$-space. (b) Energy profile along the kinematic path corresponding to $\theta_A^0 = 0$ and $\theta_D^0 = -180°$, which is a design in the blue region of (a). The dark shaded regions violate $\theta_D \geq 90°$.

the energy must be zero (equilibrium) and the second derivative must be positive (stability):

$$\frac{dE}{d\theta_A} = \kappa\left(\theta_A - \theta_A^0\right) + \kappa\left(\theta_D - \theta_D^0\right)\frac{d\theta_D}{d\theta_A} = 0 \tag{2.16}$$

$$\frac{d^2E}{d\theta_A^2} = \kappa\left(1 + \frac{d\theta_D}{d\theta_A}^2\right) + \kappa\left(\theta_D - \theta_D^0\right)\frac{d^2\theta_D}{d\theta_A^2} > 0. \tag{2.17}$$

Enforcing Eqs. (2.16) and (2.17) at both target configurations, there is a unique solution for the torsion spring rest angles of $\theta_A^0 = 45.9°$ and $\theta_D^0 = 32.2°$. Figure 2.4a shows the rest angle solution that leads to bi-stability. The energy along the kinematic path is shown in Figure 2.4b, where it is clear that both target configurations are smooth energy minima, in contrast to the boundary minima in the previous section.

By comparing the rigid and stable examples, two advantages of multi-configuration rigidity are observed. First, a large set of allowable rest angles leads to rigidity compared to a unique solution in the bi-stability case. This is because bi-stability requires an equation (Eq. (2.16)) and an inequality (Eq. (2.17)) to be satisfied at each target configuration. However, the rigidity conditions are less strict, only requiring a single inequality (Eq. (2.13)) to hold in each configuration. In practice, it is useful to have a set of allowable designs to give a margin for error when building

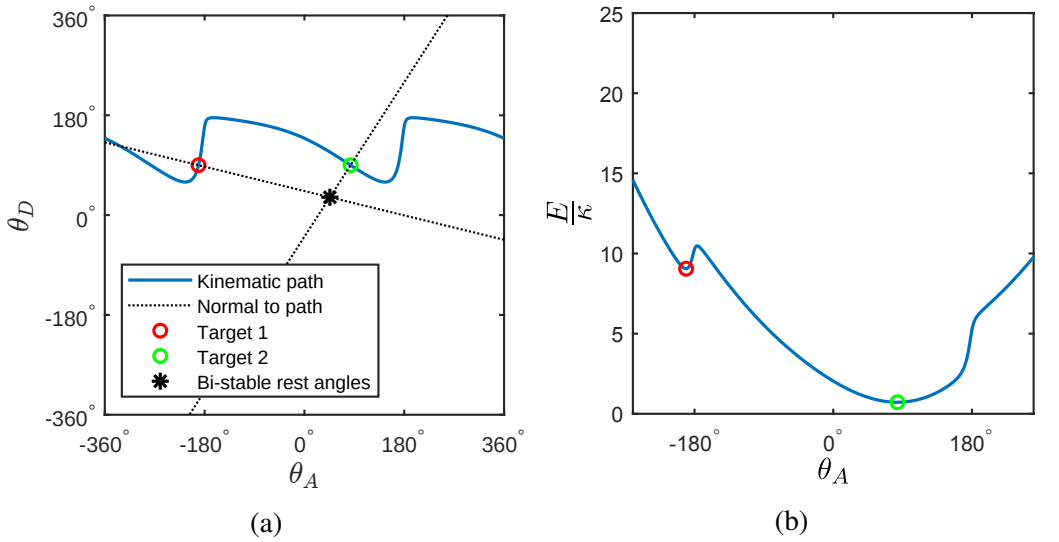

Figure 2.4: Four bar linkage solution for bi-stability. (a) Plot of the kinematic path and rest angles that lead to bi-stability, in $\theta_A\theta_D$-space. (b) Energy profile along the kinematic path for the bi-stable design $\theta_A^0 = 45.9°$ and $\theta_D^0 = 32.2°$.

physical structures, since precise values of stiffness and rest angles cannot be exactly achieved. The second advantage of multi-configuration rigidity is the ability to resist loads (below some critical value when contact is lost) without any displacement. Thus, there is an infinite initial stiffness with respect to perturbation forces, under the assumptions that the linkage consists of rigid bars and there is rigid contact with the unilateral constraint. In contrast, for multi-stability, the structure will deform elastically in response to any perturbation and the energy minima may have low stiffness.

2.4 A 24-DOF surface with two rigid configurations

To demonstrate multi-configuration rigidity in a complex structure, an example is presented of a 24-DOF kirigami pattern that can morph between a spherical configuration and a flat configuration. A set of angle stops are added throughout the structure to restrict the fold angles. Torsion springs are embedded along every fold of the structure, and the stiffness and rest angles of these springs are designed such that both the flat and spherical configurations satisfy the conditions for rigidity. The usefulness of multi-configuration rigidity for practical engineering applications is demonstrated by constructing a prototype of the morphing surface that is outfitted with antennas to create a functional morphing phased array antenna.

2.4.1 Geometry synthesis

Figure 2.5 shows the geometry of the morphing surface. The geometry consists of a set of square tiles, shown in green, that are connected by trapezoidal folds, shown in gray. The pattern can morph between flat and spherical surfaces, where the tiles lie on a sphere in the spherical configuration and are co-planar in the flat configuration. The pattern itself is non-developable, so it cannot be entirely flattened such that all faces (both green and gray) become co-planar.

Synthesis of this fold pattern follows a two-step process. First, the tiles are arranged on the surface of a sphere, shown in Figure 2.5a. The tile arrangement problem is formulated as a constrained optimization problem and is presented in detail in [30]. In this study, a sphere with a radius of 2.9 times the tile edge length is considered. The second step in the geometry synthesis process connects the adjacent tiles with valley folds, shown in gray in Figure 2.5b. The gray faces are added perpendicular to the tiles so all mountain folds are at 90° in the spherical configuration. Finally, upon closing the valley folds a flat configuration is achieved where the tiles come together to make a planar square grid, shown in Figure 2.5c.

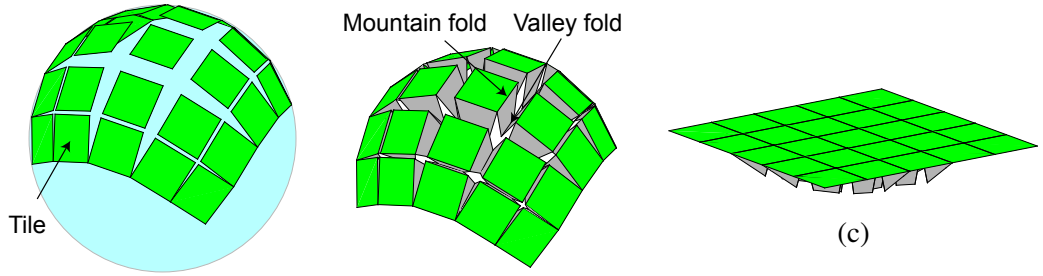

Figure 2.5: Geometry of the morphing surface kirigami pattern. (a) Arrangement of tiles on a sphere. (b) Valley folds are inserted perpendicular to the tiles to connect adjacent tiles, resulting in the spherical configuration. (c) Upon closing the valley folds, the flat configuration is achieved.

The fold angles are defined such that an angle is zero when the plates on either side of the fold are coplanar; at ±180°, there is contact. In the flat configuration, the mountain folds are at 90° and the valley folds are at 180°. In the spherical configuration, the mountain folds are at 90°, while the valley folds take on a range of angles between 150° and 160°.

2.4.2 Kinematics

The geometry of the structure is defined by vertex coordinates $\boldsymbol{x} \in \mathbb{R}^{3n}$ where n is the number of vertices in the pattern. Denote $\boldsymbol{\theta}_M \in \mathbb{R}^{n_M}$ and $\boldsymbol{\theta}_V \in \mathbb{R}^{n_V}$ as vectors containing the angles of the n_M mountain folds and n_V valley folds, respectively.

The kinematics of the structure can be captured by a pin-jointed bar model, which is outlined in Appendix A. In this kinematic model, a set of n_b bilateral constraints are used to capture the rigid-folding kinematics. The bilateral constraint gradients, or the compatibility matrix, is given by $\boldsymbol{C}^b \in \mathbb{R}^{n_b \times 3n}$. An admissible displacement from configuration $\boldsymbol{x}_t$, given by $\boldsymbol{d}_m = \boldsymbol{x} - \boldsymbol{x}_t \in \mathbb{R}^{3n}$, takes the form $\boldsymbol{d}_m = \boldsymbol{W}_m \boldsymbol{\alpha}$. The matrix $\boldsymbol{W}_m$ has dimension $3n \times m$, where the columns are basis vectors for the m-dimensional null space of $\boldsymbol{C}^b$. The vector $\boldsymbol{\alpha} \in \mathbb{R}^m$ contains amplitudes of the mechanisms. The number of mechanisms of this pattern (excluding rigid body motion), also known as the number of degrees of freedom, is $m = 24$.

In addition to the bilateral constraints, a set of unilateral constraints are embedded throughout the fold pattern in the form of restrictions on the fold angles, which are introduced to achieve multi-configuration rigidity. Observing that both the flat and spherical configurations have 90° mountain fold angles, we choose to restrict the mountain fold angles to be greater than 90°. The unilateral constraints take the form

$$90^\circ - \theta_{Mj}(\boldsymbol{x}) \leq 0, \quad j = 1, ..., n_M. \tag{2.18}$$

The gradients of the unilateral constraint functions are defined as $\boldsymbol{C}^u \in \mathbb{R}^{n_M \times 3n}$, where

$$\boldsymbol{C}^u = -\frac{\partial \boldsymbol{\theta}_M}{\partial \boldsymbol{x}}. \tag{2.19}$$

Full expressions for the gradients of hinge angles with respect to vertex coordinates can be found in Appendix A.

2.4.3 Equilibrium

Linear torsion springs are introduced on each fold of the structure, which will be designed to achieve rigidity in the spherical and flat configurations. To simplify the problem, it is assumed that all springs on the mountain folds are identical and all springs on the valley folds are identical. Hence, the springs moments take the form

$$m_i = \begin{cases} -\kappa_M(\theta_{Mi} - \theta^0_{Mi}) & i = 1, ..., n_M \\ -\kappa_V(\theta_{Vi} - \theta^0_{Vi}) & i = n_M + 1, ..., n_M + n_V, \end{cases} \tag{2.20}$$

where κ_M and θ_M^0 are the stiffness and rest angle of the mountain folds, and κ_V and θ_V^0 are the stiffness and rest angle of the valley folds. Since scaling of the stiffness does not affect the shape of the energy landscape, only three design variables must be considered: κ_V/κ_M, θ_M^0, and θ_V^0.

Now that a set of springs has been introduced, the equilibrium conditions can be derived using the principle of virtual work. Specifically, we derive equilibrium conditions in each target configuration by considering the virtual work through a first-order compatible displacement $\boldsymbol{d}_m = \boldsymbol{W}_m\boldsymbol{\alpha}$.

The work of the springs through the virtual displacement is $\boldsymbol{m}^T\boldsymbol{\delta\theta}$ where $\boldsymbol{\delta\theta}$ is a vector of corresponding angular displacements. To be compatible with $\boldsymbol{d}_m$, the angular displacements must satisfy $\boldsymbol{\delta\theta} = \boldsymbol{C}^s\boldsymbol{d}_m$. Here, the compatibility matrix of the springs is defined as $\boldsymbol{C}^s = \frac{\partial\boldsymbol{\theta}}{\partial\boldsymbol{x}}$, with dimension $(n_M + n_V) \times 3n$. The work associated with the unilateral constraints is $\boldsymbol{\mu}^T\boldsymbol{\delta\theta}_M$. The vector $\boldsymbol{\mu} \in \mathbb{R}^{n_M}$ contains generalized reaction forces in the unilateral constraints, which for angle constraints correspond to reaction moments and for rigid bar constraints correspond to bar forces. A compatible angular displacement of the mountain folds $\boldsymbol{\delta\theta}_M$ satisfies $\boldsymbol{\delta\theta}_M = \boldsymbol{C}^u\boldsymbol{W}_m\boldsymbol{\alpha}$. Equating the work of the springs and the unilateral constraints, we obtain

$$\boldsymbol{\mu}^T\boldsymbol{C}^u\boldsymbol{W}_m\boldsymbol{\alpha} = \boldsymbol{m}^T\boldsymbol{C}^s\boldsymbol{W}_m\boldsymbol{\alpha}. \tag{2.21}$$

This must hold generally for nonzero $\boldsymbol{\alpha}$. Thus, the conditions for equilibrium take the form

$$\boldsymbol{\mu}^T\boldsymbol{C}^u\boldsymbol{W}_m = \boldsymbol{m}^T\boldsymbol{C}^s\boldsymbol{W}_m \tag{2.22}$$

$$\mu_i \geq 0, \quad i = 1, \ldots, n_M \tag{2.23}$$

$$\mu_i(\theta_{Mi} - 90^\circ) = 0, \quad i = 1, \ldots, n_M. \tag{2.24}$$

Equation (2.22) represents a generalized force balance, while Eq. (2.23) requires the unilateral constraint reactions to be non-negative. Equation (2.24) is the complementary slackness condition, which states that a unilateral reaction can only be nonzero if there is contact with the constraint.

Given a set of spring parameters, which determine the spring moments $\boldsymbol{m}$, the constraint reaction forces can be computed. Equation (2.22) is a linear system with respect to $\boldsymbol{\mu}$, which can be written as

$$\boldsymbol{W}_m^T\boldsymbol{C}^{uT}\boldsymbol{\mu} = \boldsymbol{W}_m^T\boldsymbol{C}^{sT}\boldsymbol{m}. \tag{2.25}$$

Here, the matrix $\boldsymbol{W}_m^T \boldsymbol{C}^{uT}$ has dimension $m \times n_a$, where $m = 24$ mechanisms and $n_M = 80$ unilateral constraints, so the system is underdetermined and the reaction forces are not unique. However, if a solution exists where all components of $\boldsymbol{\mu}$ are positive, then the configuration is rigid. Rigorous formulation and proof of this rigidity condition is presented in Chapter 5.

2.4.4 Designing for multi-configuration rigidity

A design problem is posed to select spring parameters κ_V/κ_M, θ_M^0, and θ_V^0 such that both the flat and spherical configurations are both rigid. Rigidity occurs when positive unilateral reactions $\boldsymbol{\mu}$ satisfy equilibrium, since there are 80 unilateral constraints (stops on the 80 mountain folds), which are enough to block motion along the 24 mechanisms. The design space is limited to only three variables, allowing for a direct search of the design space to evaluate which designs lead to rigidity.

A search was performed in the region $-360^\circ \leq \theta_M^0 \leq 360^\circ$, $-360^\circ \leq \theta_V^0 \leq 360^\circ$, $0.1 \leq \kappa_V/\kappa_M \leq 10$. At any given point in this region, the solution to Eq. (2.25) can be evaluated in both configurations to check for positive unilateral reactions. By evaluating many designs, the design space can be partitioned into regions where the rigidity condition is satisfied for each configuration.

Figure 2.6 shows the regions of the design space where rigidity is achieved in the spherical and flat configurations. The axes of these plots correspond to the rest angles of the mountain and valley folds. In the black regions, equilibrium is violated for all values of the valley to mountain stiffness ratio, κ_V/κ_M. In the white regions, the rigidity conditions are satisfied for some or all values of κ_V/κ_M.

The design chosen for building the prototype in the next section has $\theta_V^0 = 180^\circ$ and $\theta_M^0 = 0^\circ$, and corresponds to the red dot in Figure 2.6. For these rest angles, as long as $\kappa_V/\kappa_M < 1.33$, the structure satisfies the rigidity conditions in both the spherical and flat configurations. These rest angles are desirable since they not only satisfy the rigidity conditions, but they are straightforward to fabricate.

2.4.5 Prototype

A prototype of the 24-DOF kirigami surface was constructed to demonstrate multi-configuration rigidity in a physical structure. Following the spring design analysis, both the flat and spherical configurations are rigid if $\theta_V^0 = 180^\circ$, $\theta_M^0 = 0$, $\kappa_V/\kappa_M < 1.33$, and stops restrict all mountain folds to $\boldsymbol{\theta}_M \geq 90^\circ$.

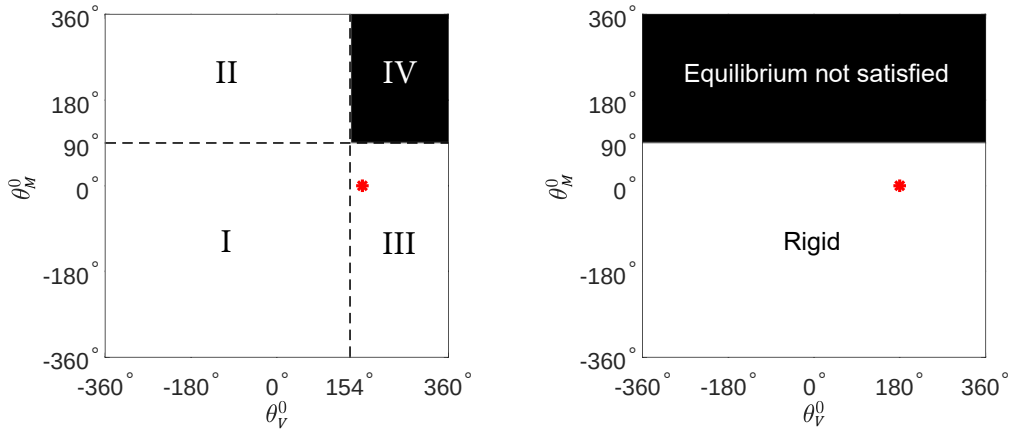

Figure 2.6: Design space of the 24-DOF morphing surface. (a) Spherical configuration. Region I satisfies rigidity for any stiffness ratio, while region IV violates equilibrium for all stiffness ratios. In region II, rigidity is maintained above some value of κ_V/κ_M and in region III, rigidity is maintained below some value of κ_V/κ_M. (b) Flat configuration. The partition holds for all κ_V/κ_M. The red dot marks the design used for the prototype, $(\theta_V^0, \theta_M^0) = (180°, 0°)$.

To fabricate compliant folds with these properties, lamina emergent torsion (LET) joints [57] were used. LET joints connect two plates with a series of slender cutout beams. The beams twist as the plates rotate with respect to each other, which imparts stiffness to the fold. Specific stiffness values can be obtained by tailoring the dimensions of the beams and several values of the rest angles can be achieved by cutting the plates as separate components and attaching them at an angle.

To achieve a compliant valley fold with a rest angle of 180°, a LET joint was created using two separate plates, as shown in Figure 2.7a. The plates were connected with screws to form a compliant fold with a fully closed rest angle, as shown in Figure 2.7b. To achieve a compliant mountain fold with a rest angle of 0°, the LET joint was cut from a single flat sheet. Figure 2.8a shows a component consisting of a square tile attached to four plates with a zero rest angle LET joint. A clip was added to the mountain folds to restrict the angle to greater than 90°. The clip was cut from a 0.51 mm thick stainless steel sheet and bent to an angle that, when attached to the mountain fold, restricted its angle to greater than 90°. A photo of one mountain fold with the clip applied is shown in Figure 2.8b. Both the mountain and valley folds were cut from 0.635 mm thick spring steel by waterjet.

There is no specifically required valley-to-mountain fold stiffness ratio. For any value less than 1.33, both configurations satisfy the rigidity conditions. An approximation

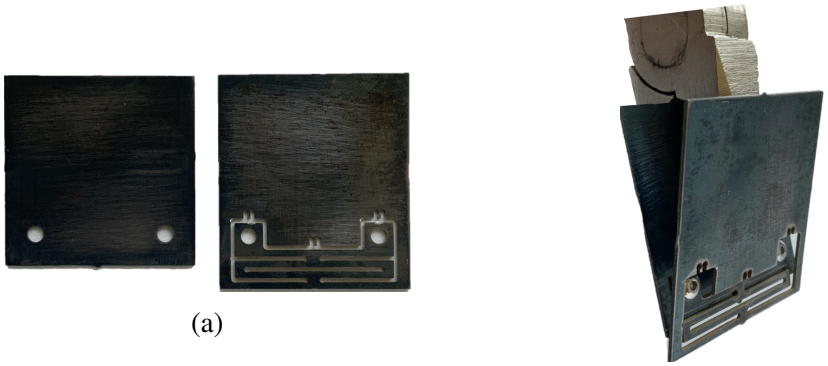

(a) (b)

Figure 2.7: Photos of the compliant valley fold design. (a) Initially cut as two separate plates. (b) The plates were attached with screws and held partially open. This creates a compliant fold with rest angle 180°.

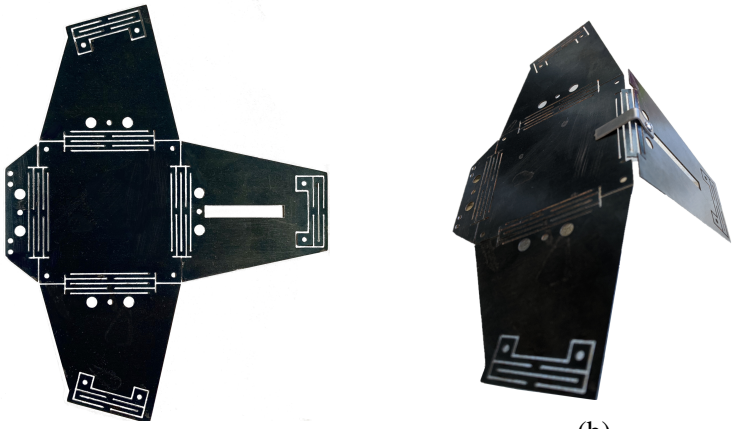

(a) (b)

Figure 2.8: Photos of compliant mountain fold design. (a) Initially cut from a flat sheet. (b) Partially assembled with 90° clip attached to one mountain fold. The mountain fold has rest angle 0 and is restricted to greater than 90° by the clip.

of the torsional stiffness of a LET joint can be made using a simple beam torsion model [57]. Using this approximation, the stiffness of the valley and mountain folds are estimated to be 59.9 and 72.9 N mm/rad, respectively. The corresponding stiffness ratio of 0.82 falls within the required range for rigidity in both configurations with margin for error.

Using the LET mountain and valley folds as the primary building blocks, a full prototype of the surface was assembled. The scale of the structure was set by the tile side length of 6.75 cm. The radius of the corresponding target spherical surface is 19.6 cm. Since the pattern is non-developable, it must be fabricated as an assembly

of separate components. Fabrication and assembly of the prototype was a two-step process. The inner 3-by-3 grid of tiles and the outer tiles were assembled separately, then joined to complete the structure. Cut patterns for the inner and outer tiles are shown in Figure 2.9.

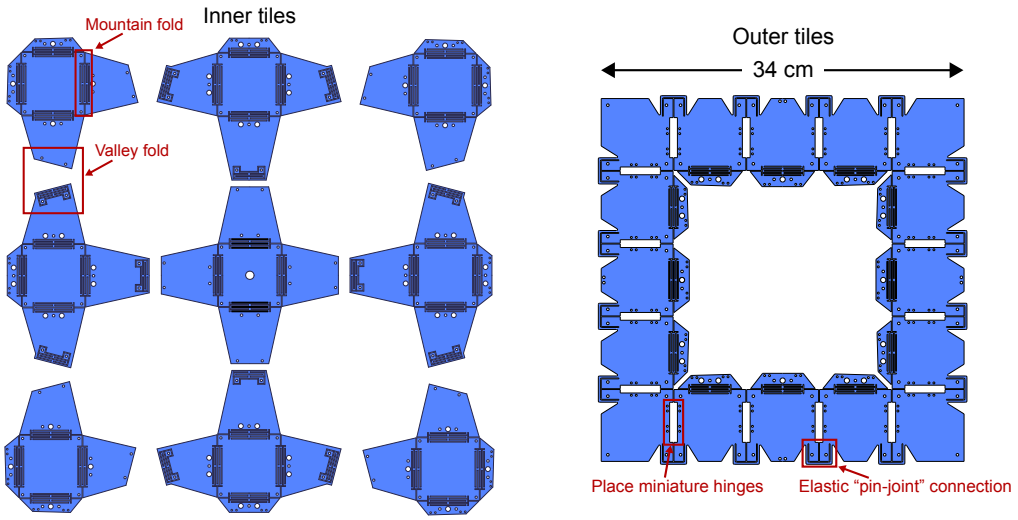

(a) (b)

Figure 2.9: Prototype cut pattern, consisting of (a) inner tiles and (b) outer tiles. To assemble, 90° clips were attached to each mountain fold. Then, valley folds of the inner tiles were attached with screws. The inner tiles were placed inside the outer tiles and the connecting valley folds were fastened.

The inner 3-by-3 grid of tiles was cut as 9 individual components. Each component consists of a square tile and the surrounding four facets. The edges of the square tile are compliant mountain folds. The first step in the assembly process was to attach the clip to each mountain fold, as shown in Figure 2.8b where the clip has been attached to one mountain fold. Once the mountain folds were held to 90° by the clips, adjacent tiles were connected. Connections between adjacent tiles are compliant valley folds following the design of Figure 2.7.

The outer loop of 16 tiles was cut from a single sheet. In the fold pattern, the corners of adjacent squares lying on the outer perimeter are joined. To emulate the kinematics of a pin-joint connection, a beam attaches the corners of the outer squares as shown in Figure 2.10.

The folds connecting the outer tiles are too small to use LET joints. Thickness of the plate and kerf of the waterjet are limiting factors on the minimum size of the LET joints. Instead, miniature hinges (8 by 10 mm when flat) were used for the

outer folds, as shown in Figure 2.10. While these are not compliant hinges, the compliance of the folds on the inner tiles is sufficient to achieve rigidity.

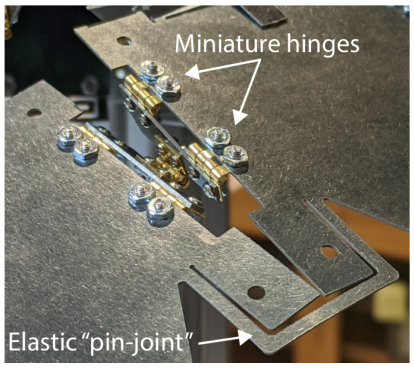

Figure 2.10: Design of the folds connecting the outer tiles. Miniature hinges were used instead of LET hinges due to the small geometric features. An elastic beam connects the outer corners of adjacent squares to imitate pin-joint kinematics.

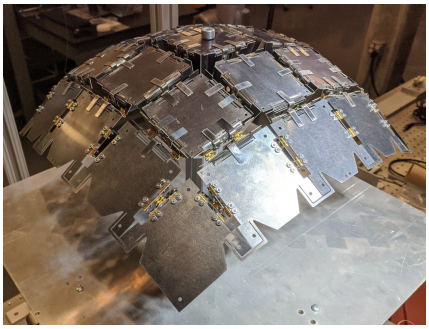

(a)

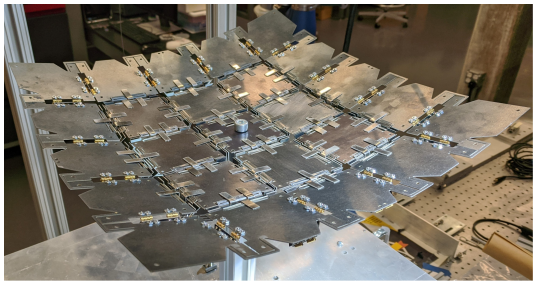

(b)

Figure 2.11: Prototype of the 24-DOF morphing surface. (a) Spherical configuration. (b) Flat configuration.

Finally, the assembled inner tiles were attached to the outer tiles. Miniature hinges were also used for the valley folds connecting the inner tiles to the outer tiles due to the small size of the fold. A photo of the complete prototype is shown in Figure 2.11. The structure was mounted by clamping the center tile to a vertical post underneath the structure.

As expected, the structure is rigid in the spherical and flat configurations. No intermediate stable configurations were observed. Actuation between the two configurations is straightforward and does not require 24 actuators, despite the 24-DOF kinematics. For example, upward forces on the four corners transform the structure from the spherical to the flat configuration while downward forces on the corners

transform the structure from the flat to the spherical configuration. Simple mechanical actuation schemes, such a linear actuator or an actuation cable, would be suitable for automated reconfiguration between the two configurations.

While the prototype exhibits two rigid target configurations, these configurations deviate from the ideal flat and spherical shapes. In particular, the flat configuration is not perfectly planar. There are two primary factors contributing to the prototype deviating from the ideal shapes. First, the parameters of the physical prototype slightly deviate from the ideal values of the design. Particularly, the angle stops on the mountain folds do not perfectly hold the folds at 90°. The second factor is elastic compliance of the physical components, which were modeled by perfect plate-hinge kinematics. LET joints are known to have unwanted kinematics beyond those of a perfect rotational hinge, such as relative torsion and tension between the plates connected by the joint [58]. Despite these undesired sources of compliance, the prototype qualitatively produced the desired behavior.

To demonstrate a practical application of this work, the prototype was outfitted with antenna elements above each tile to create a phased array antenna. The prototype with antennas mounted is shown in Figure 2.12. Details regarding the architecture and performance of the antenna from the electrical engineering perspective are presented in [19].

Finally, the ability to support antenna tiles demonstrates the load-bearing capability of the rigid configurations. The self-weight of the prototype structure is 1.05 kg while the antenna payloads have a net weight of 0.85 kg. Thus, 1.9 kg is supported in each configuration. While this causes some visible deformation due to the elasticity of the plates and angle stops, both the spherical and flat configurations can support this loading.

2.5 Conclusion

This chapter presented an introduction to the concept of multi-configuration rigidity through examples. Two structures were studied: a single-DOF four bar linkage and a 24-DOF kirigami surface. The advantages of multi-configuration rigidity, when compared to multi-stability, are evident in the single-DOF linkage example. First, multi-configuration rigidity is advantageous because each configuration can rigidly resist perturbation forces up to a finite magnitude. Second, the design space of spring parameters leading to rigidity is larger, which is especially useful for physical implementation. For the 24-DOF example, a prototype was built with flat and

(a) (b)

Figure 2.12: Prototype structure with phased array antenna tiles. (a) Spherical configuration. (b) Flat configuration.

spherical configurations designed to be rigid using torsion springs and angle stops. The prototype was outfitted with antenna tiles to create a functional phased array antenna.

Chapter 3

SYNTHESIS OF KIRIGAMI TILED SURFACES

Research presented in this chapter has been adapted from the following publication:

C. Dorn, R. Lang, S. Pellegrino, "Kirigami tiled surfaces with multiple configurations," *In preparation*.

3.1 Introduction

Origami offers a platform for transforming a flat sheet into three-dimensional surfaces by folding. Although rigid folding cannot change the intrinsic Gaussian curvature of a sheet, surfaces approximated by tiles connected by "hidden" connections can vary their apparent Gaussian curvature [32]. The inverse problem of synthesizing fold patterns capable of transforming a flat sheet into a surface with specified apparent curvature has attracted significant interest in recent years. An extension of the inverse problem is to create fold patterns capable of achieving surfaces with different apparent curvatures, which has received little attention despite its broad potential for application. This chapter presents the synthesis of kirigami fold patterns capable of approximating several specified target surfaces with differing Gaussian curvature.

A significant body of work has focused on synthesizing fold patterns capable of realizing curved surfaces from a flat sheet. The early work of Resch [39, 40] proposed several origami patterns that can achieve curved surfaces. Subsequently, various computational methods have been developed for fold pattern synthesis. One means of achieving surfaces with specified curvature is by generalizing patterns such as the Miura-ori [37, 59] and Resch's patterns [31]. General algorithms such as TreeMaker [60] and Tachi's Origamizer [41] can create fold patterns to achieve an arbitrary 3D shape. Alternatively, kirigami patterns, which allow cuts to be made in the sheet, can be designed to realize arbitrary 3D surfaces [16, 61].

Less work, however, has focused on creating fold patterns capable of achieving multiple configurations, sometimes referred to as *pluripotent* patterns. One approach is to superimpose multiple fold patterns on the same sheet, activating one set of folds at a time [62]. Others rely on switching the mountain-valley fold assignments to achieve multiple target shapes. Universal origami [63, 64] and kirigami [65]

patterns exist that can approximate any arbitrary shape, but they are limited to step-approximations of the shapes. Smoother approximations of multiple target surfaces are achieved by [34], where quadrilateral crease patterns are systematically designed to realize multiple target shapes. While a generic quadrilateral mesh is rigid, a generic triangular lattice is not only flexible with many degrees of freedom, but the number of distinct branches of motion increases exponentially with the number of vertices in the pattern [66].

In this chapter, a family of kirigami patterns is introduced that can achieve multiple specified target surfaces with different Gaussian curvature. The patterns consist of an arrangement of tiles connected by sub-folds and, although the patterns cannot vary their intrinsic curvature, the apparent surfaces approximated by the tiles can achieve a wide range of Gaussian curvatures. Unlike existing pluripotent patterns that rely on switching the mountain-valley assignment to achieve multiple target configurations, the physical mechanism for the transformation used in this research is changing the angles of the sub-folds.

The geometric synthesis of these patterns is framed as a tile arrangement problem, involving identical tiles that are required to approximate to all target surfaces. A set of geometric constraints is formulated to ensure compatibility between the arrangements corresponding to the target surfaces. Once the tile arrangements have been computed, the fold pattern synthesis is completed by adding sub-folds between adjacent tiles in any one of the arrangements. Since the tile arrangements corresponding to each target surface are already compatible, the pattern can be reconfigured into all of the target arrangements. The resulting patterns are rigidly foldable with many kinematic degrees of freedom, allowing rigid folding paths between the target surface configurations. Kinematic simulations are presented to demonstrate the reconfiguration between the target surfaces. The fold patterns have a relatively simple geometry, which is desirable from a manufacturing standpoint. A demonstration prototype is constructed that can achieve six target shapes. The prototype is built from 3D printed plates connected by steel pin hinges.

3.2 Preliminaries

Given a set of target surfaces, Fig. 3.1(a), consider a pattern in a planar configuration consisting of a set of *tiles* connected by *sub-folds*, Fig. 3.1(b). The tiles are highlighted in green and the sub-folds in gray and the pattern consists of loops of tiles connected by sub-folds. The *apparent surface* is defined as the surface tangent

to the tiles; the sub-folds are disregarded. The pattern is designed such that varying the sub-fold angles allows the apparent surface to approximate each target surface, Fig. 3.1(c).1-3. By closing the sub-folds, a flat apparent surface is achieved where the edges of adjacent tiles are coincident, Fig. 3.1c.4.

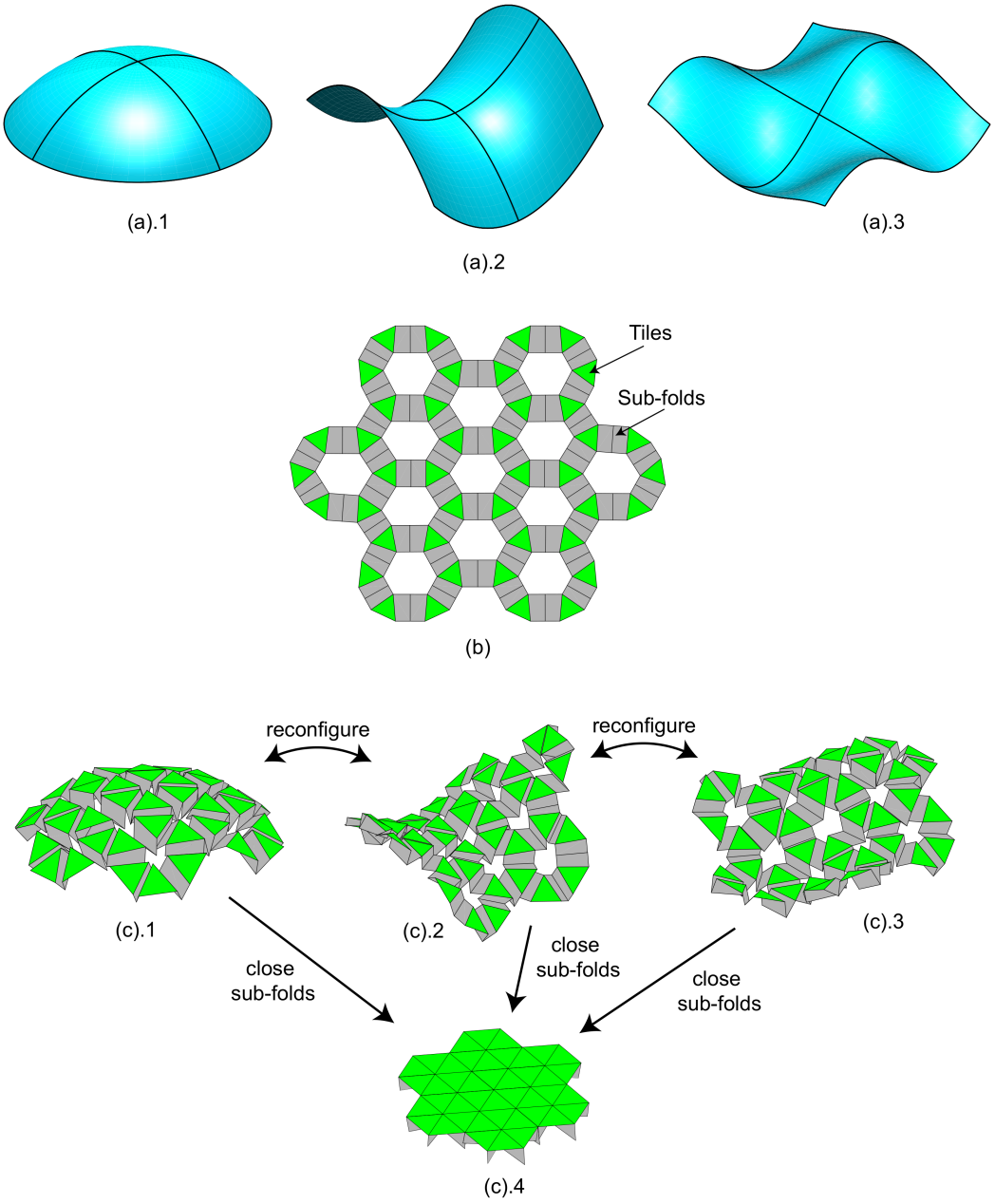

Figure 3.1: Overview of the proposed kirigami patterns. (a) Target surfaces with different Gaussian curvature. (b) A kirigami pattern that can approximate these surfaces. (c) Reconfigurations of the kirigami pattern into target surfaces and a flat configuration.

The chosen architecture of loops of tiles connected by sub-folds allows the pattern to approximate a wide range of apparent surfaces. The presence of holes plays an important role by introducing many kinematic degrees of freedom, allowing a rich configuration space accessible by rigid folding. Kinematic freedom inherently comes from the boundary of the pattern. Including holes in a pattern increases the number of boundary edges in the pattern, leading to more degrees of freedom. The equation for the number of kinematic degrees of freedom of a general fold pattern was derived by Tachi [15]:

$$\text{DOF} = B - 3H + S - 3 - \sum_{k \geq 4} (k-3) P_k, \tag{3.1}$$

where B is the number of edges on the boundary, H is the number of holes, S is the number of redundant constraints (states of self stress), and P_k is the number of faces in the pattern with k sides. This determines the number of internal mechanisms of the fold pattern and does not include rigid body motion.

In this chapter, we consider patterns with triangular or square tiles that are connected by trapezoidal sub-folds. For these patterns, only $k = 4$ appears in the summation in Eq. (3.1). The number of quadrilateral faces in the pattern is $P_4 = 2N_g + N_{t,sq}$, where N_g is the number of sub-folds and $N_{t,sq}$ is the number of square tiles in the pattern. For patterns with triangular tiles, $N_{t,sq} = 0$. The number of degrees of freedom of these patterns can be expressed as

$$\text{DOF} = B - 3H + S - 3 - 2N_g - N_{t,sq}. \tag{3.2}$$

It is evident from Eq. (3.2) that the presence of holes increases the number of degrees of freedom since each hole introduces boundary edges. For each hole, there are at least three boundary edges that define the hole. Thus, the $B - 3H$ terms in Eq. (3.2) increases as the number of holes increases, as long as the holes have more than 3 sides.

Consider, for example, a loop of four square tiles connected by sub-folds, as shown in Fig. 3.2. There are $B = 24$ boundary edges, $H = 1$ hole, $N_g = 4$ sub-folds, and $N_{t,sq} = 4$ square tiles. Generically, there are no states of self stress ($S = 0$) in the loop, which can be verified using the kinematic model in Appendix A. From Eq. (3.2), the loop has 6 degrees of freedom. The presence of the hole contributes to the number of degrees of freedom since there are 8 boundary edges associated with the hole, which is larger than the $-3H$ term associated with the hole.

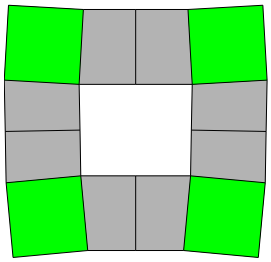

Figure 3.2: A loop of square tiles connected by sub-folds with 6 kinematic degrees of freedom.

3.3 Intrinsic vs. apparent curvature

Gauss's Theorema Egregium states that the Gaussian curvature of a surface is invariant under isometric transformations [67], which applies generally to both smooth and discrete surfaces. In the context of discrete surfaces, rigid folding is an isometric transformation and hence the discrete Gaussian curvature of a fold pattern is an intrinsic property, which cannot be changed through folding. However, the patterns presented in this work are capable of approximating multiple surfaces with different Gaussian curvature, motivating the distinction between the *intrinsic* and the *apparent* discrete Gaussian curvature of the pattern.

Before defining discrete curvature, the Gaussian curvature of a smooth surface can be defined in the context of the Gauss map of a contour on the surface. Consider a closed loop C on a smooth surface, as shown in Fig. 3.3a. The Gauss map of C is constructed by mapping the surface normal vector along C to the unit sphere, shown in Fig. 3.3b. The Gaussian curvature at a point P on the surface can be defined through the ratio of the spherical area $A(C')$ enclosed by C' on the Gauss map of the area $A(C)$ enclosed by C on the surface as C approaches P [67]:

$$K_P = \lim_{C \to P} \frac{A(C')}{A(C)}. \tag{3.3}$$

Note that $A(C')$ is the signed area and the direction of transversal matters.

The definition of Gaussian curvature in (3.3) does not directly apply to discrete surfaces; since curvature of a discrete surface is concentrated at points, the ratio of $A(C')$ to $A(C)$ is singular in the limit of a shrinking contour. This motivates the definition of the *discrete Gaussian curvature* K as the area on the Gauss map of the trace of a closed loop on the surface:

$$K = A(C'). \tag{3.4}$$

(a) (b)

Figure 3.3: Definition of the Gauss map. (a) Contour C on a smooth surface, with the normal vector shown at one point. (b) Gauss map C' of the contour with the corresponding normal vector at one point shown.

A discussion of the discrete Gaussian curvature can be found in [68] and Gauss maps are discussed in [69] in the context of origami. This definition of discrete Gaussian curvature is meaningful even for discrete surfaces with holes, which is relevant to the patterns presented in this chapter. An example of the Gauss map of a discrete loop is shown in Fig. 3.4. Note that this definition of discrete Gaussian curvature is an integrated quantity, not a point-wise measure of curvature. See [68] for a discussion of estimating point-wise curvature from discrete curvature.

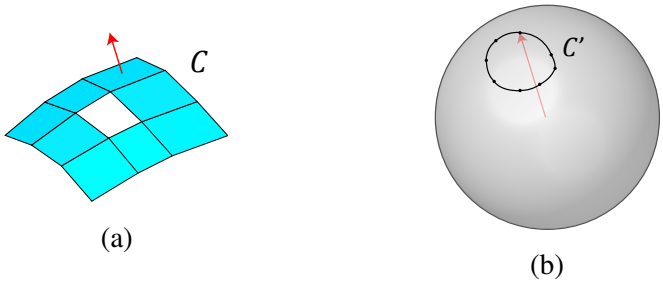

(a) (b)

Figure 3.4: Gauss map of a loop on a discrete surface. (a) Discrete loop C, with the normal vector of one face shown. (b) Gauss map C' of the loop, with the corresponding normal vector of one face shown.

The discrete Gaussian curvature of Eq. (3.4) allows us to define the intrinsic curvature of the presented kirigami patterns by examining loops in the pattern. The area enclosed on the Gauss map of a discrete loop is equal to the angular defect Δ of the loop [70], which is obtained by cutting and flattening the loop. Figure 3.5 shows loops of tiles connected by sub-folds with positive, zero, and negative intrinsic curvature. The case with zero intrinsic curvature, shown in Figure 3.5b, is *developable* since it can be flattened without cutting. Developability is often desirable from the manufacturing standpoint, since many fabrication techniques involve cutting an initially flat sheet.

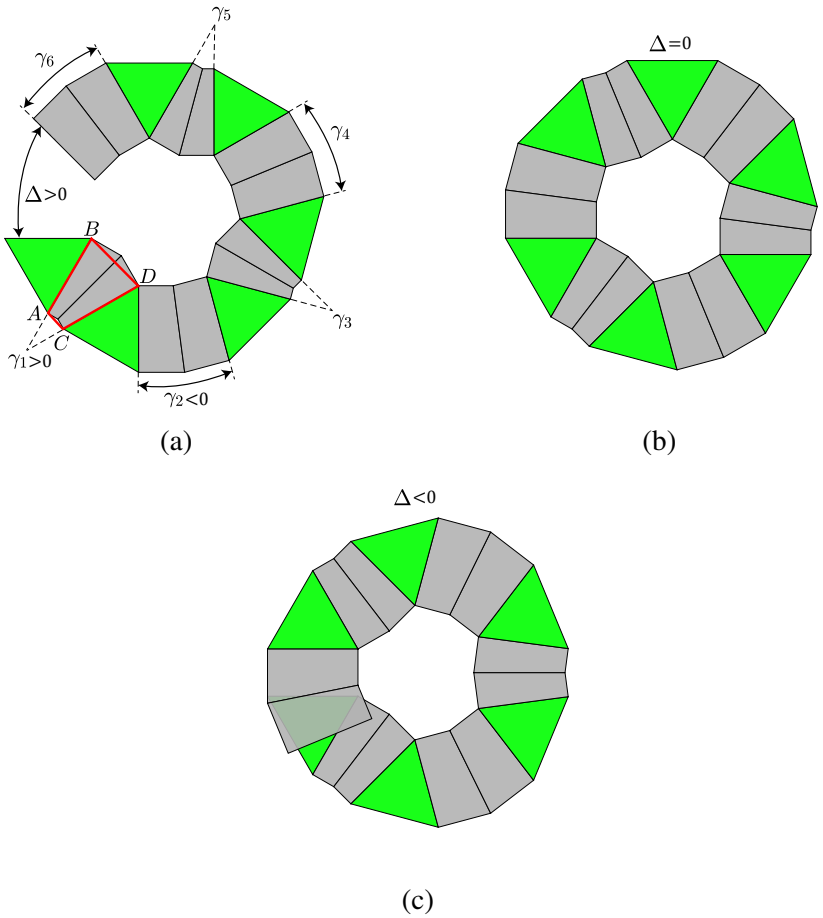

Figure 3.5: Loops of tiles with different intrinsic curvature. (a) Cut and flattened loop with positive intrinsic curvature. The isosceles trapezoid formed by gap 1 is highlighted in red. (b) Flattened loop with zero intrinsic curvature (developable). (c) Cut and flattened loop with negative intrinsic curvature.

The angular defect of the loops shown in Figure 3.5 depends on the geometry of the gaps between the tiles. It will be shown in Section 3.4 that for the kirigami patterns developed in this study, the polygon connecting the edges of two adjacent tiles is always planar and forms an isosceles trapezoid.

In Figure 3.5a, the trapezoid for gap 1 is defined by the tile vertices A, B, C, and D, as highlighted in red. The orientation of the trapezoidal gap determines how the gap contributes to the angular defect Δ of the loop. If the short side of the trapezoid lies on the outside of the loop, the gap contributes positively to the angular defect, which is the case for the highlighted trapezoid. If the gap is a rectangle, the contribution to Δ is zero. Finally, if the short side of the trapezoid lies on the inside of the loop, it makes a negative contribution to Δ.

In the case of equilateral triangular tiles, the intrinsic discrete Gaussian curvature of the loop, K, can be obtained from:

$$K = \Delta = \sum_{k=1}^{6} \gamma_k \tag{3.5}$$

where γ_k is the angle of the isosceles trapezoid corresponding to gap k, as defined in Fig. 3.5a. Note that the sign of γ depends on the orientation of the trapezoid: $\gamma_k > 0$ if $||\boldsymbol{BD}|| > ||\boldsymbol{AC}||$ and $\gamma_k < 0$ if $||\boldsymbol{BD}|| < ||\boldsymbol{AC}||$. To achieve a developable loop, either all of the gaps must be rectangles or there must be gaps of both orientations present whose angles γ_k sum to zero. The case where both orientations of gaps are present is of greatest interest, because it allows a range of apparent curvatures to be achieved.

While the intrinsic discrete Gaussian curvature is invariant, we define the *apparent* discrete Gaussian curvature as the discrete curvature of the surface formed by the tiles joined by trapezoids and disregarding the sub-folds. Figure 3.6a shows a loop of tiles connected by sub-folds. In Fig. 3.6b, the sub-folds have been removed and the resulting gaps have been filled with isosceles trapezoids. These added faces are highlighted in blue and the points A, B, C, D that correspond to the tile edges for one gap are labeled.

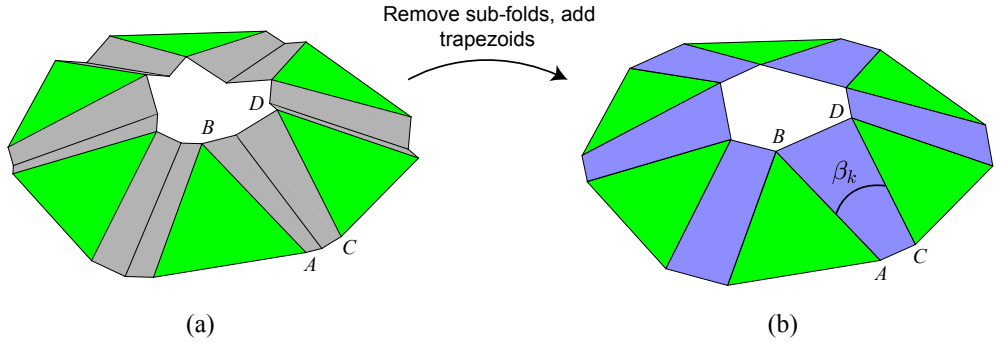

Figure 3.6: The apparent surface is defined by only considering the positions of the tiles. For the sake of defining apparent curvature, the gaps between tiles are filled with faces, which are highlighted in blue.

By considering the loop of tiles connected by the blue trapezoids, the apparent angular defect Δ_a of a loop of tiles can be defined, which corresponds to the apparent discrete Gaussian curvature K_a of the loop. Similarly to the intrinsic curvature, the angular defect of the loop depends on the orientation of the trapezoidal gaps between tiles. Trapezoids with the short side outside contribute positively to the

angular defect while trapezoids with the short side inside contribute negatively. In analogy to Eq. (3.5), the apparent curvature of a loop can be obtained from:

$$K_a = \Delta_a = \sum_{k=1}^{6} \beta_k \tag{3.6}$$

where β_k is the angle of the trapezoid corresponding to gap k, which is defined in Figure 3.6. The sign of β_k is positive for trapezoids with the short side out and negative for the opposite orientation.

Note that the sign of β_k matches the sign of γ_k for each gap. Therefore, each gap contributes either positively or negatively to both the intrinsic and apparent curvature. However, the magnitude of β_k varies as the sub-fold changes angle. Therefore, simply changing the sub-fold angles provides a mechanism for varying the apparent curvature. Furthermore, if a loop contains gaps of both orientations, the apparent curvature can assume both positive and negative values. Figure 3.7 shows the same loop with positive, zero, and negative apparent curvatures, illustrating the mechanism of apparent curvature change. The loop contains three gaps of each orientation. In Fig. 3.7a, the gaps with $\beta_k < 0$ are nearly closed ($\beta_k \approx 0$) while the gaps with $\beta_k > 0$ are kept open, so the sum of gap angles, which is the apparent curvature, is positive. If all sub-folds are closed, then $\beta_k = 0$ for all gaps and a zero apparent curvature is obtained, as in Fig. 3.7b. Finally, Fig. 3.7c shows a configuration where the gaps with $\beta_k < 0$ are open, leading to a negative apparent curvature.

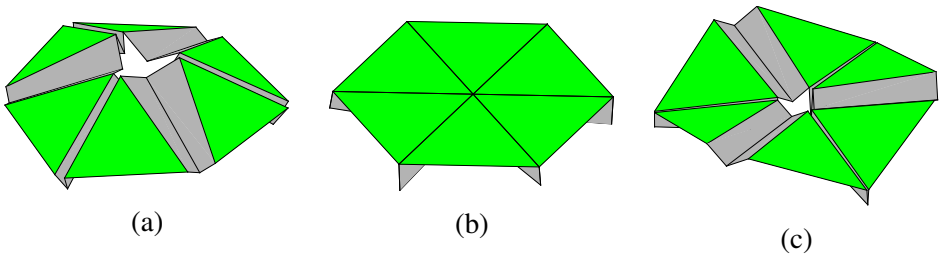

(a) (b) (c)

Figure 3.7: Three configurations of the same loop of tiles, which can achieve apparent curvature change by varying the sub-fold angles. (a) Positive apparent curvature; (b) zero apparent curvature; (c) negative apparent curvature.

This mechanism for curvature change can be replicated for larger patterns consisting of many loops, which can realize multiple surfaces with different curvatures. Each individual loop in the pattern can vary its apparent curvature, allowing a wide range of apparent surfaces with different curvatures to be created.

3.4 Gap conditions

The geometry of the gaps between the tiles has to satisfy conditions of two types. The first condition ensures that a sub-fold can be inserted between adjacent tiles, such that the edges of the tiles become coincident when the sub-fold is closed. The second condition ensures the compatibility of two gaps, meaning that the same sub-fold can span both gaps by varying only the fold angle. These conditions on the gaps between two tiles are used later, in Section 3.5, as constraints in the tile arrangement problem used to synthesize fold patterns.

3.4.1 Single sub-fold conditions

Consider two flat rigid tiles in three-dimensional space. We aim to derive conditions on the relative positions of the tiles to ensure that a single sub-fold can be inserted between the tiles such that upon closing the sub-fold, the tile edges become coincident. Figure 3.8 shows an example of tiles that satisfy these conditions, where edge AB and CD are brought together when the sub-fold is closed.

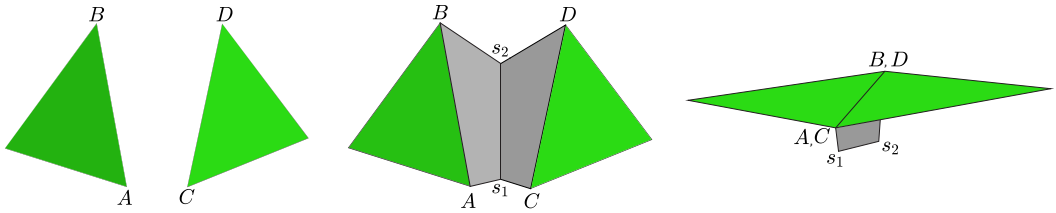

(a) (b) (c)

Figure 3.8: Two tiles with a gap that satisfies the single sub-fold conditions. (a) Definition of edges AB and CD (top view). (b) A single sub-fold, shown in gray, connecting edges AB and CD (top view). (c) When the sub-fold is closed, edges AB and CD become coincident (perspective view).

To develop general constraints on the relative positions of the tiles, we seek conditions for when points C and D can be brought to points A and B by rotating about some axis s through an angle φ, which is equivalent to closing a sub-fold. For an arbitrary point s_1 on the axis of rotation s, the length of vector $\boldsymbol{A}\mathbf{s}_1$ from A to s_1 and the length of vector $\boldsymbol{C}\mathbf{s}_1$ must be equal since these segments coincide when the sub-fold is closed. The same argument can be made for a point s_2, leading to the conditions

$$\begin{aligned} ||\boldsymbol{A}\mathbf{s}_1|| &= ||\boldsymbol{C}\mathbf{s}_1|| \\ ||\boldsymbol{B}\mathbf{s}_2|| &= ||\boldsymbol{D}\mathbf{s}_2||. \end{aligned} \tag{3.7}$$

Therefore, s must lie in planes P_1 and P_2, which perpendicularly bisect line segments AC and BD, respectively.

There are three possible cases concerning planes P_1 and P_2, which are illustrated in Fig. 3.9. In case 1, P_1 and P_2 intersect in a line. In this case, the only candidate axis of rotation s is the intersection line of the two planes. However, different rotation angles φ are generally required to bring C to A and D to B. In case 2, planes P_1 and P_2 are parallel, leaving no possible rotation axes. Finally, in case 3, planes P_1 and P_2 are coincident, leaving infinite candidate rotation axes from which s can be selected, which is the case of interest.

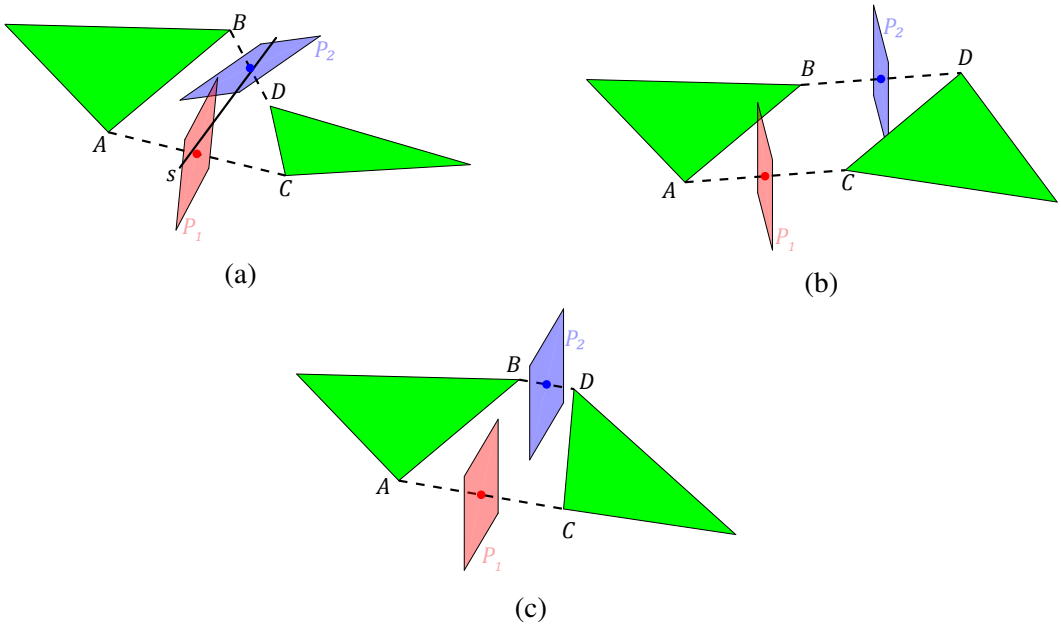

Figure 3.9: Three cases of a pair of tiles arranged in 3D space. (a) Case 1: planes P_1 and P_2 intersect in a unique line s. (b) Case 2: planes P_1 and P_2 do not intersect. (c) Case 3: planes P_1 and P_2 coincide.

Two conditions are needed to ensure that P_1 and P_2 coincide. First, points A, B, C, and D must be coplanar. This can be enforced by requiring that the triple product of vectors meeting at vertex A is zero:

$$\boldsymbol{BA} \times \boldsymbol{CA} \cdot \boldsymbol{DA} = 0. \tag{3.8}$$

This condition requires the volume of the parallelepiped generated by $\boldsymbol{BA}$, $\boldsymbol{CA}$, and $\boldsymbol{DA}$ is zero, enforcing coplanarity of A, B, C, and D. Equation (3.8) could be equivalently expressed in terms of vectors meeting at points B, C, or D.

The second condition arises from symmetry. Within the plane of points A, B, C, and D, edges AB and CD must be mirror symmetric with respect to the bisecting plane. Therefore A, B, C, and D form an isosceles trapezoid, which is equivalent to stating:

$$||\boldsymbol{AD}|| = ||\boldsymbol{BC}||. \tag{3.9}$$

The conditions in Eqs. (3.8) and (3.9) ensure that edges AB and CD can be brought together through the rotation of a sub-fold.

3.4.2 Gap compatibility

Two gaps are defined as compatible if they can be obtained by rotation of the same sub-fold. In the pattern synthesis process, this will be the key condition that allows multiple configurations to be achieved by the same fold pattern.

Consider a pair of tiles connected by a sub-fold. Figure 3.10a shows a top view of the pair of tiles for two different sub-fold angles. We aim to establish a condition on A, B, C, D, C' and D' that ensures the compatibility of Gap 1 and Gap 2.

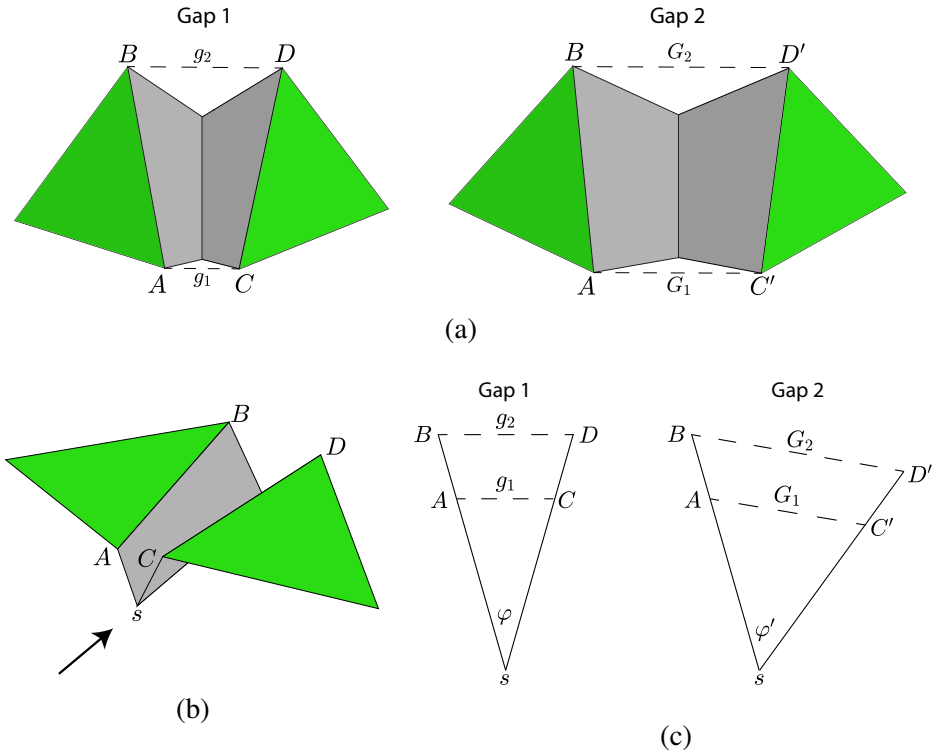

Figure 3.10: Diagrams for deriving gap compatibility constraints. (a) Top view of two gaps. (b) Perspective view of one gap. (c) Diagram of the sub-fold viewed along the sub-fold axis, looking along the arrow shown in (b). Note that the dashed lines are true length as they are parallel to the viewing plane. Solid lines are projections onto the viewing plane.

Consider the perpendicular projections of Gap 1 and Gap 2 onto a plane perpendicular to the sub-fold axis, s, Fig. 3.10c. The solid lines from s to A and s to B, and

from s to C and s to D in Gap 1 are the projections of the faces of the sub-fold. Similarly for Gap 2, the solid lines are the projections of the sub-fold faces. The dotted lines representing segments AC, BD, AC', and BD' are true lengths, since they are parallel to the projection plane.

By examining Gap 1 in Figure 3.10c, it is observed that

$$\sin\left(\frac{\varphi}{2}\right) = \frac{g_2 - g_1}{2||\boldsymbol{AB}||_p} \tag{3.10}$$

$$\sin\left(\frac{\varphi}{2}\right) = \frac{g_2}{2||\boldsymbol{sB}||_p}, \tag{3.11}$$

where $||\ ||_p$ denotes the length of the projection. Similarly, by examining Gap 2,

$$\sin\left(\frac{\varphi'}{2}\right) = \frac{G_2 - G_1}{2||\boldsymbol{AB}||_p} \tag{3.12}$$

$$\sin\left(\frac{\varphi'}{2}\right) = \frac{G_2}{2||\boldsymbol{sB}||_p}. \tag{3.13}$$

Assuming that Gap 1 and Gap 2 are two different configurations of the same sub-fold, for different angles φ and φ', the projected lengths $||\boldsymbol{AB}||_p$ and $||\boldsymbol{sB}||_p$ are the same for Gap 1 and Gap 2. By combining Eqs. (3.10)- (3.13), the following relation between the two gaps is obtained:

$$\frac{g_2 - g_1}{g_2} = \frac{G_2 - G_1}{G_2}. \tag{3.14}$$

The condition in Eq. (3.14) is equivalent to the statement that $\frac{g_2 - g_1}{g_2}$ is invariant as the sub-fold changes angle. Equation (3.14) can be used as a condition on any two gaps to ensure that they can be obtained as two different configurations of the same sub-fold.

3.5 Pattern synthesis

The synthesis of kirigami fold patterns capable of achieving multiple target surfaces with different Gaussian curvature is formulated as a tile arrangement problem. The objective is to compute a single tile arrangement that can be reconfigured, by varying the sub-fold angles, to achieve each target surface. The tiles are simultaneously arranged on all of the target surfaces, while ensuring that the following conditions are satisfied:

1. Adjacent tiles can be connected by a single sub-fold (Eqs (3.8) and (3.9)).
2. Corresponding gaps between tiles in each target surface tile arrangement are compatible (Eq. (3.14)).

The computation of the tile arrangements involves the solution of a constrained optimization problem, which can be solved using standard nonlinear optimization techniques. After generating a valid set of tile arrangements on each of the target surfaces, the sub-folds are added to any one of the arrangements to fill in the gaps. This completes the synthesis of the fold pattern. Since the tile arrangements corresponding to each target surface are compatible by design, the pattern can be reconfigured with the tiles taking on any of the computed arrangements.

An overview of the pattern synthesis process is presented in Figure 3.11. First, a set of initial guesses of the tile arrangements are generated, corresponding to each target surface. The initial guesses can be generated systematically using a discretization of the target surfaces. A flat target surface is included to achieve a developable pattern. The constrained optimization problem uses the initial guesses as a starting point, and outputs valid arrangements of the tiles on each target surface. Then, sub-folds are added to the arrangement corresponding to the flat target surface, completing the developable fold pattern.

3.5.1 Constrained optimization problem

Valid arrangements of the tiles corresponding to each target surface are obtained by solving a constrained optimization problem. The vector $\boldsymbol{v}_j \in \mathbb{R}^{3n_{vt}N_t}$ contains the vertex coordinates of an arrangement of N_t identical tiles corresponding to target surface $T_j(x, y) : \mathbb{R}^2 \to \mathbb{R}$. Various tile shapes can be considered and the number of vertices per tile is n_{vt}. There are N_s tile arrangements, each corresponding to one of the N_s target surfaces. The set of tile arrangements is parameterized by

$$\boldsymbol{V} = \begin{bmatrix} \boldsymbol{v}_1 \\ \vdots \\ \boldsymbol{v}_j \\ \vdots \\ \boldsymbol{v}_{N_s} \end{bmatrix}, \tag{3.15}$$

where $\boldsymbol{V} \in \mathbb{R}^{3n_{vt}N_tN_s}$ is a vector of tile vertex coordinates in all N_s arrangements. Each arrangement of tiles has N_g gaps, which determines the connectivity of the tiles as each gap is replaced by a sub-fold after the tile arrangements are computed.

To generate a set of tile arrangements, a constrained optimization problem is posed to minimize a cost function E subject to a set of equality constraints:

$$\min_{\boldsymbol{V}} E(\boldsymbol{V}) \quad \text{subject to} \quad C_{tiles}(\boldsymbol{V}),\ C_{gaps}(\boldsymbol{V}),\ C_{target}(\boldsymbol{V}), \tag{3.16}$$

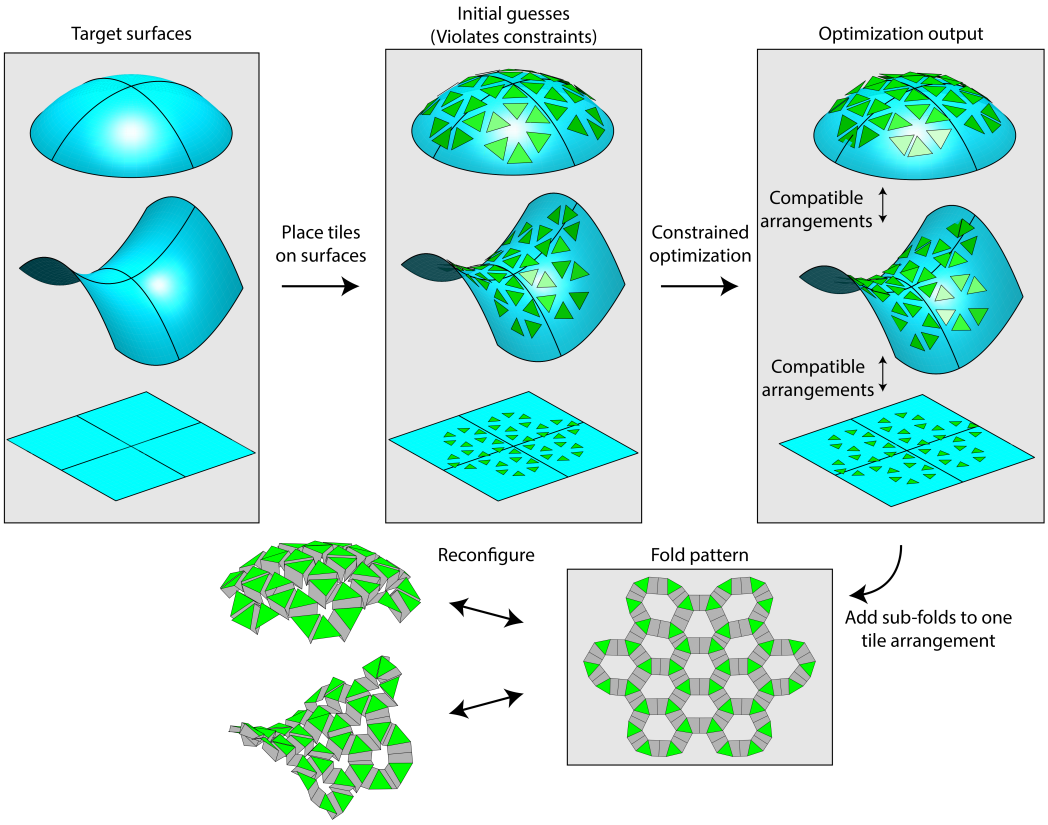

Figure 3.11: Overview of pattern synthesis process. First, an initial guess is created by arranging tiles on each target surface. By solving a constrained optimization problem, compatible tile arrangements corresponding to each target surface are computed. Then, sub-folds are added to connect adjacent tiles in one of the tile arrangements. By adding sub-folds to a flat target surface arrangement, a developable pattern is created that can be reconfigured to achieve the other tile arrangements.

where the choice of the cost function E depends on the specific application. A suitable option for the cost function is proposed in Section 3.5.3. The constraints have been divided into three sets: C_{tiles}, C_{gaps}, C_{target}.

The first set of constraints, C_{tiles}, defines the shape of the tiles. In the case of equilateral triangle tiles, denote by L_{mj} the length of tile edge m in arrangement j. The length of all tile edges in all arrangements is set equal to L_0 and hence,

$$C_{tiles}^{triangle} = \{L_{mj} = L_0, \quad m = 1, ..., 3N_t, \quad j = 1, ..., N_s\}. \tag{3.17}$$

For square tiles, extra constraints are needed to define the shape of the tile. Again, the length of edge m in arrangement j is fixed at L_0. The length of the diagonal L_{ij}^D of each tile i in arrangement j is fixed at $\sqrt{2}L_0$. An additional constraint is added to enforce the coplanarity of the four vertices of each tile. For square tiles with edge

length L_0 and corner points (q_1, q_2, q_3, q_4), the corresponding tile constraint set is

$$C_{tiles}^{square} = \{L_{mj} = L_0, \qquad m = 1, ..., 4N_t, \quad j = 1, ..., N_s \tag{3.18}$$

$$L_{ij}^{D} = \sqrt{2}L_0, \qquad i = 1, ..., N_t, \quad j = 1, ..., N_s \tag{3.19}$$

$$(\mathbf{q}_2\mathbf{q}_1 \cdot \mathbf{q}_3\mathbf{q}_1 \times \mathbf{q}_4\mathbf{q}_1)_{ij} = 0, \quad i = 1, ..., N_t, \quad j = 1, ..., N_s\}. \tag{3.20}$$

Equations (3.18) and (3.19) define the side lengths and diagonal length of the square, and Eq. (3.20) enforces the planarity of the tile. Other tile shapes could also be considered, and would be formulated in a similar way.

The second set of constraints, C_{gaps}, ensures a valid set of gaps in all tile arrangements. Following Section 3.4, C_{gaps} ensures that a single sub-fold can be inserted in each gap between adjacent tiles and that corresponding gaps in each of the target surface tile arrangements are compatible. The gap constraints can be written as

$$C_{gaps} = \{ (\boldsymbol{BA} \times \boldsymbol{CA} \cdot \boldsymbol{DA})_{kj} = 0, \qquad k = 1, ..., N_g, \quad j = 1, ..., N_s, \tag{3.21}$$

$$(||\boldsymbol{AD}|| = ||\boldsymbol{BC}||)_{kj}\,, \qquad k = 1, ..., N_g, \quad j = 1, ..., N_s, \tag{3.22}$$

$$\left(\frac{g_{2k} - g_{1k}}{g_{2k}}\right)_j = \left(\frac{g_{2k} - g_{1k}}{g_{2k}}\right)_{j=1}, \quad k = 1, ..., N_g, \quad j = 2, ..., N_s\} \tag{3.23}$$

where k indexes each gap in target arrangement j. Equations (3.21) and (3.22) enforce the condition that a single sub-fold can be added in each gap. Equation (3.23) ensures compatibility of corresponding gaps in the arrangement of the tiles for each target surface. For brevity of notation, it is omitted that all constraints are functions of $\boldsymbol{V}$.

The third set of constraints, C_{target}, ensures that each target surface is closely approximated by its corresponding tile arrangement configuration. Sections 3.5.2-3.5.4 discuss appropriate target surface constraints.

3.5.2 Ideal target constraints

To obtain the closest approximation of the target surfaces, a tile arrangement is defined as *ideal* if each tile is tangent to the target surface at the tile center. Then, the constraint set C_{target}^{ideal} is defined to strictly enforce that the arrangements are all ideal.

The centroid coordinates of tile i in target arrangement j are $(\bar{x}_{ij}, \bar{y}_{ij}, \bar{z}_{ij})$. The unit normal vector of the tile is $\hat{\mathbf{n}}_{ij}^{t} \in \mathbb{R}^3$. The target surface j, defined by the function $T_j(x, y)$, has unit normal vector $\hat{\mathbf{n}}_{j}^{s}(x, y) \in \mathbb{R}^3$. In this work, it is assumed that the analytical expressions for the target surfaces are known, however, similar

constraints could be formulated in terms of a set of numerically defined target surfaces. The constraints that force all arrangements to be ideal approximations of the target surfaces are:

$$C_{target}^{ideal} = \{\bar{z}_{ij} = T_j(\bar{x}_{ij}, \bar{y}_{ij}), \qquad i = 1, ..., N_t, \quad j = 1, ..., N_s \tag{3.24}$$

$$\Theta_{ij} = 0, \qquad i = 1, ..., N_t, \quad j = 1, ..., N_s\}, \tag{3.25}$$

where the angle Θ_{ij} is the angle between the unit normal vector $\hat{\mathbf{n}}_{ij}^t$ of tile i in arrangement j and the unit normal vector $\hat{\mathbf{n}}_j^s$ of surface T_j, evaluated at the tile center

$$\Theta_{ij} = \cos^{-1}\left(\hat{\mathbf{n}}_{ij}^t \cdot \hat{\mathbf{n}}_j^s(\bar{x}_{ij}, \bar{y}_{ij})\right). \tag{3.26}$$

The first constraint, Eq. (3.24), ensures that the tile centers lie on the target surface. Equation (3.25) ensures that the tile normal is aligned with the surface normal at the center of the tile, so that the tile is tangent to the surface.

Although it is difficult to make general statements about the existence of feasible solutions to systems of nonlinear equations, a constraint and free variable counting argument can be used to determine if the system is generically overdetermined or underdetermined. When subject to the ideal constraints, each tile effectively has three free parameters. The centroid coordinates $\bar{x}$ and $\bar{y}$ of each tile are free, but $\bar{z}$ follows from Eq. (3.24). If Eq. (3.25) is satisfied, the only remaining free parameter is an angular rotation about the tile normal vector. Therefore, by considering all N_t tiles in N_s arrangements, there are effectively $3N_sN_t$ free variables. Since C_{tiles} and C_{target} have already been accounted for while counting the free variables, the number of free variables can be compared to the number of constraints in C_{gaps}. From Eqs. (3.21)-(3.23), there are $(3N_s - 1)N_g$ gap constraints. If the number of gap constraints is greater than the number of free variables, the system is overdetermined and, in general, there will be no solution.

Table 3.1 summarizes the number of free variables versus gap constraints if the ideal target constraints are enforced. The freedom in the tile arrangement problem is defined as the number of free variables minus the number of gap constraints, denoted by F. If $F > 0$, the problem is underdetermined and feasible solutions should exist, while $F < 0$ indicates that the problem is overdetermined.

Whether or not the system is overdetermined depends on the connectivity of the tiles, particularly the number of tiles N_t, the number of gaps N_g, and the number of target surfaces N_s. Section 3.6 analyzes the freedom in the tile arrangement

problem for tiles with different connectivity. The analysis suggests that the ideal target constraints are often too restrictive and tend to over-constrain the system. This motivates the relaxation of some target constraints, discussed in the next sections.

Table 3.1: Count of free variables and constraints for three target constraint cases.

	Free variables	Gap constraints	F = Free variables − Gap constraints
Ideal target constraints	$3N_sN_t$	$(3N_s-1)N_g$	$3N_sN_t-(3N_s-1)N_g$
Relaxed target constraints	$5N_sN_t$	$(3N_s-1)N_g$	$5N_sN_t-(3N_s-1)N_g$
Relaxed target constraints and developability	$5(N_s-1)N_t+3N_t$	$(3N_s-1)N_g$	$5(N_s-1)N_t+3N_t$ $-(3N_s-1)N_g$

3.5.3 Relaxed target constraints and cost function

Depending on the connectivity of the tiles, the ideal target constraints may over-constrain the tile arrangement problem. In such cases, it is of interest to consider relaxing the constraints to obtain feasible solutions. A relaxed target constraint set is proposed that maintains the constraint that the tile center must lie on the target surface, but relaxes the constraint that the tile normal must be aligned with the surface normal. The resulting constraint set is

$$C^{relax}_{target} = \{\bar{z}_{ij} = T_j(\bar{x}_{ij}, \bar{y}_{ij}), \quad i = 1, ..., N_t, \quad j = 1, ..., N_s\}. \tag{3.27}$$

A similar constraint counting argument to that presented in Section 3.5.2 can be applied to the relaxed constraints. The placement of each tile has five free variables: two free variables to describe the tile center coordinates $\bar{x}$ and $\bar{y}$ and three angular orientation variables, since the tile normal vector is no longer constrained. The count of free variables and gap constraints for the relaxed target constraint case is included in Table 3.1.

Since the tile normal vectors are no longer required to be aligned with the surface normal vector, the deviation between the tile and the surface normals can be incorporated in the cost function in Eq. (3.16). A suitable cost function is:

$$E = E_{normal} + wE_{gap}. \tag{3.28}$$

The first term in the cost function is

$$E_{normal} = \left|\left|\left|\left[\Theta_{11}, ..., \Theta_{ij}, ..., \Theta_{N_tN_s}\right]\right|\right|\right|, \tag{3.29}$$

which is the norm of a vector whose entries are the angles between the tile normals and the surface normals, Θ_{ij}, defined in Eq. (3.26) for all tiles in all target arrangements. This term penalizes the misalignment between the tiles and the target surface. However, including only E_{normal} in the cost function would allow optimal solutions with undesirable tile spacing. For example, some gaps between adjacent tiles could be very large and others very small. To address the tile spacing, a second term, E_{gap}, has been introduced in Eq. (3.28) to control the gap sizes. This term is defined as:

$$E_{gap} = ||\boldsymbol{G} - \boldsymbol{G}_{tar}||, \tag{3.30}$$

where $\boldsymbol{G} \in \mathbb{R}^{2N_gN_s}$ is a vector of gap lengths g_1 and g_2 for each gap of each arrangement. It is given by:

$$\boldsymbol{G} = \left[g_{111},\ g_{211}\ \ldots,\ g_{1kj},\ g_{2kj},\ \ldots,\ g_{1N_gN_s},\ g_{2N_gN_s}\right], \tag{3.31}$$

where k indexes gaps of arrangement j. The term E_{gap} penalizes the deviation from a specified vector of target gap sizes $\boldsymbol{G}_{tar} \in \mathbb{R}^{2N_gN_s}$. The relative weighting between the two terms in the cost function in Eq. (3.28) is w.

3.5.4 Including the developability target

A developable pattern can be obtained by including a flat target surface. However, it should be noted that in the case of the relaxed target constraints, the tile arrangement corresponding to the flat target surface may not be exactly planar. A third set of target constraints $C_{target}^{relax,dev}$ is proposed that treats the flat target surface with ideal constraints and all other target surfaces with relaxed target constraints. Let target surface 1 be flat; the relaxed developable constraint set is

$$C_{target}^{relax,dev} = \{\bar{z}_{ij} = T_j(\bar{x}_{ij}, \bar{y}_{ij}), \qquad i = 1, ..., N_t, \quad j = 1, ..., N_s \tag{3.32}$$

$$\Theta_{ij} = 0, \qquad i = 1, ..., N_t, \quad j = 1\}. \tag{3.33}$$

Again, the free variables and gap constraints can be counted. By requiring that tile arrangement 1 is satisfied exactly (ideal target), there are $3N_t$ free variables associated with the tiles in arrangement 1 and $5N_t(N_s - 1)$ free variables associated with the other target arrangements. The count of free variables versus gap constraints is presented in Table 3.1.

Since the flat target arrangement is restricted to lie exactly in the plane, a developable pattern can be made by adding sub-folds to a flat tile arrangement. This results in a planar configuration that defines the fold pattern.

3.5.5 Implementation

The constrained optimization problem of Eq. (3.16) can be implemented numerically to compute the optimal arrangements that satisfy the constraints. Standard nonlinear optimization algorithms can be used to perform the optimization. The *fmincon* utility in Matlab was used to compute optimal tile arrangements in the examples presented in this chapter.

First, the type of tile, the number of tiles, and their connectivity are chosen. Then, depending on the chosen connectivity and whether or not the pattern is to be developable, the appropriate target constraint set is chosen. Next, the numerical implementation of the pattern synthesis process begins. An initial guess of the tile arrangements for each target surface is made. Since the initial guess may violate the constraints, it can be created by placing tiles on discretizations of the target surfaces. First, a uniform grid of equilateral triangles or squares, depending on the tile shape, is created in the xy-plane. A discretization of each target surface can be created by mapping the vertices of that grid to each target surface $\boldsymbol{T}_j(x, y)$. Then, a tile is placed in the center of each face of the discretized target surface to produce an initial guess tile arrangement for each target surface.

In all of the subsequent examples, the cost function proposed in Eq. (3.28) was used to derive optimal tile arrangements and the target gap size $\boldsymbol{G}_{tar}$ must be specified for each gap. Upon computing an optimal arrangement of tiles, the sub-folds must be added to one of the tile arrangements to complete the pattern. To create a developable pattern, the sub-folds can be added to the flat arrangement of tiles in the plane of the tiles. In this case, care should be taken to ensure that the gaps of the flat tile arrangement are larger than corresponding gaps in the other arrangements, which can be achieved by setting a larger target gap size in the cost function for the flat tile arrangement. To create a non-developable pattern, sub-folds can be added to any of the tile arrangements. In this case, the size of each sub-fold can be chosen freely. For example, the distance from point s_1 of Fig. 3.8 to the plane of the tile edges can be specified. After inserting the sub-folds, the pattern synthesis is complete and numerical simulations can verify that the resulting pattern can be reconfigured into each of the target surface arrangements.

3.6 Pattern connectivity

Before implementing the pattern synthesis process, the shape and connectivity of the tiles must be decided. Both the shape and connectivity of the tiles determine

the number of constraints in the optimization problem of Eq. (3.16). This section provides insight into the role of tile connectivity by analyzing various sizes of equilateral triangle and square tile patterns. Specifically, the freedom F in the tile arrangement problem and the number of kinematic degrees of freedom are presented for both triangular and square tiles forming patterns of different sizes.

From Table 3.1, for the ideal target constraint set:

$$F_{ideal} = 3N_sN_t - (3N_s - 1)N_g \tag{3.34}$$

and for the relaxed target constraints with the developability constraint,

$$F_{relax,dev} = 5(N_s - 1)N_t + 3N_t - (3N_s - 1)N_g. \tag{3.35}$$

The number of target surfaces, N_s, the number of tiles, N_t, and the number of gaps, N_g, determine whether the tile arrangement problem is overdetermined or underdetermined.

To understand the role of tile connectivity, we first study triangular tile patterns. Beginning with a single loop of tiles and adding loops, the pattern connectivities considered are all six-fold rotationally symmetric. Figure 3.12a shows the tile connectivity for the 7- and 13-loop cases.

In Figure 3.12b, the freedom provided by the tile arrangement constraint set is plotted for both the ideal constraints and the relaxed constraints including the developability constraint. The limiting cases of two target shapes ($N_s = 2$) and an infinite number of target shapes have been considered. In both cases, the ideal target constraint set leads to an overdetermined system ($F < 0$) for all of the patterns considered, with the exception of the single loop. However, for the relaxed constraints, the freedom in the tile arrangement problem increases as the pattern size is increased. The relaxed constraints without the strict developability constraint provide even greater freedom. Note that even in the limiting case as the number of target surfaces N_s goes to infinity, there is freedom in the tile arrangement problem with the relaxed constraints. This suggests that solutions may be possible for a high number of target shapes, though this constraint counting study does not bring insights about the quality of possible solutions.

Square tiles arranged in a square grid have also been considered. Patterns with 4 loops and 9 loops are shown in Fig. 3.13a. The ideal target constraints lead to an overdetermined constraint set except for the single loop connectivity, as shown in

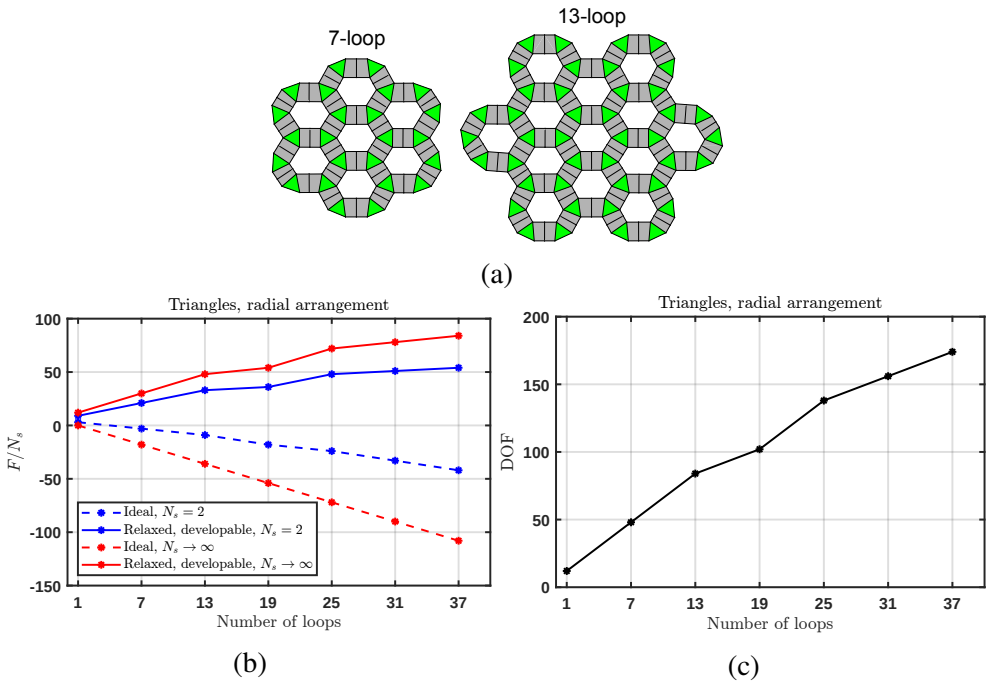

Figure 3.12: Analysis of connectivity of equilateral triangle tile patterns with six-fold rotational symmetry. (a) 7-loop and 13-loop patterns. (b) Freedom of tile arrangement problem plotted against number of loops. (c) Kinematic degrees of freedom plotted against number of loops.

Fig. 3.13b. However, the relaxed constraints including the developability constraint lead to an underdetermined constraint set only for the smaller patterns, unlike in the triangle tile connectivity cases previously considered. This difference is because the number of gaps N_g compared to the number of tiles N_t is generally larger in square tile patterns than in triangular tile patterns.

Along with the freedom in solving the tile arrangement problem, the connectivity of the tiles determines also the number of kinematic degrees of freedom of the fold pattern, which was computed using Eq. (3.2) with no states of self stress. It was verified using the bar-hinge kinematic model in Appendix A that the patterns presented in this chapter generically have no states of self stress. The number of kinematic degrees of freedom versus the number of loops have been plotted in Figures 3.12c and 3.13c for the triangular and square tile patterns. For both the triangular and square tile patterns, the number of degrees of freedom increases as the pattern increases in size.

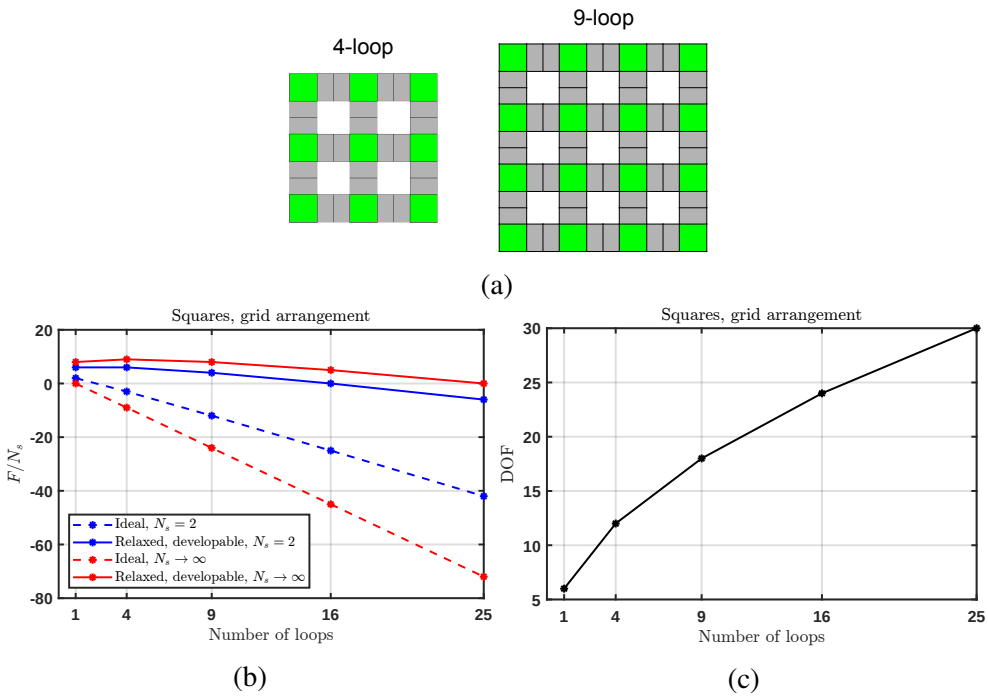

Figure 3.13: Analysis of connectivity of square tile patterns with four-fold rotational symmetry. (a) 4-loop and 9-loop patterns. (b) Freedom of tile arrangement problem plotted against number of loops. (c) Kinematic degrees of freedom plotted against number of loops.

3.7 Examples

To demonstrate the pattern synthesis process, three example patterns are presented. Both triangular and square tiles are considered and various numbers of target shapes are considered. A set of target surfaces is defined in Eq. (3.36) below, and the six surfaces are used throughout these examples:

$$\begin{aligned}
T_1: &\quad z = 0 \\
T_2: &\quad z = \sqrt{20 - x^2 - y^2} \\
T_3: &\quad z = \frac{1}{6}\left(x^2 - y^2\right) \\
T_4: &\quad z = \frac{4}{3}\sin\left(\frac{3}{4}x\right)\cos\left(\frac{3}{4}y\right) \\
T_5: &\quad z = \frac{1}{32}(x^3 - 3xy^2) \\
T_6: &\quad z = 5\sqrt{\frac{3}{2} - \frac{x^2}{32} - \frac{5y^2}{68}}.
\end{aligned} \tag{3.36}$$

The scaling of the target functions is with respect to a unit tile side length. The target functions include surfaces with a range of Gaussian curvatures. Target surface T_1 is

flat (zero curvature), which can be included to create a developable pattern. Surface T_2 is spherical (positive Gaussian curvature). Surface T_3 is a hyperbolic paraboloid, which defines a saddle shape (negative Gaussian curvature). In T_4, a sinusoidal surface, there are some regions of both positive and negative curvature. Surface T_5 is known as a monkey saddle, with negative curvature everywhere except the origin, which has zero curvature. Finally, T_6 is an ellipsoidal surface with positive Gaussian curvature. Figure 3.14 shows plots of the target surfaces.

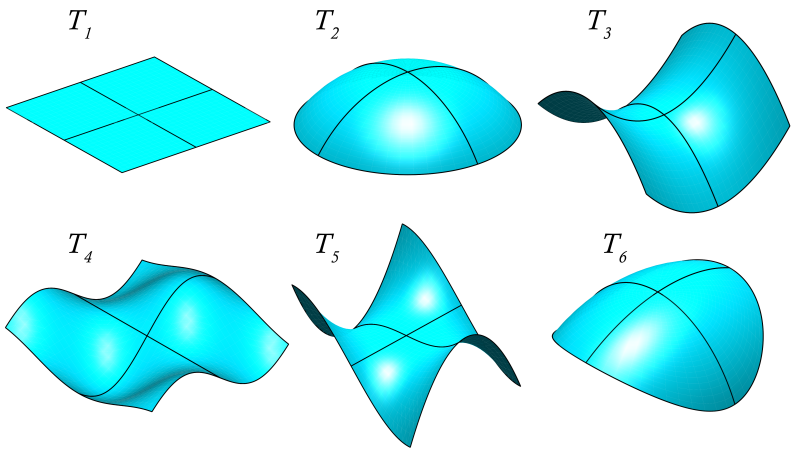

Figure 3.14: Target surfaces used in the pattern synthesis examples.

The following sections present the synthesis of three kirigami patterns. After the pattern synthesis process computes the fold pattern, we verify that each pattern is rigidly foldable and continuous kinematic paths connect each target configuration. This is verified through kinematic folding simulations using the pathfinding algorithm in Appendix B.

3.7.1 Triangular tiles, three target surfaces

The first example considers equilateral triangular tiles with the 13-loop connectivity illustrated in Figure 3.12a. Three target surfaces are used: T_1, T_2, and T_3. Following the analysis of freedom in the tile arrangement problem in Section 3.6, the relaxed developable target constraints are adopted. Subject to these constraints, based on the free variable and constraint count of Table 3.1, the tile arrangement problem has $F/N_s = 38$ free parameters per tile arrangement.

The tile arrangement optimization problem is implemented according to Section 3.5. For T_1, the target gap size is set to $0.8L_0$ where L_0 is the tile side length. A smaller target gap size of $0.4L_0$ is used for T_2 and T_3 to ensure that when sub-folds are added to the flat tile arrangement, the T_2 and T_3 configurations can be achieved.

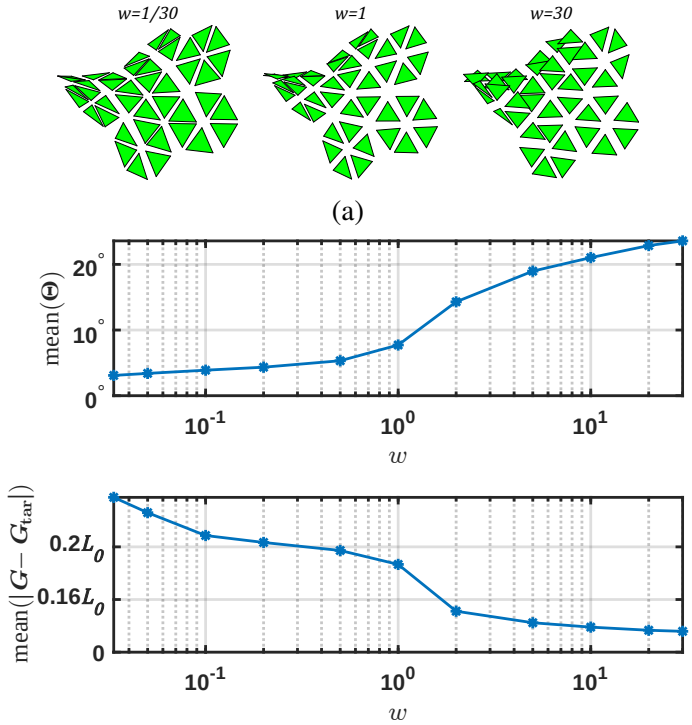

Figure 3.15: Analysis of optimal tile arrangements corresponding to target surface T_3 with varying cost function weight w for the 13-loop triangular tile example with 3 target surfaces. (a) Optimal tile arrangements corresponding to three values of w. (b) Characterization of the optimal tile arrangement for varying w, measured by the mean misalignment between tile and surface normals and mean distance to target gap size.

To explore the solution space, the weight w in the cost function of Eq. (3.28) is varied from $1/30$ to 30. Figure 3.15 characterizes the tile arrangement corresponding to target surface T_3 as w varies. A similar study could be performed for the other tile arrangements, but we focus on the T_3 arrangement to understand the role of w. The optimal tile arrangement corresponding to T_3 is shown in Fig. 3.15a for three values of w. For $w = 1/30$, the tiles align closely to the surface, but the tile spacing is irregular. Conversely, $w = 30$ produces closer to uniform tile spacing at the cost of tiles poorly aligned to the target surface. A balance is achieved with $w = 1$. Figure 3.15b quantifies the tile alignment and distance to the target gap size of the optimal tile arrangements as w varies. A desirable value for w may depend on the specific application of interest. However, to proceed with this example, $w = 1$ is selected. The corresponding mean and maximum tile misalignment and distance from target gap size are summarized in Table 3.2 for each target surface tile arrangement.

Table 3.2: Mean and maximum angle between tile and surface normal for the two target surface configurations.

Target surface	T_1	T_2	T_3
mean(Θ) (degrees)	0	6.94	8.50
max(Θ) (degrees)	0	10.22	10.91
mean($\lvert \boldsymbol{G} - \boldsymbol{G}_{tar} \rvert$)	$0.09L_0$	$0.07L_0$	$0.08L_0$
max($\lvert \boldsymbol{G} - \boldsymbol{G}_{tar} \rvert$)	$0.29L_0$	$0.30L_0$	$0.37L_0$

After computing the tile arrangements, sub-folds are added to the flat tile arrangement in the plane of the tiles, resulting in a planar fold pattern. The fold pattern can then be folded into the T_2 and T_3 configurations. Upon closing the sub-folds, a flat apparent surface can be created which we denote T_0. The T_0 configuration does not correspond to a target surface, but it is guaranteed to exist by the gap constraints of Section 3.4. Figure 3.16 shows the four configurations of the pattern.

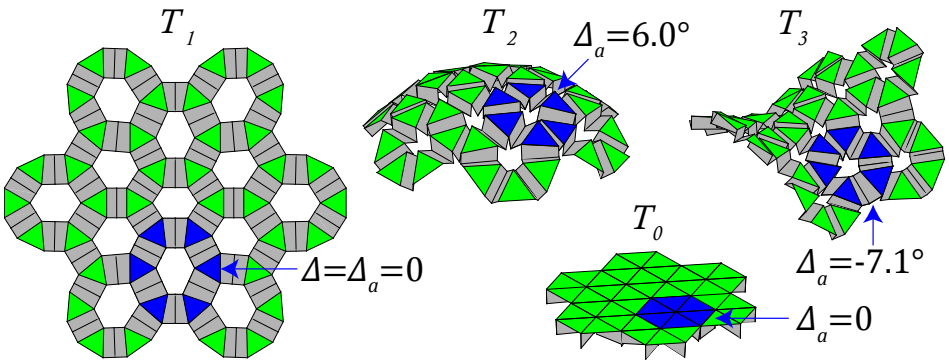

Figure 3.16: Example of a developable kirigami pattern with equilateral triangle tiles designed to achieve target surfaces T_1, T_2, and T_3.

In Figure 3.16, one loop of triangles is highlighted in blue. As shown in the T_1 configuration, the pattern can be flattened so the intrinsic curvature of the loop is zero. To achieve zero intrinsic curvature, trapezoidal gaps of both orientations are present in the loop. This follows the discussion of Section 3.3, since the angles of the trapezoidal gaps around the loop must sum to zero for developability.

The apparent curvature of each loop varies between each configuration. In the T_2 configuration, the pattern exhibits positive apparent curvature, and the blue loop has an apparent angular defect of $\Delta_a = 6.0°$. Alternatively, the T_3 configuration exhibits negative apparent curvature, and the blue loop has an apparent angular defect of $\Delta_a = -7.1°$.

3.7.2 Square tiles, two target surfaces

This example demonstrates the pattern synthesis process for square tiles. We consider a pattern with two target surfaces, T_2 and T_3; by omitting the flat target surface, a non-developable pattern is created. A pattern connectivity with nine loops is considered. With $N_t = 16$, $N_g = 24$, and $N_s = 2$, the relaxed constraints (without developability) lead to a tile arrangement problem with $F/N_s = 20$ free parameters per tile arrangement.

Target gap sizes $0.8L_0$ and $1.2L_0$ are used for the spherical and saddle tile arrangement, respectively. The cost function weight is taken as $w = 0.25$, favoring normal vector alignment over gap spacing. In Table 3.3, the mean and maximum tile misalignment along with the deviations from target gap sizes are listed for the optimal tile arrangements.

Once the tile arrangements are computed, sub-folds are added to the T_2 tile arrangement. The size of the sub-folds is determined by specifying the distance from s_1 to plane $ABCD$ for each gap, as labeled in Figure 3.8. This distance is chosen to be $0.4L_0$ for all sub-folds, resulting in the pattern shown in Figure 3.17.

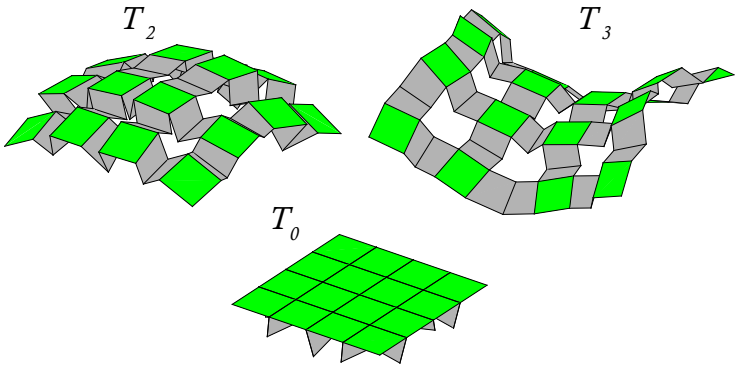

Figure 3.17: Example of a non-developable kirigami pattern with square tiles designed to achieve two target surfaces.

Table 3.3: Mean and maximum angle between tile and surface normal for the square tile pattern with two target surfaces.

Target surface	T_2	T_3
mean(Θ) (degrees)	7.92	10.43
max(Θ) (degrees)	9.07	11.95
mean($\lvert \boldsymbol{G} - \boldsymbol{G}_{tar} \rvert$)	$0.23L_0$	$0.25L_0$
max($\lvert \boldsymbol{G} - \boldsymbol{G}_{tar} \rvert$)	$0.49L_0$	$0.76L_0$

3.7.3 Triangular tiles, six target surfaces

In the final example, we demonstrate the capability of the pattern synthesis process by including all six target surfaces. Again, triangular tiles in the 13-loop connectivity are considered. For the target constraints, the relaxed developable set is used. In the cost function, the target gap size is set to $0.8L_0$ for the T_1 tile arrangement and $0.4L_0$ for all other tile arrangements. The cost function weight is set at $w = 1$. Once the optimal tile arrangements are computed, sub-folds are added to the T_1 tile arrangement in-plane to ensure developability. The resulting pattern is shown in Figure 3.18 in the configurations corresponding to target surfaces T_1 through T_6 along with T_0 where the sub-folds are fully closed.

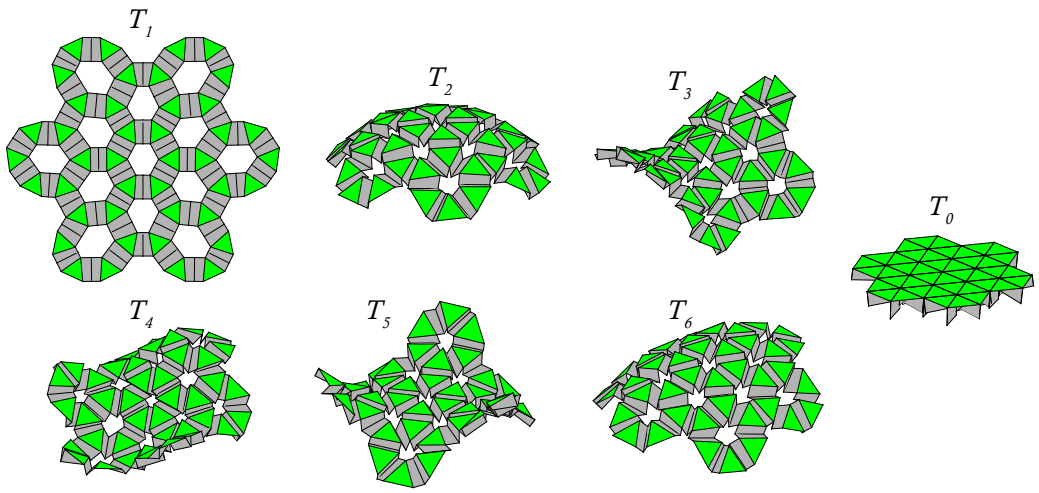

Figure 3.18: Example of a kirigami pattern with equilateral triangle tiles designed to approximate six target surfaces.

Table 3.4 lists the mean and maximum tile misalignment along with the deviations from target gap sizes for the optimal tile arrangements. Compared to the case with only three target shapes, the normal vector offset and distance to target gap size of T_1, T_2, and T_3 are slightly larger. Since the problems were set up with identical target gap sizes and cost function weight, this suggests that adding extra target shapes sacrifices the quality of the tile arrangements. However, this generally would depend on the specific target surfaces, tile connectivity considered, and cost function parameters.

3.8 Prototype

The presented family of fold patterns exhibit relatively simple geometry from the manufacturing standpoint, since they avoid having dense, detailed creases and they can be made developable. This is demonstrated by a physical prototype of the triangular tile pattern with six target surfaces. The aim of this prototype is to

Table 3.4: Mean and maximum angle between tile and surface normal for the 6 target surface pattern.

Target surface	T_1	T_2	T_3	T_4	T_5	T_6
mean(Θ) (degrees)	0	7.59	8.55	11.15	9.38	6.25
max(Θ) (degrees)	0	11.18	14.04	19.33	15.99	11.29
mean($\lvert \boldsymbol{G} - \boldsymbol{G}_{tar} \rvert$)	$0.12L_0$	$0.07L_0$	$0.08L_0$	$0.10L_0$	$0.11L_0$	$0.06L_0$
max($\lvert \boldsymbol{G} - \boldsymbol{G}_{tar} \rvert$)	$0.31L_0$	$0.27L_0$	$0.38L_0$	$0.36L_0$	$0.26L_0$	$0.20L_0$

capture the rigid folding kinematics of the pattern to achieve the six target surface configurations.

The model is constructed from 3D printed plates made of nylon 12 plastic connected by steel pin hinges. This fabrication concept is appealing because it offers clean rigid-folding kinematics since the plates are stiff and the pin hinges have a well-defined axis of rotation. Although the entire model consists of many individual pieces, assembly simply requires sliding in the pin connections. It should also be noted that while this prototype is developable, the fabrication concept does not require developability.

Photos of the hinge design are shown in Figure 3.19 for two tiles connected by a sub-fold. The pins have a 1 mm diameter and the plates are 2.5 mm thick, making the plates sufficiently stiff to exhibit nearly rigid-folding kinematics. To accommodate the thickness of the plates, both faces of the sub-fold are split in half. A slender arm reaches from one face of the sub-fold to the other to ensure alignment of the hinge. With this design, the sub-fold is capable of fully closing and the desired kinematics are preserved, accommodating for the plate thickness.

A prototype of the entire pattern is created by applying the sub-fold design concept shown of Figure 3.19 to the dimensions of each sub-fold in the pattern. The prototype is shown in Figure 3.20 in each of the six target surface configurations, as well as the T_0 configuration with the sub-folds closed. Since the pattern has 84 kinematic degrees of freedom, positioning the pattern into each target surface configuration is a challenge. To address this challenge, a 3D printed support structure for each configuration is used. The support structure consists of triangular posts under the position of each tile in the target configuration. A groove on the underside of the tiles allows the prototype to fit on the support structure. Figure 3.21 shows the support structure with and without the prototype for the T_3 (saddle) configuration. Once the prototype is properly positioned on the support, a small amount of glue is placed on each hinge allowing the prototype to hold its configuration when removed

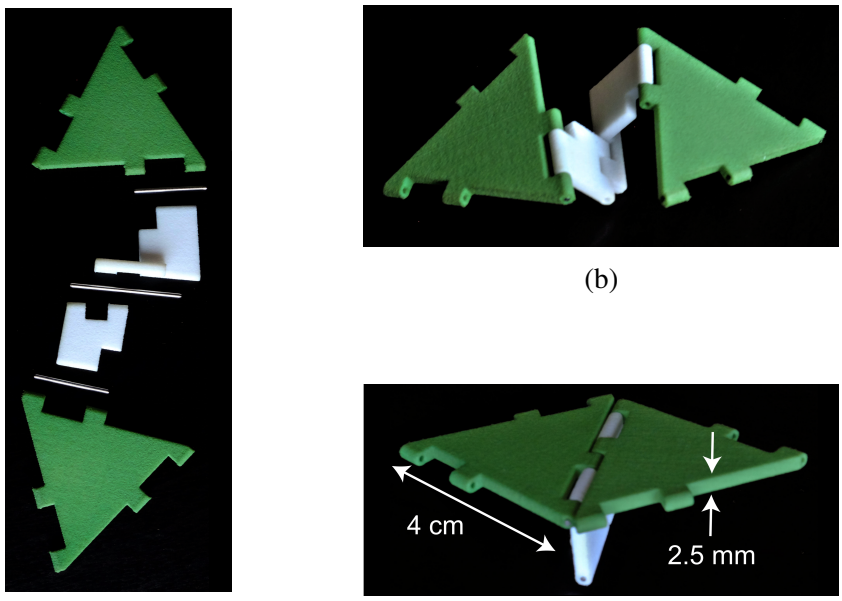

(a) (b) (c)

Figure 3.19: Hinge design concept demonstrated on two tiles connected by a sub-fold. (a) Exploded view of the 3D printed plates and pin hinges. (b) A configuration with the sub-fold partially open. (c) A configuration with the sub-fold closed.

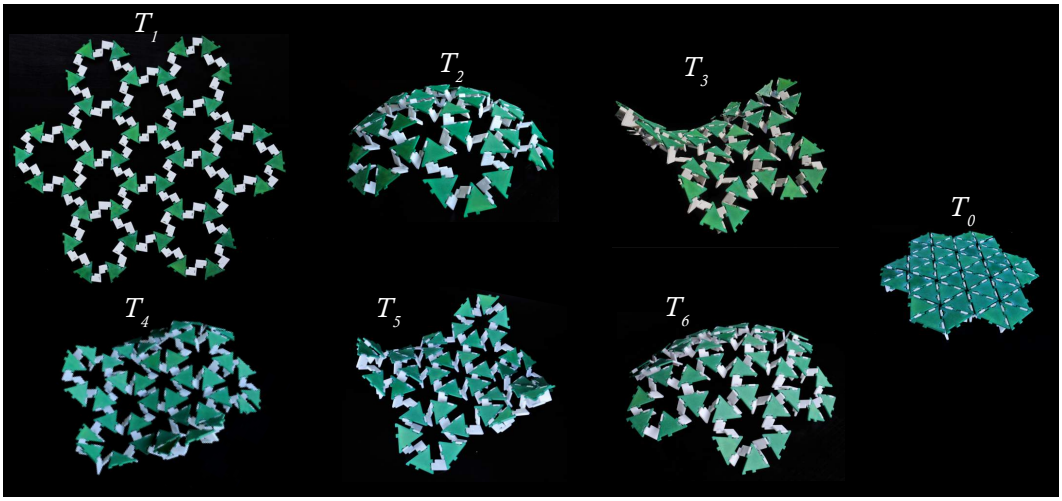

Figure 3.20: Prototype in the six target surface configurations and the T_0 configuration with the sub-folds closed.

from the support structure. The bond of the glue on each hinge can then be snapped, freeing the hinges so the next target configuration can be achieved.

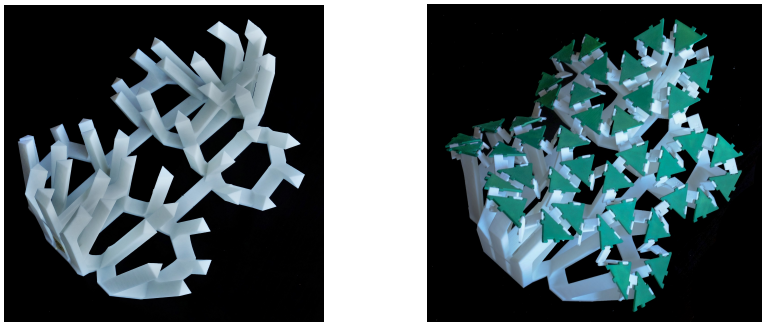

(a) (b)

Figure 3.21: A 3D printed support structure is used to position the prototype in the target surface configurations. (a) Support structure for the T_3 (saddle) configuration. (b) The prototype positioned on the support structure.

3.9 Conclusions

In this chapter, the synthesis of a new family of kirigami patterns has been presented. These patterns are capable of approximating multiple target surfaces of varying Gaussian curvature. The patterns, which consist of a set tiles connected by sub-folds, can vary the apparent curvature of the surface comprised of only tiles. Changing the sub-fold angles serves as a mechanism for changing the apparent curvature of the pattern, leading to patterns capable of achieving a large range of apparent curvature.

A numerical framework for pattern synthesis has been presented, which is posed as a tile arrangement problem. Arrangements of tiles corresponding to each target surface are simultaneously computed by solving a constrained optimization problem. The constraints are formulated to ensure that sub-folds can be added between adjacent tiles and that each arrangement is compatible with the others. Additionally, constraints are included to ensure that the arrangements closely approximate the target surfaces and both developable and non-developable patterns can be created. Upon computing tile arrangements, sub-folds are added to connect adjacent tiles in one arrangement, completing the pattern synthesis. Since all tile arrangements are compatible, the pattern is capable of reconfiguring to realize each target surface tile arrangement.

While these fold patterns exhibit the freedom to take on a range of curved surfaces, their many kinematic degrees of freedom present a challenge. To achieve practical application of such patterns, load-bearing capacity in each target configuration and reconfiguration between target configurations must be addressed, which presents a challenge for fold patterns with many degrees of freedom. This provides motivation

for the remainder of the thesis, which develops the concept of multi-configuration rigidity to address these challenges.

Chapter 4

MULTI-CONFIGURATION RIGIDITY: THE STATICALLY DETERMINATE CASE

4.1 Introduction

This chapter develops a theoretical foundation and systematic design process for multi-configuration rigidity. As demonstrated in the introductory example of Chapter 2, embedding springs and unilateral constraints to achieve rigidity in multiple target configurations is an effective solution for achieving load-bearing capacity in many-DOF structures. The kirigami patterns of Chapter 3 provide further motivation for rigorously developing a design methodology for multi-configuration rigidity, which is formulated generally for discrete structures.

Discrete structures comprised of rigid components, such as rigid bars connected by pin-joints or rigid plates connected by hinges, are typically categorized as rigid structures or as mechanisms. Rigid structures cannot deform at all, under the assumption that all components of the structure are rigid. Conversely, mechanisms are *kinematically indeterminate*, meaning that the structure can move without deforming its components. The fundamental question of whether a structure is rigid or kinematically indeterminate is the subject of the theory of rigidity [71]. Rigidity theory is a kinematic theory; the classification of a structure as rigid or kinematically indeterminate is entirely defined by its geometry. In this chapter, we bring a new perspective to rigidity by studying structures that are not rigid when considering only kinematics, but can be made rigid by the combination of unilateral constraints (e.g., contact or cables) and an applied force that engages the unilateral constraints. Such a structure is rigid, but only up to some finite perturbation force where the unilateral constraint reactions (e.g. contact or cable forces) are overcome. In this chapter, the statically determinate case is considered, when the unilateral reactions are unique, which is explicitly defined in Section 4.3.2.

Structures with unilateral constraints have been studied from the perspective of rigidity theory. The rigidity of tensegrity structures, which contain tension-only cables and compression-only struts, is covered by an extensive literature [72–74]. Furthermore, linkages that are rigid due to self contact give another example of rigidity due to unilateral constraints [75]. These studies, however, do not consider

the case of a structure with unilateral constraints that becomes rigid only under the application of an external force.

To achieve rigidity due to unilateral constraints and an applied force, it is of particular interest when the force is passively applied by a set of springs embedded throughout the structure. Specifically, we consider structures comprised of three ingredients: (i) a kinematically indeterminate *skeleton* structure, (ii) a set of unilateral constraints, and (iii) a set of springs. A design problem is posed to compute spring parameters such that a set of target configurations are rigid. Since the conditions for rigidity in each target configuration involve linearized kinematics, the resulting design problem can be formulated as a linear program.

In Section 4.2, a simple example is presented as a conceptual introduction. Section 4.3 derives conditions for when a configuration is held rigidly by an applied force and unilateral constraints. Building upon these conditions, Section 4.4 poses a design problem to embed springs throughout a structure to rigidify multiple configurations while maximizing the critical perturbation forces in each configuration. In Section 4.5, an example is presented where a 2-degree-of-freedom linkage is designed to have four rigid configurations.

4.2 A simple example

To illustrate the concept of rigidity due to a force and unilateral constraint, we begin with a simple example. Consider a rigid bar of unit length pinned at one end, as shown in Figure 4.2. The bar represents the skeleton structure, a one degree of freedom mechanism described by the rotation θ about the pinned end. The tip of the bar has coordinates (x, y). A unilateral constraint restricts the bar to $y \geq 0$, which is depicted in Figure 4.1 as a rigid platform that the bar cannot pass through. The reaction force in the unilateral constraint is μ. A force $\boldsymbol{f}$ is applied to the tip of the bar.

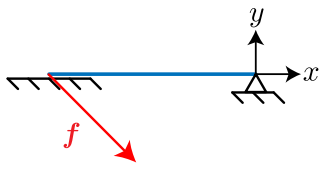

Figure 4.1: Introductory example of a bar pinned at one end made rigid due to an applied force $\boldsymbol{f}$ that maintains contact with a unilateral constraint.

This example can be viewed from two perspectives. The first is that there are no admissible displacements, which arises from the two conditions associated with the

unilateral constraint:

$$\begin{aligned} \mu &\geq 0 \\ \mu y &= 0. \end{aligned} \tag{4.1}$$

That is, the contact force must be non-negative and the contact force must be zero if there is no contact. From the second condition, it is evident that a nonzero μ requires the tip of the bar to stay at $y = 0$. In other words, displacements are not allowed as long as $\mu > 0$. The condition for rigidity is that f_y, the y-component of $\boldsymbol{f}$, is negative. This leads to a positive μ and therefore rigidity.

The second perspective comes from considering perturbation forces. If an upward perturbation force P is additionally applied to the tip of the bar, the bar will not move for $P < -f_y$. In this case, the reaction force $\mu = -f_y - P > 0$ becomes smaller due to P, but stays positive requiring that contact still occurs. For a large enough P, μ must be negative to satisfy equilibrium; since a negative contact force is forbidden, the bar will lift off the contact. The *critical perturbation force* $P^* = -f_y$ represents the smallest force that overcomes the unilateral reaction.

Building from the concept of rigidity due to a force and unilateral constraints, multi-configuration rigidity occurs when the force is applied by a spring. Consider a linear extensional spring with stiffness k and rest length l^0 connecting the tip of the bar to the point $(0, -1)$, as shown in Figure 4.2a. The spring force is $\sigma = k(\sqrt{2} - l^0)$. The requirement for a positive contact force (therefore rigidity) is that the y-component of the spring force is negative: $k(\sqrt{2} - l^0)/\sqrt{2} < 0$, which is satisfied if $l^0 < \sqrt{2}$. If another unilateral constraint is added at $\theta = \pi$, as in Figure 4.2b, there are two rigid configurations. At both $\theta = 0$ and $\theta = \pi$, the spring force causes a positive reaction.

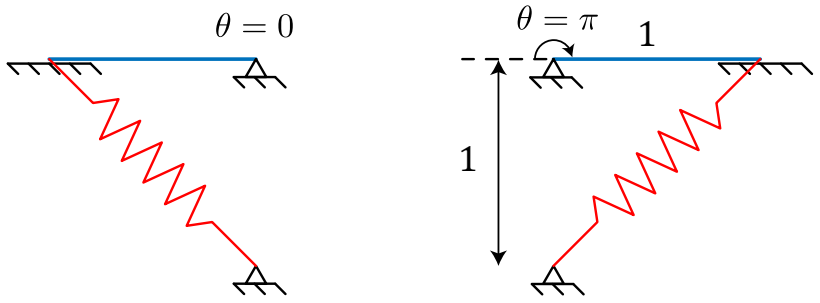

Figure 4.2: Two rigid configurations can be achieved, at $\theta = 0$ and $\theta = \pi$, due to unilateral constraints and a spring.

In the remainder of this chapter, the notion of rigidity due to unilateral constraints and an applied force is formulated for structures with multiple degrees of freedom. An analysis of critical perturbation forces is presented, leading to a systematic method for designing springs for multi-configuration rigidity.

4.3 Rigidity due to unilateral constraints and a force

In this section, conditions are developed for when a mechanism is rigid due to an applied force that engages a set of unilateral constraints. Linearized kinematics about a specific configuration of a discrete structure are used to derive conditions for infinitesimal rigidity, which is a sufficient condition for rigidity [71].

4.3.1 Kinematics

Consider a bar and hinge structure parameterized by vertex coordinates $\boldsymbol{x} \in \mathbb{R}^{dn}$, where n is the number of vertices and d is the number of spatial dimensions. The kinematics of the structure are defined by a set of bilateral constraints $\boldsymbol{h}(\boldsymbol{x})$ and unilateral constraints $\boldsymbol{g}(\boldsymbol{x})$:

$$h_i(\boldsymbol{x}) = 0 \quad i = 1, ..., n_b \tag{4.2}$$

$$g_j(\boldsymbol{x}) \leq 0 \quad j = 1, ..., n_u. \tag{4.3}$$

These formulations are presented in the context of general bilateral and unilateral constraints, which can model a variety of discrete structures. The bilateral constraints can represent, for example, pin-joint structures or plate-hinge structures. Appendix A formulates a kinematic model for plate-hinge structures as a set of bilateral constraints. The unilateral constraints can represent contact as well as tensegrity elements such as cables and no tension struts. In the context of the simple example of Figure 4.1, $\boldsymbol{x} = [x,\ y]^T$ contains the coordinates of the tip of the bar, the bilateral constraint is $h(\boldsymbol{x}) = \sqrt{x^2 + y^2} - 1 = 0$, and the unilateral constraint is $g(\boldsymbol{x}) = -y \leq 0$.

Linearization of the constraints about a configuration $\boldsymbol{x}_t$ yields

$$h_i(\boldsymbol{x}_t + \boldsymbol{d}) \approx h_i(\boldsymbol{x}_t) + \frac{\partial h_i(\boldsymbol{x})}{\partial \boldsymbol{x}}^T \Bigg|_{\boldsymbol{x}_t} \boldsymbol{d} = 0, \quad i = 1, ..., n_b \tag{4.4}$$

$$g_j(\boldsymbol{x}_t + \boldsymbol{d}) \approx g_j(x_t) + \frac{\partial g_j(\boldsymbol{x})}{\partial \boldsymbol{x}}^T \Bigg|_{\boldsymbol{x}_t} \boldsymbol{d} \leq 0, \quad j = 1, ..., n_u, \tag{4.5}$$

where $\boldsymbol{d} \in \mathbb{R}^{dn}$ is a displacement of the vertices about configuration $\boldsymbol{x}_t$. The gradients of the bilateral constraints $\boldsymbol{C}^b \in \mathbb{R}^{dn \times n_b}$ and unilateral constraints $\boldsymbol{C}^u \in \mathbb{R}^{dn \times n_a}$ give

the compatibility matrices of the constraints, defined as

$$C^b_{ik} = \left.\frac{\partial h_i(x)}{\partial x_k}\right|_{\boldsymbol{x}_t} \tag{4.6}$$

$$C^u_{jk} = \left.\frac{\partial g_j(x)}{\partial x_k}\right|_{\boldsymbol{x}_t}, \quad j \in I^a. \tag{4.7}$$

Here, the unilateral constraint gradients $\boldsymbol{C}^u$ are defined only for the *active unilateral constraints*, which belong to the set

$$I^a = \{j \mid g_j(\boldsymbol{x}_t) = 0\}, \tag{4.8}$$

where the set I^a indexes the n_a active constraints. Constraints that are not active in the configuration $\boldsymbol{x}_t$ do not need to be considered.

Assuming that configuration $\boldsymbol{x}_t$ satisfies the constraints, the linearized constraints of Eqs. (4.4) and (4.5) become

$$\boldsymbol{C}^b\boldsymbol{d} = \boldsymbol{\delta h} = \boldsymbol{0} \tag{4.9}$$

$$\boldsymbol{C}^u\boldsymbol{d} = \boldsymbol{\delta g} \leq \boldsymbol{0}. \tag{4.10}$$

The first-order changes in the bilateral and active unilateral constraints due to displacement $\boldsymbol{d}$ are $\boldsymbol{\delta h} \in \mathbb{R}^{n_b}$ and $\boldsymbol{\delta g} \in \mathbb{R}^{n_a}$, respectively.

Following Eq. (4.9), a first-order compatible displacement must be within the null space of $\boldsymbol{C}^b$. Defining $\boldsymbol{W}_m \in \mathbb{R}^{dn\times m}$ as an orthonormal basis of the m-dimensional null space of $\boldsymbol{C}^b$, a first-order compatible displacement $\boldsymbol{d}_m$ takes the form

$$\boldsymbol{d}_m = \boldsymbol{W}_m\boldsymbol{\alpha}, \tag{4.11}$$

where $\boldsymbol{\alpha}$ contains displacement coordinates with respect to the *mechanisms*, or the columns of $\boldsymbol{W}_m$. A kinematically indeterminate structure has $m > 0$ or, equivalently, there exist first-order compatible displacements. The quantity m defines the number of degrees of freedom of the structure.

4.3.2 Equilibrium

Consider a force $\boldsymbol{f} \in \mathbb{R}^{dn}$ applied to the vertices of the structure. This section derives conditions for equilibrium, corresponding to when the reaction forces in the bilateral and unilateral constraints balance the applied force. The generalized reaction forces associated with the bilateral and active unilateral constraints are denoted $\boldsymbol{\lambda} \in \mathbb{R}^{n_b}$ and $\boldsymbol{\mu} \in \mathbb{R}^{n_a}$. The unilateral constraint reactions must satisfy the conditions

$$\mu_i \geq 0, \quad i = 1, ..., n_a \tag{4.12}$$

$$\mu_i g_i = 0, \quad i = 1, ..., n_a. \tag{4.13}$$

In Equation (4.12), a sign convention is adopted where the unilateral reaction forces must be non-negative. For example, if the unilateral constraint represents contact, only compressive forces can be supported, so a positive reaction μ corresponds to a compressive contact force. If the unilateral constraint represents a cable, only tensile forces can be supported, so a positive reaction μ corresponds to a tensile cable force. Equation (4.13) represents the *complementary slackness* condition, which states that the unilateral reaction can only be nonzero if the constraint is active. For example, a contact force can only be nonzero if there is contact.

To derive the equations of equilibrium, the principle of virtual work is applied. The external work corresponding to the applied force $\boldsymbol{f}$ through displacement $\boldsymbol{d}$ is $\boldsymbol{f}^T\boldsymbol{d}$. The internal work associated with the constraints is $\boldsymbol{\lambda}^T\boldsymbol{\delta h} + \boldsymbol{\mu}^T\boldsymbol{\delta g}$. Equating the internal and external work,

$$\boldsymbol{f}^T\boldsymbol{d} = \boldsymbol{\lambda}^T\boldsymbol{\delta h} + \boldsymbol{\mu}^T\boldsymbol{\delta g}. \tag{4.14}$$

In the virtual work equation, the kinematic variables $\boldsymbol{d}$, $\boldsymbol{\delta h}$, and $\boldsymbol{\delta g}$ must be compatible, and we can substitute $\boldsymbol{d} = \boldsymbol{W}_m\boldsymbol{\alpha}$, $\boldsymbol{\delta h} = \boldsymbol{0}$, and $\boldsymbol{\delta g} = \boldsymbol{C}^u\boldsymbol{W}_m\boldsymbol{\alpha}$ to obtain

$$\boldsymbol{f}^T\boldsymbol{W}_m\boldsymbol{\alpha} = \boldsymbol{\mu}^T\boldsymbol{C}^u\boldsymbol{W}_m\boldsymbol{\alpha}. \tag{4.15}$$

Finally, this must generally hold for an arbitrary nonzero $\boldsymbol{\alpha}$. This leads to a set of m equilibrium equations

$$\boldsymbol{W}_m^T\boldsymbol{f} = \boldsymbol{W}_m^T\boldsymbol{C}^{uT}\boldsymbol{\mu} \tag{4.16}$$

that correspond to equilibrium in the direction of the mechanisms of the skeleton structure. The bilateral constraint reactions have been eliminated from the problem and the resulting equation requires that applied force $\boldsymbol{f}$ balances the unilateral constraint reactions in the direction of each mechanism. Equation (4.16) can be redefined in concise notation as

$$\hat{\boldsymbol{f}} = \boldsymbol{A}\boldsymbol{\mu} \tag{4.17}$$

where

$$\hat{\boldsymbol{f}} = \boldsymbol{W}_m^T\boldsymbol{f} \tag{4.18}$$

$$\boldsymbol{A} = \boldsymbol{W}_m^T\boldsymbol{C}^{uT}. \tag{4.19}$$

The matrix $\boldsymbol{A} \in \mathbb{R}^{m\times n_a}$ can be interpreted as a matrix that maps unilateral reaction forces to the mechanism directions. The vector $\hat{\boldsymbol{f}} \in \mathbb{R}^m$ represents the projection

of the applied force onto the mechanism directions. In the context of the simple example of Figure 4.2, $\hat{\boldsymbol{f}}$ contains only the y-component of the applied force, since the $\boldsymbol{W}_m = [0, 1]^T$.

Depending on the number of mechanisms and unilateral constraints, there are three cases regarding the equilibrium equation. The first is when $\boldsymbol{A}$ is square and invertible, which can occur when there are as many active unilateral constraints as mechanisms so $n_a = m$. This is the *statically determinate* case, where the unilateral reactions $\boldsymbol{\mu}$ are unique. The second case occurs when there are more active unilateral constraints than mechanisms $n_a > m$. This is the *statically indeterminate* case; a solution may exist, but the unilateral reactions are not unique. Finally, if $n_a < m$, rigidity cannot be achieved because there are not enough unilateral constraints to block all mechanism directions. The remainder of this chapter focuses on the statically determinate case while Chapter 5 develops the statically indeterminate case.

4.3.3 Conditions for rigidity: statically determinate case

For the case of statically determinate unilateral constraints, Theorem 4.1 states conditions for when a configuration is rigid. Since these conditions are developed based on linearization about a specific configuration, they represent conditions for *infinitesimal rigidity*, which are sufficient conditions for rigidity.

Theorem 4.1. *A configuration is rigid due to unilateral constraints and an applied force if*

$$null\left(\begin{bmatrix}\boldsymbol{C}^b\\ \boldsymbol{C}^u\end{bmatrix}\right) = \emptyset \tag{4.20}$$

and

$$\boldsymbol{\mu} = \boldsymbol{A}^{-1}\hat{\boldsymbol{f}} > \boldsymbol{0}. \tag{4.21}$$

Proof. If Eq. (4.21) holds, then all unilateral constraints are *strongly active*, with nonzero reaction forces. From complementary slackness, Eq. (4.13), strongly active unilateral constraints must hold to the equality:

$$\mu_i > 0 \implies g_i(x) = 0. \tag{4.22}$$

The linearized strongly active unilateral constraints must also hold to the equality,

$$\boldsymbol{C}^u\boldsymbol{d} = \boldsymbol{0}. \tag{4.23}$$

A first-order compatible displacement must not only be within the null space of $\boldsymbol{C}^b$, but also be within the null space of $\boldsymbol{C}^u$ since all active unilateral constraints are strongly active,

$$\boldsymbol{d} \in null\left(\begin{bmatrix}\boldsymbol{C}^b\\ \boldsymbol{C}^u\end{bmatrix}\right). \tag{4.24}$$

Finally, if Eq. (4.20) holds, there are no first-order admissible displacements and the configuration is infinitesimally rigid, and therefore rigid. □

The rigidity conditions can be interpreted as a kinematic condition in Eq. (4.21) and a static condition in Eq. (4.20). The kinematic condition requires that there are enough unilateral constraints such that if they are all held to the equality, the structure is rigid. Then, the static condition ensures that the force is applied in a direction that causes positive reactions in all unilateral constraints, allowing them to be treated as bilateral constraints.

4.3.4 Geometric interpretation of the rigidity conditions

Equation (4.21) takes the form of a set of linear inequalities. A powerful geometric interpretation of the rigidity conditions comes from examining the structure of the linear inequalities. The system of linear inequalities of Eq. (4.21) can be interpreted as an intersection of half-spaces in $\mathbb{R}^m$ that pass through the origin, also known as a *convex polyhedral cone*. The m half-spaces that make up the cone are defined by the normal vectors $\boldsymbol{n}_i$, which are the rows of the matrix $\boldsymbol{A}^{-1}$:

$$\boldsymbol{A}^{-1} = \begin{bmatrix}\boldsymbol{n}_1^T\\ \vdots\\ \boldsymbol{n}_m^T\end{bmatrix}. \tag{4.25}$$

Equation (4.21) requires that the applied force projected onto the mechanisms $\hat{\boldsymbol{f}}$ must belong to the interior of this cone:

$$\hat{\boldsymbol{f}} \in \{\hat{\boldsymbol{f}} \mid \boldsymbol{n}_i^T \hat{\boldsymbol{f}} > \boldsymbol{0}, \quad i = 1, ..., m\}. \tag{4.26}$$

Figure 4.3a illustrates this geometric interpretation in the two-dimensional case, where $m = n_a = 2$. The shaded region represents the cone defined by the two normal vectors in $\mathbb{R}^2$. Any applied force whose projection belongs to the interior of the cone leads to positive unilateral constraint reactions, and thus rigidity. This geometric interpretation provides a useful tool for analyzing perturbation forces applied to a rigid configuration.

(a) (b)

Figure 4.3: Geometric interpretation of the rigidity conditions for the two-dimensional case. (a) The polyhedral cone in $\mathbb{R}^2$ defined by the intersection of two half-spaces with normal vectors $\boldsymbol{n}_1$ to $\boldsymbol{n}_2$. (b) Example of a projected force $\hat{\boldsymbol{f}}_0$ that lies within this cone, thus satisfying the rigidity conditions.

4.3.5 Critical perturbation forces

The rigidity conditions were developed in the context of requiring no admissible displacements. Alternatively, a rigid configuration can resist arbitrary perturbation forces without displacement, up to some critical magnitude. If a large enough perturbation force is applied, the reaction forces in the unilateral constraints are overcome and the configuration is no longer rigid. The critical perturbation forces at which rigidity is lost are of interest because they correspond to the load-bearing capacity of a rigid configuration.

Consider a force $\boldsymbol{f}_0$ that, when applied to the structure, satisfies the rigidity conditions. Now, consider a perturbation force of magnitude P in the direction of the unit vector $\boldsymbol{f}_p$ that is also applied to the structure. The net force is

$$\boldsymbol{f} = \boldsymbol{f}_0 + P\boldsymbol{f}_p. \tag{4.27}$$

The structure will remain rigid if the net force satisfies the rigidity conditions. The critical force P^* in direction $\boldsymbol{f}_p$ at which rigidity is lost is the solution to the linear program

$$\max P \quad \text{subject to} \quad \boldsymbol{A}^{-1}\boldsymbol{W}_m^T\left(\boldsymbol{f}_0 + P\boldsymbol{f}_p\right) \geq 0. \tag{4.28}$$

In the context of the geometric interpretation of the rigidity conditions, the critical perturbation force can be interpreted as the distance from the projected force $\hat{\boldsymbol{f}}_0 = \boldsymbol{W}_m^T\boldsymbol{f}_0$ to the boundary of the polyhedral cone along direction projected perturbation direction $\hat{\boldsymbol{f}}_p = \boldsymbol{W}_m^T\boldsymbol{f}_p$.

Finally, we note that this type of linear programming analysis resembles the classical literature on the limit loads for plastic collapse of frames [76], another class of discrete structure with unilateral constraints.

4.3.6 An exact lower bound on the critical perturbation force

Utilizing the geometric interpretation that the critical force is the distance from the applied force $\hat{\boldsymbol{f}}_0$ to the boundary of the polyhedral cone, a lower bound on critical forces can be computed. The distance from $\hat{\boldsymbol{f}}_0$ to the hyperplane with normal $\boldsymbol{n}_i$ can be computed through the dot product

$$P_i^* = \frac{\boldsymbol{n}_i^T}{||\boldsymbol{n}_i||}\hat{\boldsymbol{f}}_0, \quad i = 1, ..., n_a, \tag{4.29}$$

where P_i^* represents the critical force in direction $-\boldsymbol{n}_i$. The distance from $\hat{\boldsymbol{f}}_0$ to the closest boundary of the polyhedral cone is

$$P_{min}^* = \min\{P_1^*, ..., P_{n_a}^*\}. \tag{4.30}$$

Among all possible perturbation force directions, the smallest critical force is P_{min}^*, in the direction normal to the closest boundary of the cone. This provides a lower bound on the critical perturbation force magnitude,

$$P_{min}^* \leq P^*. \tag{4.31}$$

In other words, a perturbation force in any direction is guaranteed not to cause displacements if its magnitude is less than P_{min}^*. Figure 4.3b illustrates the lower bound on the critical perturbation force in a two-dimensional example, where the distance P_{min}^* from $\hat{\boldsymbol{f}}_0$ to the closest boundary is highlighted.

The lower bound for the critical force provides a powerful tool for assessing the load-bearing capacity of a structure. Particularly, it provides the basis for the design of structures in the following section, where the lower bound critical force is maximized.

4.4 Spring parameter design

In this section, the design problem of embedding springs and unilateral constraints throughout a structure to achieve multi-configuration rigidity in specified target configurations is posed. Building from the rigidity conditions derived in Section 4.3, we seek to design springs such that the spring forces satisfy the rigidity conditions in multiple configurations.

The process for designing structures with multiple rigid configurations has three steps. First, n_t target configurations of a skeleton structure with m degrees of freedom are chosen. Then, a set of linear elastic springs are placed throughout the

structure. Figure 4.4 shows an example of a five-bar linkage, which represents a skeleton structure, embedded with two extensional springs and five torsion springs. Each spring introduces two design variables, the stiffness and the rest length or angle. Finally, m active unilateral constraints are placed in each target configuration such that Eq. (4.20) is satisfied.

The focus of this section is on designing spring parameters given a skeleton structure with n_t target configurations and a set of unilateral constraints satisfying Eq. (4.20) in each target configuration. The spring parameters must be designed such that all unilateral constraint reactions are positive, satisfying Eq. (4.21), in each target configuration, which corresponds to multi-configuration rigidity. For this problem, we present a general method for designing spring parameters. Moreover, a solution can be computed that maximizes the lower bound critical force in all configurations, effectively maximizing the load-bearing capacity of all target configurations. The spring design problem is formulated as a linear programming problem, which can be efficiently solved with guarantees of optimality.

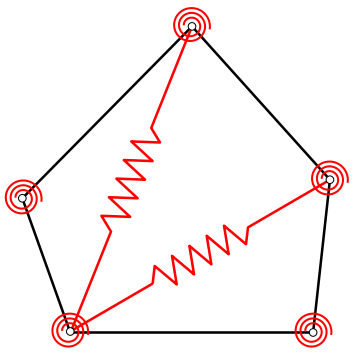

Figure 4.4: Example of a planar five-bar linkage with $p = 2$ extensional springs and $q = 5$ torsional springs.

4.4.1 Spring design problem setup

We pose a design problem to make n_t target configurations rigid by embedding linear extensional and torsion springs. The coordinates of each target configuration are $\boldsymbol{x}_j$ where $j = 1, ..., n_t$. In each target configuration, m active unilateral constraints have been placed, satisfying Eq. (4.20). A set of p linear extensional and q linear torsion springs are embedded throughout the structure. Extensional spring i has stiffness k_i and rest length l_i^0 while torsion spring k has angular stiffness κ_k and rest angle θ_k^0. Overall, there are $2(p + q)$ spring parameters, which make up the design variables that must be chosen to achieve multi-configuration rigidity. Extensional spring i has

current length l_i and torsion spring k has current angle θ_k. The forces $\boldsymbol{\sigma} \in \mathbb{R}^p$ in the extensional springs and moments $\boldsymbol{m} \in \mathbb{R}^q$ in the torsion springs are given by

$$\sigma_i = -\mathrm{k}_i(l_i - l_i^0) \tag{4.32}$$

$$m_k = -\kappa_k(\theta_k - \theta_k^0). \tag{4.33}$$

The rigidity conditions derived in the previous section are formulated in terms of an applied force on the vertices of the skeleton structure. The spring forces and moments must be mapped to their equivalent forces on the vertices. This mapping can be achieved using the equilibrium matrix of the springs. For consistency of notation, we first define the compatibility matrix of the springs $\boldsymbol{C}^s \in \mathbb{R}^{(p+q)\times dn}$, which contains the gradients of $\boldsymbol{l}$ and $\boldsymbol{\theta}$

$$\boldsymbol{C}^s = \begin{bmatrix} \dfrac{\partial \boldsymbol{l}}{\partial \boldsymbol{x}} \\ \dfrac{\partial \boldsymbol{\theta}}{\partial \boldsymbol{x}} \end{bmatrix}. \tag{4.34}$$

The transpose of the compatibility matrix yields the equilibrium matrix [77], which maps spring forces to forces on the vertices of the structure,

$$\boldsymbol{f} = \boldsymbol{C}^{sT} \begin{bmatrix} \boldsymbol{\sigma} \\ \boldsymbol{m} \end{bmatrix}. \tag{4.35}$$

Here, $\boldsymbol{f}$ is the force exerted on the skeleton structure by the springs, which now fits the framework of the rigidity conditions. Inserting Eq. (4.35) into Eq. (4.18), the projection of the spring forces onto the mechanisms is

$$\hat{\boldsymbol{f}} = \boldsymbol{W}_m^T \boldsymbol{C}^{sT} \begin{bmatrix} \boldsymbol{\sigma} \\ \boldsymbol{m} \end{bmatrix}. \tag{4.36}$$

The design problem at hand is to choose spring parameters such that the corresponding $\hat{\boldsymbol{f}}$ satisfies the rigidity conditions in multiple configurations.

To formulate the spring parameter design problem, we begin by listing a set of constraints. For rigidity in each configuration, positive unilateral reactions are required from Eq. (4.21), which must hold in all target configurations. Inserting Eq. (4.36) into (4.21) at each configuration, the conditions for rigidity in all target configurations can be written as:

$$\left(\boldsymbol{A}^{-1} \boldsymbol{W}_m^T \boldsymbol{C}^{sT} \begin{bmatrix} \boldsymbol{\sigma} \\ \boldsymbol{m} \end{bmatrix} \right)_j > \boldsymbol{0}, \quad t = 1, ..., n_j, \tag{4.37}$$

where $()_j$ denotes evaluation at configuration $\boldsymbol{x}_j$. For each target configuration, Eq. (4.37) contains m inequalities, leading to $n_t m$ total inequalities required for multi-configuration rigidity.

Along with the conditions for rigidity, bounds on the spring parameters are introduced to limit the design space to practical spring parameters. Solutions with negative stiffness or extremely large stiffness springs are not of interest. We restrict the spring stiffnesses to the range between 0 and some upper bound $\boldsymbol{k}_{max}$ and $\boldsymbol{\kappa}_{max}$. Similarly, the extensional spring rest lengths are bound by $\boldsymbol{l}^0_{min}$ and $\boldsymbol{l}^0_{max}$ and the torsion spring rest angles are bound by $\boldsymbol{\theta}^0_{min}$ and $\boldsymbol{\theta}^0_{max}$. The spring parameter constraints are written as:

$$\mathbf{0} \leq \begin{bmatrix} \mathbf{k} \\ \boldsymbol{\kappa} \end{bmatrix} \leq \begin{bmatrix} \mathbf{k}_{max} \\ \boldsymbol{\kappa}_{max} \end{bmatrix} \tag{4.38}$$

$$\begin{bmatrix} \boldsymbol{l}^0_{min} \\ \boldsymbol{\theta}^0_{min} \end{bmatrix} \leq \begin{bmatrix} \boldsymbol{l}^0 \\ \boldsymbol{\theta}^0 \end{bmatrix} \leq \begin{bmatrix} \boldsymbol{l}^0_{max} \\ \boldsymbol{\theta}^0_{max} \end{bmatrix}. \tag{4.39}$$

Therefore, we seek a set of spring parameters that collectively satisfy the multi-rigidity condition of Eq. (4.37), that is within the bounds of Eqs. (4.38) and (4.39).

4.4.2 The most rigid solution: Chebyshev center

There may be many sets of spring parameters within the bounds that satisfy the multi-configuration rigidity conditions. However, not all solutions lead to desirable and practical designs. If the lower bound on the critical force in a target configuration is small, that configuration can only support small loads in the direction corresponding to the lower bound. Thus, we seek a set of spring parameters that maximizes the lower bound on critical force in each target configuration.

Recalling Section 4.3.6, the minimum critical force in each configuration is the distance from the projected spring force $\hat{\boldsymbol{f}}$ to the nearest boundary of the polyhedral cone describing the rigidity conditions. Therefore, spring parameters are sought that maximize the distance to the nearest boundary. The distance from $\hat{\boldsymbol{f}}$ to boundary i of the polyhedral cone in configuration $\boldsymbol{x}_j$ can be computed in terms of the spring forces and moments by inserting Eq. (4.36) into Eq. (4.29), yielding

$$P_i^*|_j = \left(\frac{\boldsymbol{n}_i^T}{||\boldsymbol{n}_i||} \boldsymbol{W}_m^T \boldsymbol{C}^{sT} \begin{bmatrix} \boldsymbol{\sigma} \\ \boldsymbol{m} \end{bmatrix} \right)_j. \tag{4.40}$$

For springs satisfying the rigidity conditions, $P_i^*|_j$ is positive for all boundaries i and configurations j. A positive scalar r is introduced such that $P_i^*|_j \geq r$ for all i

and j. Now, an optimization problem can be formulated to maximize r, equivalently maximizing the smallest value of $P_i^*|_j$:

$$\begin{aligned} \max r \quad & \text{subject to} \\ & P_i^*|_j = \left(\frac{\boldsymbol{n}_i^T}{||\boldsymbol{n}_i||} \boldsymbol{W}_m^T \boldsymbol{C}^{sT} \begin{bmatrix} \boldsymbol{\sigma} \\ \boldsymbol{m} \end{bmatrix} \right)_j \geq r, \quad i = 1, ..., m, \quad j = 1, ..., n_t \\ & \mathbf{0} \leq \begin{bmatrix} \mathbf{k} \\ \boldsymbol{\kappa} \end{bmatrix} \leq \begin{bmatrix} \mathbf{k}_{max} \\ \boldsymbol{\kappa}_{max} \end{bmatrix} \\ & \begin{bmatrix} \boldsymbol{l}_{min}^0 \\ \boldsymbol{\theta}_{min}^0 \end{bmatrix} \leq \begin{bmatrix} \boldsymbol{l}^0 \\ \boldsymbol{\theta}^0 \end{bmatrix} \leq \begin{bmatrix} \boldsymbol{l}_{max}^0 \\ \boldsymbol{\theta}_{max}^0 \end{bmatrix}. \end{aligned} \tag{4.41}$$

This optimization problem is formulated in terms of the spring parameters $\mathbf{k}$, $\boldsymbol{\kappa}$, $\boldsymbol{l}^0$, $\boldsymbol{\theta}^0$, and r. The optimal solution corresponds to the spring design with the largest minimum critical force in all target configurations.

This solution is referred to as the *Chebyshev center*. The Chebyshev center solution represents the design that maximizes the lower bound on critical force, where this optimal lower bound corresponds to the Chebyshev radius. The corresponding spring parameters are denoted $\mathbf{k}_c$, $\boldsymbol{\kappa}_c$, $\boldsymbol{l}_c^0$, $\boldsymbol{\theta}_c^0$. This set of spring parameters represents the design that has the largest lower bound critical force $P_{min}^* = r_c$ while respecting the bounds on spring parameters. This gives a guarantee that any perturbation force smaller than r_c, applied in any direction to any target configuration will not cause any displacement of the structure.

The Chebyshev center, which is defined generally in [78], represents the center of the largest sphere inscribed in a set and the Chebyshev radius r_c is the radius of this sphere. Equivalently, it corresponds to the point furthest from the boundary of a set, where the distance from this point to the closest boundary is r_c. The Chebyshev center is not necessarily unique, but the Chebyshev radius is. For example, a rectangle does not have a unique center for its largest inscribed circle, but the corresponding radius is unique. For further discussion of uniqueness, see [79]. A variety of fields have found use for Chebyshev centers; it appears in robust controller design [80, 81], classification problems [82], state estimation for dynamic systems [83], and machine learning [84].

As written in Eqs. (4.41), the optimization problem to compute the Chebyshev center is parameterized by the spring parameters $\mathbf{k}$, $\boldsymbol{l}^0$, $\boldsymbol{\kappa}$, and $\boldsymbol{\theta}^0$, noting that $\boldsymbol{\sigma}$ and $\boldsymbol{m}$ are functions of the spring parameters from Eqs. (4.32) and (4.33). In this

parameterization the optimization problem is nonlinear since the rigidity constraints contain the product $\mathrm{k}_i l_i^0$ from Eq. (4.32) and $\kappa_j \theta_j^0$ from Eq. (4.33). However, with a change of variables, all constraints can be written as linear inequalities so that the Chebyshev center computation becomes a linear program.

4.4.3 Linear programming formulation

With a change of variables, the rigidity constraints can be formulated as linear inequalities. To avoid the nonlinearity introduced by the product of stiffness and rest length/angle, a change of variables is introduced as

$$\begin{aligned} \sigma_i^0 &\equiv \mathrm{k}_i l_i^0 \\ m_j^0 &\equiv \kappa_j \theta_j^0, \end{aligned} \tag{4.42}$$

where $\boldsymbol{\sigma}^0 \in \mathbb{R}^p$ corresponds to the extensional spring force at zero length and $\boldsymbol{m}^0 \in \mathbb{R}^q$ corresponds to the torsion spring moment at zero angle. In this parameterization, the spring forces take the form

$$\begin{aligned} \sigma_i &= -\mathrm{k}_i l_i + \sigma_i^0 \\ m_j &= -\kappa_j \theta_j + m_j^0. \end{aligned} \tag{4.43}$$

Equivalently in matrix form,

$$\begin{aligned} \boldsymbol{\sigma} &= \boldsymbol{M}_1 \begin{bmatrix} \mathbf{k} \\ \boldsymbol{\sigma}^0 \end{bmatrix} \\ \boldsymbol{m} &= \boldsymbol{M}_2 \begin{bmatrix} \boldsymbol{\kappa} \\ \boldsymbol{m}^0 \end{bmatrix} \end{aligned} \tag{4.44}$$

where the matrices $\boldsymbol{M}_1 \in \mathbb{R}^{p \times 2p}$ and $\boldsymbol{M}_2 \in \mathbb{R}^{q \times 2q}$ are defined as

$$\begin{aligned} \boldsymbol{M}_1 &= \left[\begin{array}{c|c} \mathrm{diag}(\boldsymbol{l}) & -\boldsymbol{I}_p \end{array} \right] \\ \boldsymbol{M}_2 &= \left[\begin{array}{c|c} \mathrm{diag}(\boldsymbol{\theta}) & -\boldsymbol{I}_q \end{array} \right]. \end{aligned} \tag{4.45}$$

The $p \times p$ and $q \times q$ identity matrices are denoted $\boldsymbol{I}_p$ and $\boldsymbol{I}_q$. The operator diag() maps a vector to a matrix with the vector along its diagonal. Inserting Eq. (4.44) into the multi-configuration rigidity conditions of Eq. (4.37), we obtain

$$\left(\boldsymbol{A}^{-1} \boldsymbol{W}_m^T \boldsymbol{C}^{sT} \begin{bmatrix} \boldsymbol{M}_1 & \mathbf{0} \\ \mathbf{0} & \boldsymbol{M}_2 \end{bmatrix} \begin{bmatrix} \mathbf{k} \\ \boldsymbol{\sigma}^0 \\ \boldsymbol{\kappa} \\ \boldsymbol{m}^0 \end{bmatrix} \right)_j > \mathbf{0}, \quad j = 1, \ldots, n_t, \tag{4.46}$$

which is a set of mn_t linear inequalities with respect to $\mathbf{k}$, $\boldsymbol{\sigma}^0$, $\boldsymbol{\kappa}$, and $\boldsymbol{m}^0$.

In addition to the rigidity conditions, the bounds on spring parameters must be formulated in this new parameterization. The bounds on stiffness in Eq. (4.38) can be enforced directly. However, Eq. (4.39) must be reformulated in terms of $\boldsymbol{\sigma}^0$ and $\boldsymbol{m}^0$. Multiplying by the stiffness of each spring,

$$\begin{aligned} \mathrm{k}_i l^0_{min,i} \leq \mathrm{k}_i l^0_i \leq \mathrm{k}_i l^0_{max,i}, \quad & i = 1, ..., p \\ \kappa_i \theta^0_{min,i} \leq \kappa_i \theta^0_i \leq \kappa_i \theta^0_{max,i}, \quad & i = 1, ..., q, \end{aligned} \tag{4.47}$$

which is valid since all stiffness variables are non-negative. Now, the bounds on rest lengths and angles can be written as linear inequalities on $\mathbf{k}$, $\boldsymbol{\sigma}^0$, $\boldsymbol{\kappa}$, and $\boldsymbol{m}^0$ as

$$\begin{bmatrix} \boldsymbol{M}_3 & \mathbf{0} \\ \mathbf{0} & \boldsymbol{M}_4 \end{bmatrix} \begin{bmatrix} \mathbf{k} \\ \boldsymbol{\sigma}^0 \\ \boldsymbol{\kappa} \\ \boldsymbol{m}^0 \end{bmatrix} \leq \mathbf{0} \tag{4.48}$$

where the matrices $\boldsymbol{M}_3 \in \mathbb{R}^{2p \times 2p}$ and $\boldsymbol{M}_4 \in \mathbb{R}^{2q \times 2q}$ are defined as

$$\begin{aligned} \boldsymbol{M}_3 &= \left[\begin{array}{c|c} \mathrm{diag}(\boldsymbol{l}_{min}) & -\boldsymbol{I}_p \\ \hline \mathrm{diag}(-\boldsymbol{l}_{max}) & \boldsymbol{I}_p \end{array}\right] \\ \boldsymbol{M}_4 &= \left[\begin{array}{c|c} \mathrm{diag}(\boldsymbol{\theta}_{min}) & -\boldsymbol{I}_q \\ \hline \mathrm{diag}(-\boldsymbol{\theta}_{max}) & \boldsymbol{I}_q \end{array}\right]. \end{aligned} \tag{4.49}$$

In summary, the constraints that define the multi-configuration rigidity design problem, Eqs. (4.37), (4.38), and (4.39), can be rewritten as linear inequalities with respect to $\mathbf{k}$, $\boldsymbol{\sigma}^0$, $\boldsymbol{\kappa}$, and $\boldsymbol{m}^0$. These linear inequalities are given by Eqs. (4.46), (4.38), (4.48).

Finally, the computation of the Chebyshev center can be reformulated as a linear program, taking the form:

$$\max r \quad \text{subject to}$$

$$P_i^*|_j = \left(\frac{\boldsymbol{n}_i^T}{||\boldsymbol{n}_i||} \boldsymbol{W}_m^T \boldsymbol{C}^{sT} \begin{bmatrix} \boldsymbol{M}_1 & \boldsymbol{0} \\ \boldsymbol{0} & \boldsymbol{M}_2 \end{bmatrix} \right)_j \begin{bmatrix} \mathbf{k} \\ \boldsymbol{\sigma}^0 \\ \boldsymbol{\kappa} \\ \boldsymbol{m}^0 \end{bmatrix} \geq r, \quad i = 1, ..., m, \quad j = 1, ..., n_t$$

$$\boldsymbol{0} \leq \begin{bmatrix} \mathbf{k} \\ \boldsymbol{\kappa} \end{bmatrix} \leq \begin{bmatrix} \mathbf{k}_{max} \\ \boldsymbol{\kappa}_{max} \end{bmatrix}$$

$$\begin{bmatrix} \boldsymbol{M}_3 & \boldsymbol{0} \\ \boldsymbol{0} & \boldsymbol{M}_4 \end{bmatrix} \begin{bmatrix} \mathbf{k} \\ \boldsymbol{\sigma}^0 \\ \boldsymbol{\kappa} \\ \boldsymbol{m}^0 \end{bmatrix} \leq \boldsymbol{0}. \tag{4.50}$$

There are a total of $mn_t + 4p + 4q$ inequality constraints in the linear program, which optimizes over the $2p + 2q + 1$ unknowns $\mathbf{k}$, $\boldsymbol{\sigma}^0$, $\boldsymbol{\kappa}$, $\boldsymbol{m}^0$, and r. Since linear programs can be solved efficiently with optimality guarantees, the Chebyshev center can be easily computed and is guaranteed to be the globally optimal solution. Additionally, if this linear program is infeasible, then there are no spring parameters in the given bounds that satisfy rigidity in all configurations.

Finally, upon computing the solution, the rest lengths and angles can be retrieved from $\boldsymbol{\sigma}_c^0$ and $\boldsymbol{m}_c^0$ as

$$l_{ci}^0 = \frac{\sigma_{ci}^0}{\mathrm{k}_{ci}}, \quad \theta_{cj}^0 = \frac{m_{cj}^0}{\kappa_{cj}}. \tag{4.51}$$

If a spring has zero stiffness, the rest length or angle is not defined and there is effectively no spring in this case.

4.4.4 Energetic interpretation

Multi-configuration rigidity has so far been formulated without any notion of energy. However, a useful interpretation comes from considering the energy in the springs. Specifically, in a configuration satisfying the rigidity conditions, the energy has a positive slope in all kinematically admissible directions. Thus, a rigid configuration corresponds to a sharp local energy minimum on the boundary of kinematically admissible configurations.

The energy stored in the extensional and torsion springs is given by

$$E(\boldsymbol{x}) = \sum_{i=1}^{p} \frac{1}{2} \mathrm{k}_i (l_i(\boldsymbol{x}) - l_i^0)^2 + \sum_{i=1}^{q} \frac{1}{2} \kappa_i (\theta_i(\boldsymbol{x}) - \theta_i^0)^2. \tag{4.52}$$

The slope of the energy along a mechanism direction $\boldsymbol{d}_m = \boldsymbol{W}_m \boldsymbol{\alpha}$

$$\frac{\partial E}{\partial \boldsymbol{x}}^T \boldsymbol{d}_m = \left(\frac{\partial E}{\partial \boldsymbol{l}} \frac{\partial \boldsymbol{l}}{\partial \boldsymbol{x}} \right)^T \boldsymbol{W}_m \boldsymbol{\alpha} + \left(\frac{\partial E}{\partial \boldsymbol{\theta}} \frac{\partial \boldsymbol{\theta}}{\partial \boldsymbol{x}} \right)^T \boldsymbol{W}_m \boldsymbol{\alpha}. \tag{4.53}$$

The spring forces and moments are related to the energy by $\partial E / \partial \boldsymbol{l} = -\boldsymbol{\sigma}$ and $\partial E / \partial \boldsymbol{\theta} = -\boldsymbol{m}$. In terms of the spring forces and moments along with the compatibility matrix of the springs from Eq. (4.34), we obtain

$$\begin{aligned} \frac{\partial E}{\partial \boldsymbol{x}}^T \boldsymbol{d}_m &= - \begin{bmatrix} \boldsymbol{\sigma} \\ \boldsymbol{m} \end{bmatrix}^T \boldsymbol{C}^s \boldsymbol{W}_m \boldsymbol{\alpha} \\ &= -\boldsymbol{f}^T \boldsymbol{W}_m \boldsymbol{\alpha}, \end{aligned} \tag{4.54}$$

where $\boldsymbol{f}$ contains the nodal forces applied by the springs from Eq. (4.35). Substituting in the equilibrium equation, Eq. (4.16),

$$\frac{\partial E}{\partial \boldsymbol{x}}^T \boldsymbol{d}_m = -\boldsymbol{\mu}^T \boldsymbol{C}^u \boldsymbol{W}_m \boldsymbol{\alpha}. \tag{4.55}$$

Rewriting as a sum over the active unilateral constraints gives

$$\frac{\partial E}{\partial \boldsymbol{x}}^T \boldsymbol{d}_m = - \sum_{i=1}^{n_a} \mu_i \left(\boldsymbol{C}^u \boldsymbol{W}_m \boldsymbol{\alpha} \right)_i . \tag{4.56}$$

The rigidity condition of Eq. (4.21) requires that all reactions $\mu_i > 0$. Recalling the linearized unilateral constraints of Eq. (4.10), the vector $\boldsymbol{\delta g} = \boldsymbol{C}^u \boldsymbol{W}_m \boldsymbol{\alpha}$ must have non-positive components. This leaves two possible cases. If $\boldsymbol{\delta g}$ has at least one nonzero component, then the directional derivative of the energy is positive in all admissible directions. Alternatively, if all components of $\boldsymbol{\delta g}$ are zero, the directional derivative of the energy is zero. The latter case is prohibited by the condition of Eq. (4.20), which is equivalently written as $null(\boldsymbol{C}^u \boldsymbol{W}_m) = \emptyset$. Therefore, $\boldsymbol{C}^u \boldsymbol{W}_m \boldsymbol{\alpha}$ must have at least one negative entry for any nonzero $\boldsymbol{\alpha}$. Finally, we conclude that

$$\frac{\partial E}{\partial \boldsymbol{x}}^T \boldsymbol{d} > 0 \quad \forall \boldsymbol{d} \in \{ \boldsymbol{d} \mid \boldsymbol{C}^b \boldsymbol{d} = \boldsymbol{0},\ \boldsymbol{C}^u \boldsymbol{d} \leq \boldsymbol{0},\ \boldsymbol{d} \neq \boldsymbol{0} \}. \tag{4.57}$$

Therefore, at a rigid configuration, the slope of the energy of the springs is positive in all kinematically admissible directions.

From the energetic perspective, multi-configuration rigidity corresponds to having multiple local energy minima, where each energy minima exhibits property of Eq. (4.57). That is, each local minimum is a sharp minimum with the energy sloping into the boundary in all kinematically admissible directions. To draw comparison to multi-stability, multi-stable structures have smooth energy minima at multiple configurations. The key difference between the two concepts is that the slope of the energy is nonzero in rigid configurations and zero in stable configurations.

4.5 2-DOF linkage example

To demonstrate multi-configuration rigidity, an example is presented of the design of a linkage. Unilateral constraints and springs are embedded to achieve rigidity in four target configurations.

4.5.1 Problem setup

In this example, the skeleton structure is a linkage comprised of four pin-jointed bars. Both ends of the linkage are pinned and the resulting linkage has $m = 2$ degrees of freedom. The aim of this example is to embed springs and unilateral constraints to achieve rigidity in the four target configurations shown in Figure 4.5. Unilateral constraints are introduced in the form of angle stops on hinges 1 and 5, restricting the range of these hinges to between 0 and $\pi/4$. The angle stops are represented by the black brackets around θ_1 and θ_5 in Figure 4.5. Finally, linear torsion springs are placed on each hinge. This introduces 10 design variables corresponding to the stiffness $\boldsymbol{\kappa} \in \mathbb{R}^5$ and rest angle $\boldsymbol{\theta}^0 \in \mathbb{R}^5$ of each spring. The design problem at hand is to select the 10 spring parameters such that each target configuration is rigid.

We present this example with realistic units, which both accommodates intuitive understanding of the problem and corresponds to the prototype presented in Chapter 6. The bar lengths are $L_1 = L_4 = 75$ mm and $L_2 = L_3 = 94.75$ mm, while the ends of the linkage are $L_5 = 238.65$ mm apart. The hinge angles in the four target configurations are listed in Table 4.1.

Table 4.1: Target configuration hinge angles (in radians)

Configuration	1	2	3	4
θ_1	$\pi/4$	0	$\pi/4$	0
θ_2	$\pi/2$	2.063	1.052	2.731
θ_3	$\pi/2$	0.985	1.426	1.426
θ_4	$\pi/2$	2.063	2.731	1.052
θ_5	$\pi/4$	0	0	$\pi/4$

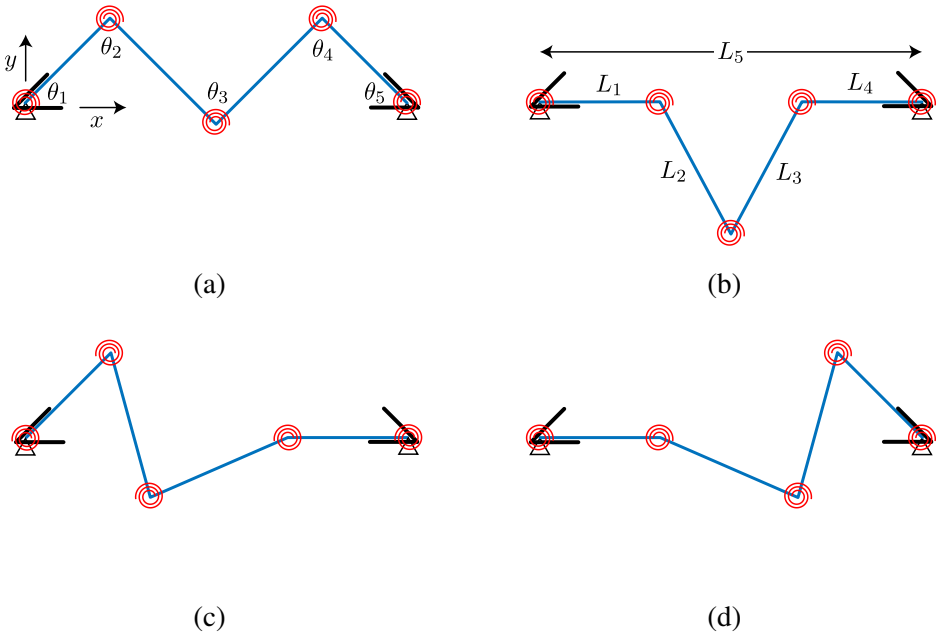

Figure 4.5: Two-DOF linkage geometry. The red coils at each hinge represent linear torsion springs and the brackets on hinges 1 and 5 represent unilateral constraints on the fold angle. (a) Target configuration 1. (b) Target configuration 2. (c) Target configuration 3. (d) Target configuration 4.

Since hinges 1 and 5 are pinned, the structure can be parameterized by the coordinates of the free vertices at hinges 2, 3, and 4, $\boldsymbol{x} = [x_2, y_2, x_3, y_3, x_4, y_4]^T$. The lengths of the four bars are $\boldsymbol{L}(\boldsymbol{x}) : \mathbb{R}^6 \to \mathbb{R}^4$. The kinematics of the linkage can be captured by a set of bilateral constraints $\boldsymbol{h}(\boldsymbol{x})$ fixing the lengths (in mm) as

$$\boldsymbol{h}(\boldsymbol{x}) = \boldsymbol{L}(\boldsymbol{x}) - \begin{bmatrix} 75 \\ 94.75 \\ 94.75 \\ 75 \end{bmatrix} = \boldsymbol{0}. \tag{4.58}$$

The unilateral constraints corresponding to the angle stops on hinges 1 and 5 take the form

$$\boldsymbol{g}(\boldsymbol{x}) = \begin{bmatrix} \theta_1(\boldsymbol{x}) \\ -\theta_1(\boldsymbol{x}) \\ \theta_5(\boldsymbol{x}) \\ -\theta_5(\boldsymbol{x}) \end{bmatrix} - \begin{bmatrix} \pi/4 \\ 0 \\ \pi/4 \\ 0 \end{bmatrix} \leq \boldsymbol{0}. \tag{4.59}$$

Of the $n_u = 4$ unilateral constraints, in each target configuration $n_a = 2$ unilateral constraints are active, leading to static determinacy among the unilateral constraint

reaction moments since $n_a = m$. Linearization of the constraints to compute the constraint compatibility matrices $\boldsymbol{C}^u$, $\boldsymbol{C}^b$, as well as the other relevant matrices in each configuration, is outlined in Appendix C. Upon computation of $\boldsymbol{C}^u$ and $\boldsymbol{C}^b$ in each configuration, it can be verified that Eq. (4.20) is satisfied in each configuration. Therefore, if the spring parameters admit positive unilateral reactions in each target configuration, all four target configurations are rigid.

The moments in the $q = 5$ torsion springs are $m_i = -\kappa_i(\theta_i - \theta_i^0)$ for $i = 1, ..., 5$. The compatibility matrix of the springs $\boldsymbol{C}^s$ is also computed in Appendix C, which maps the spring moments to their equivalent nodal forcing on the skeleton structure through Eq. (4.35). Bounds are introduced on the spring parameters to reduce the design space to practical designs that are physically achievable. For this example, all components of $\boldsymbol{\theta}^0_{min}$ are taken as $-\pi$ and all components of $\boldsymbol{\theta}^0_{max}$ are taken as π. Each torsion spring is restricted by the same upper bound on stiffness, κ_{max}, which is left unspecified and acts as a scaling factor for the critical force solution.

4.5.2 The Chebyshev center solution

In this example, there are many solutions that satisfy multi-configuration rigidity and the spring parameter bounds of Eqs. (4.37)-(4.39). Of particular interest, however, is the solution that maximizes the smallest critical perturbation force, which is the Chebyshev center solution formulated in Section 4.4.2. The Chebyshev center can be computed by solving the following linear program:

$$
\begin{aligned}
&\max r \quad \text{subject to} \\
&P_i^*|_j = \left(\frac{\boldsymbol{n}_i^T}{||\boldsymbol{n}_i||} \boldsymbol{W}_m^T \boldsymbol{C}^{sT} \boldsymbol{M}_2 \right)_j \begin{bmatrix} \boldsymbol{\kappa} \\ \boldsymbol{m}^0 \end{bmatrix} \geq r, \quad i = 1, 2, \quad j = 1, 2, 3, 4 \\
&\mathbf{0} \leq \boldsymbol{\kappa} \leq \boldsymbol{\kappa}_{max} \\
&\boldsymbol{M}_4 \begin{bmatrix} \boldsymbol{\kappa} \\ \boldsymbol{m}^0 \end{bmatrix} \leq \mathbf{0}.
\end{aligned}
\tag{4.60}
$$

This linear program follows from Eq. (4.50) for the specific problem at hand, which has only torsional springs, four target configurations, and $m = n_a = 2$. The matrices required to formulate the constraints are given in Appendix C. Solving the linear program yields the Chebyshev center spring parameters $\boldsymbol{\kappa}_c$ and $\boldsymbol{m}_c^0$ along with the Chebyshev radius r_c. The spring parameters $\boldsymbol{\kappa}_c$ and $\boldsymbol{\theta}_c^0$ corresponding to the

Chebyshev center, with the rest angles computed from Eq. (4.51), are

$$\boldsymbol{\kappa}_c = \begin{bmatrix} 0 \\ 0.79 \\ 1 \\ 0.79 \\ 0 \end{bmatrix} \kappa_{max}, \qquad \begin{bmatrix} \theta^0_{2c} \\ \theta^0_{3c} \\ \theta^0_{4c} \end{bmatrix} = \begin{bmatrix} \pi \\ \pi \\ \pi \end{bmatrix}, \tag{4.61}$$

where θ^0_c is in radians and the stiffness scales linearly with κ_{max}. Since κ_1 and κ_5 are zero, there are effectively no springs on hinges 1 and 5, so the rest angles are not defined.

The corresponding Chebyshev radius, which is also output from the linear program, is $r_c = 7.78\kappa_{max}$, where r_c has units of Newtons if κ_{max} is specified in Nm/rad. As a benchmark, the prototype of the linkage presented in Chapter 6 uses spring with nominal stiffness of 0.230 Nm/rad; if this value is taken as κ_{max}, the resulting Chebyshev radius is 1.79 N. However, the maximum stiffness of the springs can be scaled to achieve a larger Chebyshev radius and therefore a larger load-bearing capacity.

The Chebyshev radius brings the guarantee that applying a load to any of the four target configurations in any direction will not cause displacements so long as its magnitude is less than r_c. However, most loading directions can support larger loads than the Chebyshev radius since it provides a lower bound. Since the Chebyshev center is computed by solving a linear program, its optimality is guaranteed. There is no set of spring parameters that leads to a larger value than r_c. A larger value could potentially be achieved by increasing the bounds on spring parameters, introducing new springs, or considering different unilateral constraints.

The geometric interpretation of the rigidity conditions presented in Section 4.3.4 is useful in understanding the Chebyshev center solution. For each target configuration, Figure 4.6 plots the polyhedral cone of projected forces that satisfies the rigidity condition, which is shaded blue. For example, the shaded region of 4.6a is the intersection of half-planes defined by the normal vectors $\boldsymbol{n}_1|_1 = [-95.7107,\ 45.7107]^T$ and $\boldsymbol{n}_2|_1 = [45.7107,\ 95.7107]^T$, which are computed in Appendix C. Each plot is in the space of the mechanism directions evaluated in each respective target configuration. That is, $\hat{f}_1|_1$ is the component of the force in the direction of the first column of $\boldsymbol{W}_m|_1$.

Figure 4.6 also plots for each configuration the projection of the spring force of the Chebyshev center spring parameters, $\hat{\boldsymbol{f}}_c$. This is computed by first computing spring moments $\boldsymbol{m}_c$ corresponding to the Chebyshev center spring parameters using Eq. (4.32), then projecting onto the mechanisms using Eq. (4.36).

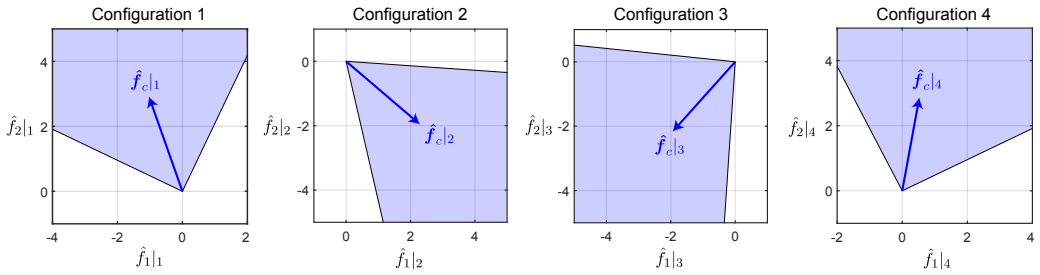

(a) (b) (c) (d)

Figure 4.6: In each target configuration, the shaded region is the polyhedral cone defining the rigidity condition of Eq. (4.21). The projected spring force of the Chebyshev center solution $\hat{\boldsymbol{f}}_c$ is the solution that maximizes the distance to the boundary of the cone in all configurations, while respecting the spring parameter bounds. The units of all four plots are Newtons.

The Chebyshev center is the solution that maximizes the distance from $\hat{\boldsymbol{f}}_c$ to the boundaries of the cone in all target configurations, while respecting the spring parameter bounds. The spring parameter bounds impose restrictions on the magnitude of $\hat{\boldsymbol{f}}_c$ in each configuration (otherwise the linear program would be unbounded). The Chebyshev center solution $\hat{\boldsymbol{f}}_c$ is close to bisecting the boundaries of the cone in each configuration, which results from maximizing distance to the closest boundary. In each configuration, we can compute the distance to the closest boundary P^*_{min} of the cone, from Eq. (4.30). In configurations 2, 3, and 4, the distance to the closest boundary is $P^*_{min}|_2 = P^*_{min}|_3 = P^*_{min}|_4 = 7.78\kappa_{max}$. Again, if κ_{max} is specified in Nm/rad the critical forces take units N. In configuration 1, $P^*_{min}|_1 = 9.52\kappa_{max}$, which is larger than for the other configurations. Recall that the Chebyshev center formulation requires the spring force is at least r_c from each boundary, but the distance to a boundary can be farther, which is the case for configuration 1.

4.5.3 Perturbation force analysis

To gain a deeper understanding of multi-configuration rigidity and the Chebyshev center solution, critical forces are computed for various loading cases applied to target configuration 2. A similar analysis could be carried out for each of the four rigid configurations. Critical perturbation loads in the unit direction $\boldsymbol{f}_p$ can be

directly computed through the linear program of Eq. (4.28). Additionally, the geometric interpretation of critical forces is discussed to build intuition. We present three perturbation load cases to highlight the structure of the rigidity conditions.

The first perturbation direction we consider is $\boldsymbol{f}_{p1} = [0, 0, 1, 0, 0, 0]^T$, which corresponds to the $+x$ direction of vertex 3 as shown in Figure 4.7a. Directly from the linear programming computation, the critical force in this direction is $P^* = 12.17\kappa_{max}$. To plot the geometry of this load case, the projected perturbation direction is $\hat{\boldsymbol{f}}_{p1} = \boldsymbol{W}_m^T|_2 \boldsymbol{f}_{p1} = [-0.52, -0.61]^T$, where $\boldsymbol{W}_m|_2$ is computed in Appendix C. Figure 4.8a plots the projection of this loading direction on the space of the mechanisms, which adds to the projected spring force vector. As long as the resultant vector lies inside the cone, the structure remains rigid. The critical force is the distance from the tip of $\hat{\boldsymbol{f}}_c|_2$ to the boundary along the direction $\hat{\boldsymbol{f}}_{p1}$, shown by a dashed line of length $12.17\kappa_{max}$.

The second perturbation direction we consider is the direction corresponding to the minimum critical force. Recalling Eq. (4.29), the shortest distances to the two boundaries are along the $-\boldsymbol{n}_1|_2$ and $-\boldsymbol{n}_2|_2$ directions. In this example, the spring force vector exactly bisects the cone and the distance to each boundary is equal; we examine the $-\boldsymbol{n}_1|_2$ direction. There is a family of directions $\boldsymbol{f}_p \in \mathbb{R}^6$ whose projection $\hat{\boldsymbol{f}}_p$ is parallel to $-\boldsymbol{n}_1|_2$. However, only one direction corresponds to the minimum critical force, when $||\boldsymbol{f}_p|| = ||\hat{\boldsymbol{f}}_p|| = 1$. In other words, the unit vector $\boldsymbol{f}_p$ pushes exactly in the direction of the mechanisms and has no component perpendicular to the mechanisms. Therefore, its projection onto the mechanisms is also a unit vector. This vector, denoted $\boldsymbol{f}_{p2}$, is given by $\boldsymbol{f}_{p2} = -\boldsymbol{W}_m|_2 \boldsymbol{n}_1|_2 = [0, 0.69, -0.64, 0.34, 0, 0]^T$, which is a force vector that pushes exactly in the mechanism directions, aligned with $-\boldsymbol{n}_1|_2$. The critical magnitude in this direction is $P^*_{min} = r_c = 7.78\kappa_{max}$, which corresponds to the Chebyshev radius. Figures 4.7b and 4.8b plot $\boldsymbol{f}_{p2}$ on the linkage and in the space of the mechanisms.

The final load case we study is in the direction $\boldsymbol{f}_{p3} = [0, 0, 0, -1, 0, 0]^T$, plotted in Figure 4.7c. Its projection onto the mechanisms is $\hat{\boldsymbol{f}}_{p2} = \boldsymbol{W}_m^T|_2 \boldsymbol{f}_{p2} = [0.44, -0.37]^T$. In this direction, the perturbation force is directly counteracted by the unilateral constraints. That is, a large perturbation in this direction leads to large positive reactions in the unilateral constraints. Theoretically, an infinite perturbation force can be withstood in this direction. In the geometric interpretation of Figure 4.8c, the projection $\hat{\boldsymbol{f}}_{p3}$ points in an unbounded direction of the cone.

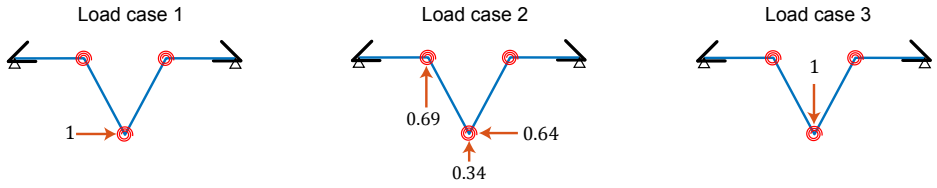

(a) (b) (c)

Figure 4.7: Three cases of perturbation loads applied to configuration 2. (a) Load case 1, where $\boldsymbol{f}_{p1} = [0, 0, 1, 0, 0, 0]^T$. (b) Load case 2, where $\boldsymbol{f}_{p2} = [0, 0.69, -0.64, 0.34, 0, 0]^T$. (c) Load case 3, where $\boldsymbol{f}_{p3} = [0, 0, 0, -1, 0, 0]^T$.

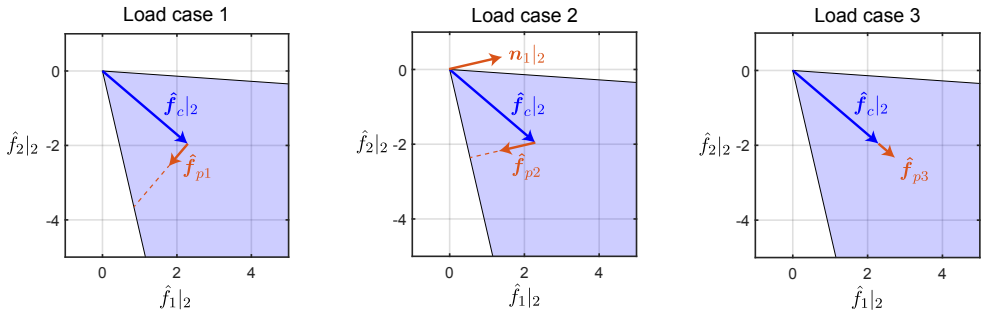

(a) (b) (c)

Figure 4.8: Geometric interpretation of the three load cases. The projection Chebyshev center spring force vector onto the mechanism directions, $\hat{\boldsymbol{f}}_c|_2$, is plotted in blue. The projection of the perturbation direction onto the mechanisms is $\hat{\boldsymbol{f}}_p = \boldsymbol{W}_m^T|_2 \boldsymbol{f}_p$, which is added to the tip of the spring force vector. (a) Load case 1. (b) Load case 2. (c) Load case 3.

These three load cases exemplify the geometric structure of the rigidity conditions. In some directions, the cone is unbounded and an infinite load can be counteracted. In other directions, any perturbation force below some critical value (the distance to the boundary) will remain inside the cone, but a large enough load will overcome the contact forces. Finally, there is a very specific loading direction corresponding to the minimum critical force. This direction pushes exactly along the mechanism directions, and provides a lower bound for the magnitude of any critical force applied to the structure.

4.5.4 Spring energy

Although the rigidity conditions are formulated without any consideration of energy, examining the energy of the linkage is insightful especially for comparison to multi-stability. By computing the energy of the torsion springs in each kinematically admissible configuration of the linkage, it is evident that each rigid target

configuration corresponds to a sharp energy minimum at the boundary of admissible configurations, which follows from the discussion of energy in Section 4.4.4.

In Figure 4.52, energy stored in the torsion springs is plotted for every kinematically admissible configuration. Here, the two degrees of freedom of the linkage are parameterized by θ_1 and θ_5. With this parameterization, the kinematically admissible domain ranges from $0 \leq \theta_1, \theta_5, \leq \pi/4$, where the limits are defined by the angle stops. For each kinematically admissible configuration, the spring energy is computed by inserting the Chebyshev center spring parameters of Eq. (4.61) into Eq. (4.52).

The four corners of the kinematically admissible domain correspond to the four target configurations. Each of the four rigid target configurations corresponds to sharp local energy minimum, which occur since the target configurations lie on the boundary of the admissible domain. In accordance with Eq. (4.57) and the discussion in Section 4.4.4, the slope of the energy is positive along all kinematically admissible directions from each rigid target configuration.

By considering energy, the similarities and differences between multi-configuration rigidity and multi-stability can be highlighted. In both concepts, there are multiple local energy minima. However, the energy minima for rigidity are a special type of minima located at a corner of the kinematically admissible domain with a nonzero slope of the energy in all directions. This nonzero slope corresponds to the spring forces that engage the unilateral constraints, which leads to rigidity. In contrast, multi-stable structures have smooth energy minima.

4.6 Conclusion

This chapter has presented the theory and a design process for multi-configuration rigidity in the statically determinate case. First, conditions for when a configuration is rigid due to an applied force and unilateral constraints are derived. In the case of rigidity due to an applied force and unilateral constraints, a rigid configuration can withstand finite perturbations without displacement, up to some critical threshold magnitude, which depends on the direction of the perturbation. A lower bound on the critical forces can be easily computed as the distance to the closest boundary of the polyhedral cone that describes the rigidity conditions.

The lower bound on critical forces offers a useful quantitative metric for assessing the load-bearing capacity in rigid configurations. Furthermore, it allows for systematic optimal design of embedded springs to achieve multi-configuration rigidity. A

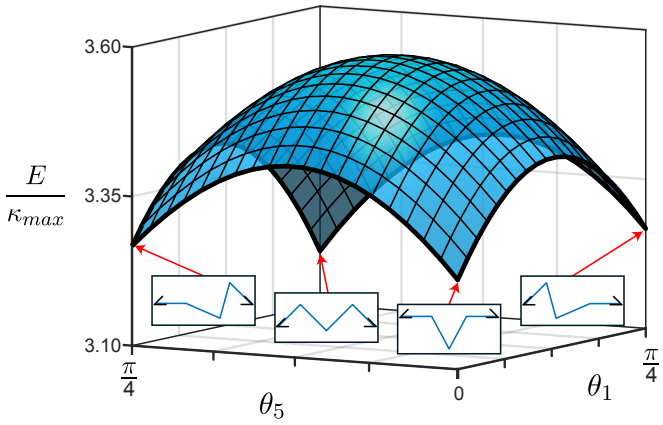

Figure 4.9: Energy in the springs corresponding to the Chebyshev center spring parameters, plotted for all kinematically admissible configurations (θ_1, θ_5 from 0 to $\pi/4$) of the linkage. Each target configuration is rigid, and thus corresponds to a sharp energy minimum at the boundary of kinematically admissible configurations.

design problem was formulated to embed springs throughout the structure such that multiple configurations are made rigid with maximal load-bearing capacity by computing the Chebyshev center solution. Since the conditions for rigidity are based on linearized kinematics about the target configurations, the design problem can be formulated as a linear programming problem bringing guarantees of optimality of solutions. Furthermore, the solution is scalable; the load-bearing capacity in each configuration scales linearly with the upper bound on spring stiffness.

Chapter 5

STRUCTURES WITH STATICALLY INDETERMINATE UNILATERAL CONSTRAINTS

5.1 Introduction

Static indeterminacy occurs when equilibrium alone is insufficient to determine the reaction forces in a structure. This indeterminacy can be resolved by considering the constitutive behavior of structural members [77]. Throughout this thesis, however, it is assumed that all structural members (bars of a linkage or facets of a kirigami pattern) are rigid. For statically indeterminate structures, the assumptions of rigidity lead to non-uniqueness of internal forces.

Static indeterminacy has been extensively studied since the work of Maxwell [85] on computing the degree of indeterminacy, which is the difference between unknown internal forces and number of independent equilibrium equations. Pellegrino and Calladine formulated a rigorous approach for characterizing static indeterminacy based on matrix analysis [86]. Static indeterminacy is a fundamental indicator of the load-bearing capability of a structure [87] and is utilized in both nature and engineering to achieve robust load-bearing structures [88, 89].

In this chapter, we extend the theoretical developments of Chapter 4 to the statically indeterminate case. Specifically, we formulate the Chebyshev center design process to the case when the unilateral constraint reactions are non-unique. To accommodate the non-uniqueness of the unilateral constraint reactions, we leverage concepts in convex geometry. In Chapter 4, the geometric structure of the equilibrium conditions as a convex polyhedral cone was utilized. In this chapter, we further exploit the properties of polyhedral cones to develop rigidity conditions and a lower bound on critical forces in the context of static indeterminacy. In past work, Quirant has studied static indeterminacy in tensegrity structures, which have cables as unilateral constraints, using the geometry of polyhedral cones [90, 91]. They studied statically indeterminate rigid tensegrity structures from the perspective of polyhedral cones, as opposed to the case of rigidity due to unilateral constraints and a force that we develop.

Static indeterminacy is beneficial for designing multi-configuration rigidity. We show in this chapter that having more unilateral constraints can increase the critical

perturbation forces. It follows that having highly indeterminate unilateral constraints can lead to spring designs with a larger Chebyshev radius and therefore a larger load-bearing capacity in rigid configurations compared to the statically determinate case. As a design principle, more unilateral constraints are desirable. For static determinacy, exactly as many unilateral constraints as the number of degrees of freedom of the skeleton structure must be introduced, which poses a difficult problem of where to place unilateral constraints out of a potentially enormous amount of possible combinations. Alternatively, placing as many unilateral constraints as possible is an appealing approach, which leads to static indeterminacy. This offers a practical route to designing multi-configuration rigidity of large structures with many unilateral constraints.

Rigidity conditions and critical perturbation force calculations for the statically indeterminate case are formulated in Section 5.2. Then, Section 5.3 discusses the spring design process followed by a 3-DOF linkage example in Section 5.4. To demonstrate multi-configuration rigidity in a large structure, an 18-DOF kirigami surface with two rigid configurations is presented in Section 5.5.

5.2 Rigidity with statically indeterminate unilateral constraints

In this section, we develop a theoretical framework for rigidity due to an applied force and unilateral constraints with static indeterminacy. We are specifically considering static indeterminacy among unilateral constraints. Following the formulation of equilibrium in Section 4.3.2, only equilibrium in the direction of the mechanisms needs to be considered, which eliminates the bilateral reaction forces $\boldsymbol{\lambda}$ from the analysis. That is, the equilibrium conditions $\hat{\boldsymbol{f}} = \boldsymbol{A}\boldsymbol{\mu}$ with $\boldsymbol{\mu} \geq \mathbf{0}$ from Eq. (4.17) are written only in terms of the unilateral constraint reactions $\boldsymbol{\mu}$.

Static indeterminacy among the unilateral constraints occurs when $n_a > m$, recalling that the dimensions of $\boldsymbol{A}$ are $m \times n_a$ where n_a is the number of active unilateral constraints in the configuration of interest and m is the number of degrees of freedom of the skeleton structure. In this case, given a force $\hat{\boldsymbol{f}}$, the linear system $\hat{\boldsymbol{f}} = \boldsymbol{A}\boldsymbol{\mu}$ is underdetermined and does not admit a unique set of unilateral reactions $\boldsymbol{\mu}$.

In the statically determinate case, $\boldsymbol{A}$ is square and invertible, which allows for computation of the lower bound on critical perturbation forces using $\boldsymbol{A}^{-1}$ (see Section 4.3.6). This lower bound provides the foundation for the optimal spring design process. However, in the statically indeterminate case, $\boldsymbol{A}$ is not invertible. By re-examining rigidity due to an applied force and unilateral constraints from

the lens of convex geometry, formulations are developed that apply to the statically indeterminate case.

5.2.1 Two representations of equilibrium

The equilibrium conditions in the presence of unilateral constraints require that the applied force $\hat{\boldsymbol{f}}$ belongs to the convex polyhedral cone C, which is defined by $C = \{\hat{\boldsymbol{f}} \mid \hat{\boldsymbol{f}} = \boldsymbol{A}\boldsymbol{\mu},\ \boldsymbol{\mu} \geq \boldsymbol{0}\}$. This constitutes the *vector representation*, or V-representation, of the equilibrium cone C. In this representation, $\hat{\boldsymbol{f}}$ is a conic combination (a linear combination with non-negative coefficients) of the vectors in the columns of $\boldsymbol{A}$

$$\begin{aligned} \hat{\boldsymbol{f}} &= \sum_{i=1}^{n_a} \mu_i \boldsymbol{a}_i \\ \mu_i &\geq 0, \quad i = 1, ..., n_a \end{aligned} \tag{5.1}$$

where $\boldsymbol{a}_i$ is column i of $\boldsymbol{A}$.

A well-known result in convex geometry is that polyhedral cones have two equivalent representations. They can be represented as a conic combination of vectors, or equivalently as the intersection of a set of half-spaces through the origin. From Theorem 1.3 of [92], the following representations of the cone C are equivalent

$$C = \{\hat{\boldsymbol{f}} \mid \hat{\boldsymbol{f}} = \boldsymbol{A}\boldsymbol{\mu},\ \boldsymbol{\mu} \geq \boldsymbol{0}\} \tag{5.2}$$

$$C = \{\hat{\boldsymbol{f}} \mid \boldsymbol{N}\hat{\boldsymbol{f}} \geq \boldsymbol{0}\}. \tag{5.3}$$

Along with the V-representation of Eq. (5.2), the cone C can equivalently be represented as the intersection of half-spaces passing through the origin in Eq. (5.3). The rows of the matrix $\boldsymbol{N} \in \mathbb{R}^{h \times m}$ contain normal vectors to these half-spaces:

$$\boldsymbol{N} = \begin{bmatrix} \boldsymbol{n}_1^T \\ \vdots \\ \boldsymbol{n}_h^T \end{bmatrix}. \tag{5.4}$$

This is denoted as the *half-space representation*, or H-representation of the cone. The number of half-spaces h in the H-representation can vary widely, which is discussed in Section 5.2.2.

The V-representation of equilibrium naturally arises in the principle of virtual work in Section 4.3.2 and $\boldsymbol{A}$ is directly computed from the linearized kinematics about a target configuration. Yet, the H-representation of equilibrium is a useful tool for studying perturbation forces. This is evident from the statically determinate case,

where it is straightforward to compute the corresponding H-representation since $\boldsymbol{A}$ is invertible, leading to $\boldsymbol{N} = \boldsymbol{A}^{-1}$. With the H-representation in hand, we showed in Section 4.3.6 that the lower bound on critical perturbations forces can be computed, which is the basis for the Chebyshev center spring design problem of Section 4.4. Since the H-representation allows for the lower bound critical perturbation force to be computed, it is desirable to convert from the V- to the H-representations in statically indeterminate problems as well.

In the statically indeterminate case, computing the matrix $\boldsymbol{N}$, given $\boldsymbol{A}$, is not as straightforward as in the determinate case, yet it is a well-studied problem called the *facet enumeration* problem. The objective of the facet enumeration is to compute the half-spaces that define a polyhedral cone given its V-representation. The facet enumeration problem is closely related to the convex hull problem that converts vertices of a bounded polytope to the facets of a polytope [93]. There are well-established algorithms for facet enumeration, such as the double description method [94] based on Fourier-Motzkin elimination [92], and pivoting tree-search methods [95, 96].

5.2.2 An upper bound on the number of half-spaces

An interesting aspect of facet enumeration problems is that the number of half-spaces h in the H-representation can vary greatly given the dimensions m and n_a of the $\boldsymbol{A}$ matrix. That is, two V-representation cones in the same dimension with the same number of vectors can have H-representations with a very different number of half-spaces h. Generally, h can only be determined by fully solving the facet enumeration problem. This can pose a challenge for problems set in high dimension, since h can potentially be very large.

There is an upper bound on the number of half-spaces in the H-representation, which provides a useful guide in the context of large problems. To obtain the upper bound on h, the bound on the number of faces of polytopes can be utilized, which can be converted to bounds on the number of faces of a polyhedral cone. Polytopes are bounded geometric objects defined either by the convex hull of a set of points or as the intersection of half-spaces [92]. McMullen's upper bound theorem [97] states that a polytope with a vertices in b dimensions, has at most h_{max} half-spaces in the H-representation where, using the notation of [98],

$$h_{max}(a, b) = \binom{a - \lfloor \frac{b+1}{2} \rfloor}{a - b} + \binom{a - \lfloor \frac{b+2}{2} \rfloor}{a - b}. \tag{5.5}$$

The floor function is denoted by $\lfloor\ \rfloor$. This upper bound for polytopes can be adapted to polyhedral cones since the projection of a cone in $\mathbb{R}^m$ onto a hyperplane corresponds to a polytope in $\mathbb{R}^{m-1}$. Figure 5.1 illustrates the projective transformation from cone C to polytope $\mathcal{P}$. This allows the upper bound for polytopes to be adapted to cones since the number of vectors in C equals the number of vertices in $\mathcal{P}$ and they both have the same number of facets. For a deeper discussion of projective transformations of cones, see Section 2.6 of [92].

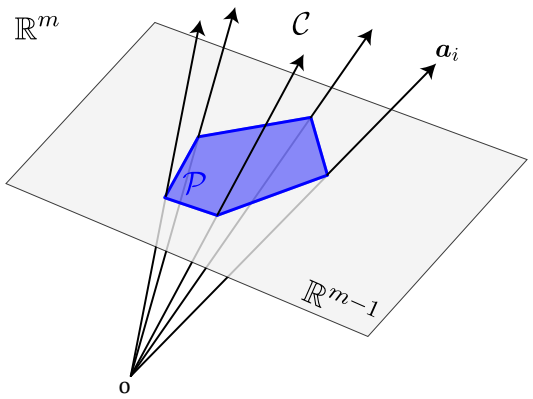

Figure 5.1: The cone C in m-dimensional space, which is defined by vectors $\boldsymbol{a}_i$ where $i = 1, ..., n_a$, can be projected onto a polytope $\mathcal{P}$ in $(m-1)$-dimensional space.

The upper bound theorem can be adapted to the equilibrium cone, which consists of n_a vectors in m dimensions. Computing the polytope upper bound for $a = n_a$ and $b = m - 1$, the upper bound for the number of facets of C is

$$h_{max}(n_a, m) = \binom{n_a - \lfloor \frac{m}{2} \rfloor}{n_a - m + 1} + \binom{n_a - \lfloor \frac{m+1}{2} \rfloor}{n_a - m + 1}. \tag{5.6}$$

This represents an upper bound on the number of rows of $\boldsymbol{N}$ in the H-representation given the number of unilateral constraints and degrees of freedom of the skeleton structure. Although the actual size of $\boldsymbol{N}$ may be much lower than the upper bound, it provides a useful guide when considering structures with many degrees of freedom unilateral constraints.

5.2.3 Rigidity conditions using the V-representation

Conditions for rigidity due to a force and statically indeterminate unilateral constraints are formulated using both the V- and H-representations. We start by considering the V-representation.

In the statically determinate case, the two conditions for rigidity are that all unilateral reactions are positive and that there are enough unilateral constraints to block motion of all mechanisms, from Theorem 4.3. In the indeterminate case, there is not a unique set of unilateral reactions. However, it is the existence of an entirely positive set of reactions among all possible sets of reactions satisfying equilibrium that corresponds to rigidity.

Theorem 5.1. *A configuration is rigid due to unilateral constraints and an applied force if*

$$null\left(\begin{bmatrix}\boldsymbol{C}^b\\ \boldsymbol{C}^u\end{bmatrix}\right) = \emptyset \tag{5.7}$$

and

$$\exists \boldsymbol{\mu} \;\mid\; \hat{\boldsymbol{f}} = \boldsymbol{A}\boldsymbol{\mu},\;\; \mu_i > 0,\; i = 1, ..., n_a. \tag{5.8}$$

Proof. For any first-order admissible displacement $\boldsymbol{d}_m = \boldsymbol{W}_m\boldsymbol{\alpha}$ away from the configuration, the unilateral constraints must do no work. Recalling Section 4.3.2, the work of the unilateral constraints corresponding to this displacement is given by

$$\boldsymbol{\mu}^T\boldsymbol{\delta g} = \boldsymbol{\mu}^T\boldsymbol{C}^u\boldsymbol{W}_m\boldsymbol{\alpha} = 0. \tag{5.9}$$

If Eq. (5.8) holds, then any solution to the linear system $\hat{\boldsymbol{f}} = \boldsymbol{A}\boldsymbol{\mu}$ can be written in the form $\boldsymbol{\mu} = \boldsymbol{\mu}_p + \boldsymbol{\mu}_h$. Here, $\boldsymbol{\mu}_p$ is a particular solution with all positive entries and $\boldsymbol{\mu}_h$ is a homogeneous solution in $null(\boldsymbol{A})$. Inserting $\boldsymbol{\mu} = \boldsymbol{\mu}_p + \boldsymbol{\mu}_h$ into Eq. (5.9),

$$(\boldsymbol{\mu}_p^T + \boldsymbol{\mu}_h^T)\boldsymbol{C}^u\boldsymbol{W}_m\boldsymbol{\alpha} = 0 \tag{5.10}$$

$$\boldsymbol{\mu}_p^T\boldsymbol{C}^u\boldsymbol{W}_m\boldsymbol{\alpha} = 0, \tag{5.11}$$

noting that $\boldsymbol{\mu}_h^T\boldsymbol{C}^u\boldsymbol{W}_m = \boldsymbol{0}$ since $\boldsymbol{\mu}_h$ is in the null space of $\boldsymbol{A} = \boldsymbol{W}_m^T\boldsymbol{C}^{uT}$. Rewriting Eq. (5.11) as a summation,

$$\sum_{i=1}^{n_a} \mu_{pi}(\boldsymbol{C}^u\boldsymbol{W}_m\boldsymbol{\alpha})_i = 0. \tag{5.12}$$

All components of $\boldsymbol{\mu}_p$ are positive if Eq. (5.8) holds and all components of $\boldsymbol{C}^u\boldsymbol{W}_m\boldsymbol{\alpha}$ are non-negative from Eqs. (4.10) and (4.11), so the left-hand side of Eq. (5.12) is a summation of entirely non-positive terms. The only way to satisfy Eq. (5.12) is if all terms of the summation are zero, requiring

$$\boldsymbol{\alpha} \in null(\boldsymbol{C}^u\boldsymbol{W}_m). \tag{5.13}$$

Finally, Eq. (5.7) is equivalently stated as

$$null(\boldsymbol{C}^b) \cap null(\boldsymbol{C}^u) = \emptyset \tag{5.14}$$

$$\boldsymbol{C}^u \boldsymbol{W}_m \boldsymbol{\alpha} = \boldsymbol{0} \Rightarrow \boldsymbol{\alpha} = \boldsymbol{0} \tag{5.15}$$

$$null(\boldsymbol{C}^u \boldsymbol{W}_m) = \emptyset, \tag{5.16}$$

where Eq. (5.15) follows from (5.14) since $\boldsymbol{W}_m \boldsymbol{\alpha} \in null(\boldsymbol{C}^b)$. Equations (5.16) and (5.13) require that $\boldsymbol{\alpha} = \boldsymbol{0}$. This implies that there is no first-order admissible displacement $\boldsymbol{d} = \boldsymbol{W}_m \boldsymbol{\alpha}$ and the configuration is infinitesimally rigid. □

Theorem 5.1 is a generalization of Theorem 4.1, which applies whether or not there is static indeterminacy.

As with the statically determinate case, a rigid configuration can resist perturbation forces of any direction up to a finite magnitude. For a force $\boldsymbol{f}_0$ that satisfies the rigidity conditions, the question at hand is whether the resultant force $\boldsymbol{f} = \boldsymbol{f}_0 + P\boldsymbol{f}_p$ after applying a perturbation force of magnitude P in direction $\boldsymbol{f}_p$ still satisfies the rigidity conditions. Computation of critical perturbation forces in a given direction can be achieved using the V-representation by solving the linear program

$$\begin{aligned} \max P \quad \text{subject to} \quad & \boldsymbol{W}_m^T \left(\boldsymbol{f}_0 + P\boldsymbol{f}_p \right) = \boldsymbol{A}\boldsymbol{\mu} \\ & \boldsymbol{\mu} \geq \boldsymbol{0}. \end{aligned} \tag{5.17}$$

The lower bound on critical perturbation forces, however, cannot be directly computed using the V-representation. This is where the utility of the H-representation becomes evident.

5.2.4 Rigidity conditions using the H-representation

Conditions for rigidity can also be stated in terms of the H-representation, which are developed under the premise that a configuration that is rigid due to contact and an applied force can rigidly resist a perturbation force in any direction up to some finite magnitude.

Theorem 5.2. *A configuration is rigid due to unilateral constraints and an applied force if Eq.* (5.7) *is satisfied along with*

$$\boldsymbol{N}\hat{\boldsymbol{f}} > \boldsymbol{0}. \tag{5.18}$$

Proof. Equation (5.16) is equivalently stated as $null(\boldsymbol{A}^T) = \emptyset$. This implies that the column space of $\boldsymbol{A}$ is full-dimensional with dimension m; the columns of $\boldsymbol{A}$ span

$\mathbb{R}^m$. Therefore, the cone C has a nonempty interior: $int(C) \neq \emptyset$. Equation (5.18) requires that $\hat{\boldsymbol{f}} \in int(C)$. By definition, if $\hat{\boldsymbol{f}} \in int(C)$, then a finite scalar ϵ exists such that $\hat{\boldsymbol{f}} + \epsilon \hat{\boldsymbol{f}}_p \in int(C)$ for any vector $\hat{\boldsymbol{f}}_p \in \mathbb{R}^m$. Therefore, a finite perturbation force in any direction can be resisted, which corresponds to rigidity. □

Theorem 5.2 is equivalent to Theorem 5.1, noting that the existence of a positive $\boldsymbol{\mu}$ in the V-representation corresponds to $\hat{\boldsymbol{f}}$ being interior to C, since C is full dimensional, by Lemma 3.2 of [99].

Critical perturbation forces can also be computed using the H-representation. For a perturbation force applied about $\boldsymbol{f}_0$ in direction $\boldsymbol{f}_p$ with magnitude P, the critical perturbation force is the solution to the linear program

$$\max P \quad \text{subject to} \quad \boldsymbol{N}\boldsymbol{W}_m^T \left(\boldsymbol{f}_0 + P\boldsymbol{f}_p \right) \geq \boldsymbol{0}. \tag{5.19}$$

The critical magnitude P^* is equivalent whether computed by Eq. (5.19) or Eq. (5.17) since the V and H-representations equivalently describe C.

The advantage of working with the H-representation is that a lower bound can be computed on the critical forces. The minimum distance from $\hat{\boldsymbol{f}}_0$ to each half-space of the cone is

$$P_i^* = \frac{\boldsymbol{n}_i^T}{||\boldsymbol{n}_i||} \hat{\boldsymbol{f}}_0, \quad i = 1, ..., h. \tag{5.20}$$

The only difference here from Eq. (4.29) in the statically determinate case is that there are h half-spaces instead of n_a.

The lower bound on the critical perturbation force corresponds to the distance from $\hat{\boldsymbol{f}}_0$ to the closest half-space, which is simply the minimum of the distances to each half-space:

$$P_{min}^* = \min\{P_1^*, ..., P_h^*\}. \tag{5.21}$$

The ability to compute the distance to each half-space and a lower bound on critical forces, which requires the H-representation, provides a basis for the spring design problem by allowing the Chebyshev center to be computed.

5.2.5 Positive independence and the benefit of static indeterminacy

Static indeterminacy is desirable from the perspective of the load-bearing capacity of a rigid configuration. Generally, more unilateral constraints will lead to larger

perturbation forces. In other words, adding more vectors in the V-representation (where each vector corresponds to a unilateral constraint) can lead to a larger equilibrium cone C.

This becomes evident through the concept of *positive independence*. The set of vectors $\{\boldsymbol{a}_1, ..., \boldsymbol{a}_{n_a}\}$ is a positively independent set if and only if

$$\boldsymbol{a}_j = \sum_{\substack{i=1 \\ i \neq j}}^{n_a} \mu_i \boldsymbol{a}_i, \quad \boldsymbol{\mu} \geq 0, \tag{5.22}$$

has no solution for all vectors in the set, $j = 1, ..., n_a$ [100] (referred to as conic independence in some texts [101]). That is, the set is positively independent if and only if no vector can be described as a conic combination of the other vectors.

If a set of vectors is positively independent, then removing any vector from the set will decrease the size of the corresponding cone. This is evident in Figure 5.1; removing any vector reduces the interior of C. Alternatively, adding a vector to C in Figure 5.1 would increase its size if the added vector is outside of C. However, adding a conically dependent vector that is inside C will not increase its size.

A useful guiding design principle for multi-configuration rigidity arises from this thinking. Introducing more positively independent unilateral constraints leads to larger load-bearing capacity of a rigid configuration. Thus, for large problems, it is beneficial to place many unilateral constraints.

Finally, we note that in two-dimensional space, a pointed cone (cones that contains no lines, which is the case for all examples in this thesis) can only have two positively independent vectors. However, in three dimensions or higher, there is no limit on the number of positively independent vectors [101]. For this reason, the simple example considered in Section 5.4 is a 3-DOF linkage to highlight the benefit of static indeterminacy, instead of continuing the 2-DOF linkage previously studied in Chapter 4.

5.3 Spring design problem

Now that the concept of rigidity due to an applied force and statically indeterminate unilateral constraints has been developed, the multi-configuration rigidity design problem can be revisited. A procedure for designing structures with multiple rigid configurations is presented that, by incorporating static indeterminacy, opens the door to the design of large, many-DOF structures. First, the design problem is set up by placing unilateral constraints and springs throughout the skeleton structure.

Then, the spring parameters are systematically designed to satisfy rigidity in all target configurations such that the lower bound on critical force in each configuration is maximized.

5.3.1 Design problem setup

Given a set of target configurations of a skeleton structure, the goal of the design problem is to embed springs and unilateral constraints to achieve rigidity in each target configuration such that the smallest critical perturbation force of all target configurations is maximized.

First, a set of unilateral constraints is placed throughout the structure to be active in the target configurations. As discussed in Section 5.2.5, it is advantageous to place as many unilateral constraints as possible. However, after placing unilateral constraints throughout the structure, there must be a kinematic path connecting all target configurations; otherwise the structure could not reconfigure between target configurations. This condition complicates the unilateral constraint placement step for large structures with many-DOF. In this work, kinematic simulations are conducted to verify that a kinematic path exists between the target configurations after placing unilateral constraints. It can be a challenging problem to verify if two configurations are connected by a continuous kinematic path for multi-DOF folding structures, which have highly nonlinear kinematics. However, if a kinematic path is found that does not violate the unilateral constraints (for example, by the algorithm of Appendix B), those constraints can be used. If a path is not found using some kinematic pathfinding algorithm, it is generally difficult to guarantee that a path does not exist between two configurations. That is, if the pathfinding algorithm of Appendix B does not find a solution, a more sophisticated pathfinding algorithm (e.g., a random tree search [102]) may be able to find a path. For the examples in this thesis, we verify that a path exists for chosen unilateral constraints, but a general constraint placement method respecting the condition that all target configurations remain connected by kinematic paths remains an open problem.

The next step in the problem setup is spring placement. Embedding as many springs as possible is desirable for the sake of maximizing the number of design variables. The primary restriction for spring placement arises from fabrication considerations; for practical application, springs must be able to be physically realized.

5.3.2 Systematic spring parameter design

Once the unilateral constraints and springs are placed throughout the skeleton structure, what remains is to compute spring parameters. Spring parameter design is an entirely systematic process, achieved by modifying the Chebyshev center design methodology of Chapter 4 for the statically indeterminate case.

First, the matrix $\boldsymbol{A}$ is computed in each configuration, which gives the V-representation of C. The matrix $\boldsymbol{A}$ is entirely determined from the unilateral and bilateral constraint gradients for each target configuration.

Second, the matrix $\boldsymbol{N}$ is computed in each target configuration by solving the facet enumeration problem with $\boldsymbol{A}$ as the input. There are several numerical implementations for solving the facet enumeration, such as lrslib [103] and cddlib [104]. The facet enumeration problem can be computationally expensive for problems with many unilateral constraints in high dimension. The upper bound of Section 5.2.2 is useful for assessing the worst case size of $\boldsymbol{N}$.

The final step for spring design is to solve the Chebyshev center linear program to compute spring parameters, which requires $\boldsymbol{N}$. Generally, the Chebyshev center cannot be computed directly from the V-representation [79], which is why the facet enumeration step is required. The Chebyshev center computation takes the same form as for the statically determinate case of Eq. (4.50), except that there are h normal vectors in the statically indeterminate case. The linear program for the statically indeterminate case is given by:

$$
\begin{aligned}
&\max r \quad \text{subject to} \\
&P_i^*|_j = \left(\frac{\boldsymbol{n}_i^T}{||\boldsymbol{n}_i||} \boldsymbol{W}_m^T \boldsymbol{C}^{sT} \begin{bmatrix} \boldsymbol{M}_1 & \boldsymbol{0} \\ \boldsymbol{0} & \boldsymbol{M}_2 \end{bmatrix} \right)_j \begin{bmatrix} \mathbf{k} \\ \boldsymbol{\sigma}^0 \\ \boldsymbol{\kappa} \\ \boldsymbol{m}^0 \end{bmatrix} \geq r, \quad i = 1, ..., h, \;\; j = 1, ..., n_t \\
&\boldsymbol{0} \leq \begin{bmatrix} \mathbf{k} \\ \boldsymbol{\kappa} \end{bmatrix} \leq \begin{bmatrix} \mathbf{k}_{max} \\ \boldsymbol{\kappa}_{max} \end{bmatrix} \\
&\begin{bmatrix} \boldsymbol{M}_3 & \boldsymbol{0} \\ \boldsymbol{0} & \boldsymbol{M}_4 \end{bmatrix} \begin{bmatrix} \mathbf{k} \\ \boldsymbol{\sigma}^0 \\ \boldsymbol{\kappa} \\ \boldsymbol{m}^0 \end{bmatrix} \leq \boldsymbol{0}.
\end{aligned}
\tag{5.23}
$$

This is a linear program with $hn_t + 4p + 4q$ linear inequalities and $2p + 2q + 1$ variables. For problems with very large h, this represents another potentially expensive computation. However, efficient linear program solvers exist that can handle large problems. The example presented in Section 5.5 has on the order of 10^7 constraints.

5.4 3-DOF linkage example

The first example we present is the design of a 3-DOF linkage with two rigid configurations. This low-dimensional example allows for the equilibrium cone C to be visualized, providing intuitive insights into the statically indeterminate rigidity formulations.

5.4.1 Problem setup

To obtain a 3-DOF linkage ($m = 3$), we added an extra bar to the 2-DOF linkage of Chapter 4. The resulting linkage is shown in Figure 5.2 in two target configurations. The bar lengths in mm are $L_1 = L_5 = 75$, $L_2 = L_4 = 94.75$, and $L_3 = 37.5$. The corresponding bilateral constraints are

$$\boldsymbol{h}(\boldsymbol{x}) = \boldsymbol{L}(\boldsymbol{x}) - \begin{bmatrix} 75 \\ 94.75 \\ 37.5 \\ 94.75 \\ 75 \end{bmatrix} = \mathbf{0}. \tag{5.24}$$

The hinge angles in target configuration 1 are $\theta_1 = \theta_6 = \pi/4$, $\theta_2 = \theta_5 = \pi/2$, and $\theta_3 = \theta_4 = 3\pi/4$. The hinge angles in target configuration 2 are $\theta_1 = \theta_6 = 0$ and $\theta_2 = \theta_3 = \theta_4 = \theta_5 = 2.063$.

For the unilateral constraint placement step, we choose to place $n_a = 4$ active unilateral constraints in each target configuration in the form of angle stops. More constraints could be placed, but we limit this problem to four for simplicity, which is the smallest number that leads to static indeterminacy. Angle stops are introduced on hinges 1, 2, 5, and 6 that limit the hinge angles to between their two target

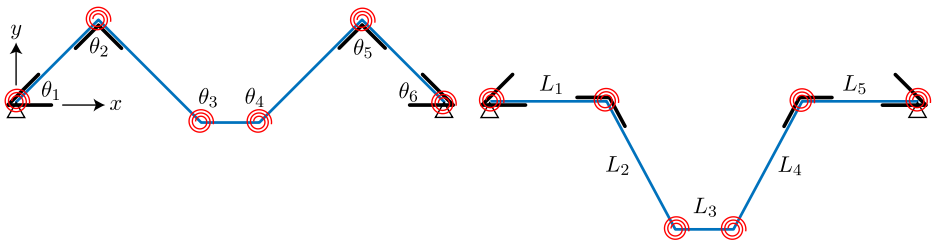

(a) (b)

Figure 5.2: Three-DOF linkage geometry. The red coils at each hinge represent linear torsion springs and the brackets on hinges 1, 2, 5, and 6 represent unilateral constraints on the fold angles. Hinges 1 and 5 have pinned boundary conditions. (a) Target configuration 1. (b) Target configuration 2.

configuration values. The corresponding unilateral constraints are

$$\boldsymbol{g}(\boldsymbol{x}) = \begin{bmatrix} \theta_1(\boldsymbol{x}) \\ -\theta_1(\boldsymbol{x}) \\ \theta_2(\boldsymbol{x}) \\ -\theta_2(\boldsymbol{x}) \\ \theta_5(\boldsymbol{x}) \\ -\theta_5(\boldsymbol{x}) \\ \theta_6(\boldsymbol{x}) \\ -\theta_6(\boldsymbol{x}) \end{bmatrix} + \begin{bmatrix} -\pi/4 \\ 0 \\ -2.063 \\ \pi/2 \\ -2.063 \\ \pi/2 \\ -\pi/4 \\ 0. \end{bmatrix} \leq \mathbf{0}. \tag{5.25}$$

It is straightforward to verify that a path exists between the two target configurations that respects the unilateral constraints. For example, the symmetric path between target configurations, where $\theta_1 = \theta_6$, $\theta_2 = \theta_5$, and $\theta_2 = \theta_4$, does not violate the unilateral constraints.

The final step in the design problem setup is spring placement. A torsion spring is placed on each hinge, leading to $q = 6$ torsion springs and 12 design variables: $\kappa_i, \theta_i^0,\ i = 1, ..., 6$. The rest angles of the springs are restricted to between $-\pi$ and π, following the previous example of Chapter 4. The maximum allowable stiffness κ_{max} of each spring is left unspecified, which acts as a scaling factor for the solution.

5.4.2 Spring parameter computation

What remains is to compute the spring parameters that correspond to the Chebyshev center solution, which is an entirely systematic process. The first step is to compute $\boldsymbol{A}$, which follows directly from the constraint gradients. In this example, we omit the computation of intermediate matrices, but their computation follows the same

procedure presented in Appendix C for the 2-DOF example. The resulting $\boldsymbol{A}$ matrices have $m = 3$ rows and $n_a = 4$ columns. In the two target configurations,

$$\begin{aligned} \boldsymbol{A}|_1 &= \begin{bmatrix} -0.0031 & 0.0016 & -0.0012 & 0.0054 \\ 0.0079 & 0.0053 & -0.0034 & 0.0016 \\ -0.0017 & -0.0085 & 0.0095 & 0.0065 \end{bmatrix} \\ \boldsymbol{A}|_2 &= \begin{bmatrix} 0.0044 & 0.0010 & -0.0023 & -0.0057 \\ -0.0075 & -0.0140 & 0.0083 & 0.0019 \\ -0.0044 & -0.0010 & -0.0110 & -0.0077 \end{bmatrix}. \end{aligned} \tag{5.26}$$

These matrices constitute the V-representation of the equilibrium cone C. Figure 5.3a plots the columns of $\boldsymbol{A}|_2$ to illustrate what the V-representation of the equilibrium cone looks like for a target configuration.

The H-representation of the cone is computed by solving the facet enumeration problem. We used the lexicographic reverse search (LRS) algorithm [95] for facet enumeration. The lrslib implementation of this algorithm [103] and its Matlab interface [105] were used for the facet enumeration computations. The corresponding matrix $\boldsymbol{N}$ of half-space normal vectors in each configuration is

$$\boldsymbol{N}|_1 = \begin{bmatrix} -0.5240 & 0.8208 & 0.2272 \\ -0.6151 & 0.7174 & 0.3271 \\ 0.8165 & 0.4082 & 0.4082 \\ 0.8811 & 0.4007 & 0.2511 \end{bmatrix}, \quad \boldsymbol{N}|_2 = \begin{bmatrix} 0.8115 & 0.0979 & -0.5761 \\ 0.5678 & -0.5960 & -0.5678 \\ -0.8899 & -0.4335 & -0.1418 \\ -0.7071 & 0.000 & -0.7071 \end{bmatrix}. \tag{5.27}$$

Both configurations have an H-representation with $h = 4$ facets. This is equal to the upper bound on the number of facets from Eq. (5.6), $h_{max} = 4$, though the upper bound is more useful for assessing high-dimensional problems. To illustrate the H-representation, the facets of C for target configuration 2 are shaded in Figure 5.3b, where each facet is defined by the normal vectors that are the rows of $\boldsymbol{N}|_2$.

From the illustrations of the two representations of C in Figure 5.3, we can gain insights about rigidity and static indeterminacy. In the V-representation, there are $n_a = 4$ vectors in $m = 3$ dimensions, corresponding to static indeterminacy since $n_a > m$. The four vectors are positively independent since none of the vectors lie in the cone of the other three. Therefore, removing any of the four vectors reduces the size of C. This illustrates the reason why static indeterminacy is beneficial from the perspective of perturbation forces; having four unilateral constraints instead of only three leads to a larger equilibrium cone C and therefore a larger load-bearing capacity.

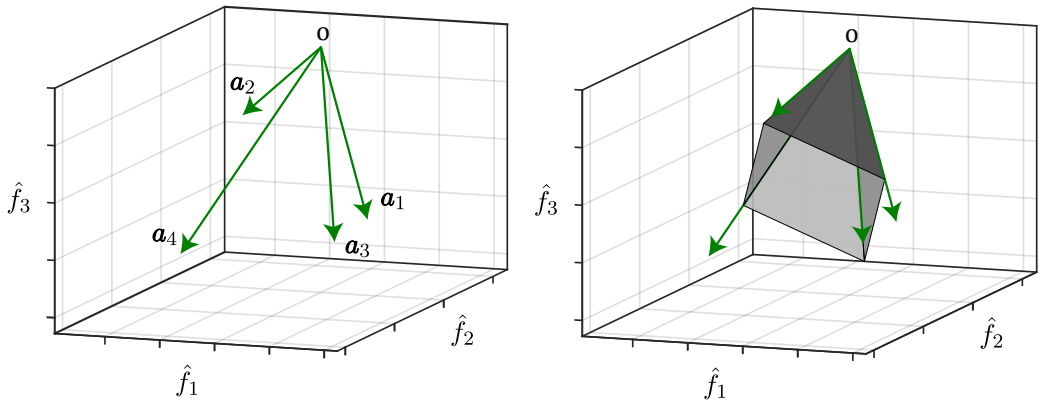

(a) (b)

Figure 5.3: Equilibrium cone C for target configuration 2 of the 3-DOF linkage. (a) V-representation of the cone defined by vectors $\boldsymbol{a}_1$, $\boldsymbol{a}_2$, $\boldsymbol{a}_3$, and $\boldsymbol{a}_4$. (b) The H-representation of the cone is defined by $h = 4$ facets highlighted in gray.

The final step in the spring design process is solving the Chebyshev center linear program of Eq. (5.23), which yields the solution

$$\boldsymbol{\kappa}_c = \begin{bmatrix} 0.11 \\ 1 \\ 1 \\ 1 \\ 1 \\ 0.11 \end{bmatrix} \kappa_{max}, \qquad \boldsymbol{\theta}^0 = \begin{bmatrix} \pi \\ \pi \\ \pi \\ \pi \\ \pi \\ \pi \end{bmatrix}. \tag{5.28}$$

The corresponding Chebyshev radius is $r_c = 3.96\kappa_{max}$, where r_c is in Newtons if κ_{max} is specified in Nm/rad. This provides a guarantee that any load with magnitude less than r_c applied to either configuration can be resisted without causing any displacements. For reference, if the torsion springs of the prototype in Chapter 6, which have a nominal stiffness of 0.230 Nm/rad, define the maximum stiffness, the corresponding Chebyshev radius is 0.91 N.

5.4.3 Comparison to statically determinate constraints

To exemplify the fact that having more positively independent unilateral constraints leads to a higher load-bearing capacity, we can draw comparison to the statically determinate case. So far, we have considered four active unilateral constraints in each target configuration of the 3-DOF linkage. Removing one active unilateral constraint in each target configuration leads to static determinacy. Since the columns

of $\boldsymbol{A}$ are positively independent in each target configuration, removing one constraint will reduce the size of C leading to a smaller Chebyshev radius and thus a smaller lower bound on critical perturbation forces.

We can quantitatively show this by considering all possible statically determinate combinations of the unilateral constraints. To achieve static determinacy in both target configurations, one of the four active constraints in each configuration can be removed. This leads to 16 possible combinations of active constraints between the two target configurations. For each of these combinations, we can compute the Chebyshev center. Of all 16 combinations, removing stops on hinges 3 and 4 in configurations 1 and 2, respectively, leads to the largest Chebyshev radius, $r_c = 3.09\kappa_{max}$. As expected, this is smaller than the Chebyshev radius of $3.96\kappa_{max}$ if all four stops are included in each configuration. This verifies that the load-bearing capacity of each target configuration is reduced if less unilateral constraints are considered.

5.5 18-DOF morphing surface example

To demonstrate design process on a large structure, a kirigami surface is designed to have two rigid configurations. This provides a connect between multi-configuration rigidity and the kirigami pattern synthesis framework of Chapter 3.

5.5.1 Problem setup

In this example, we design the kirigami pattern from Section 3.7.2 to have two rigid configurations: the spherical and saddle configurations shown in Figure 3.17. This fold pattern has $m = 18$ degrees of freedom.

For unilateral constraint placement, angle stops are placed on all 48 mountain folds to be active in both configurations. Specifically, denote $\boldsymbol{\theta}_M$ as a 48-dimensional vector containing the mountain fold angles. The unilateral constraints are placed according to

$$\min\{\theta_{Mi}|_1, \theta_{Mi}|_2\} \leq \theta_{Mi}(\boldsymbol{x}) \leq \max\{\theta_{Mi}|_1, \theta_{Mi}|_2\}, \tag{5.29}$$

which limits each mountain fold angle to range between its value in target configuration 1 (spherical) and target configuration 2 (saddle). This results in $n_a = 48$ active unilateral constraints in both target configurations.

After placing these unilateral constraints, it must be verified that a kinematic path exists connecting the two target configurations. In this case, the pathfinding algorithm of Appendix B can find a path between target configurations that obeys the

unilateral constraints. Figure 5.4 plots the mountain fold angles along this path. The path starts at the saddle configuration and ends at the spherical configuration. Fold angles are plotted against the arc length along the kinematic path. The key feature of this path is that all of the mountain fold angles remain between their start and end values throughout the path. The existence of this path gives a guarantee that the pattern can be continuously reconfigured between target configurations after the unilateral constraints are placed. Since the pattern has many degrees of freedom, there may be many such paths, but we only need the guarantee that at least one such path exists.

The final step in the design problem setup is spring placement. Torsion springs are placed on all mountain and valley folds of the pattern. This introduces $q = 72$ springs, leading to 144 design variables corresponding to the stiffness and rest angle of each spring. Again, the rest angles are limited to the range between $-\pi$ and π. The edge length of the tiles is set to 4 cm to reflect a physically realistic length scale.

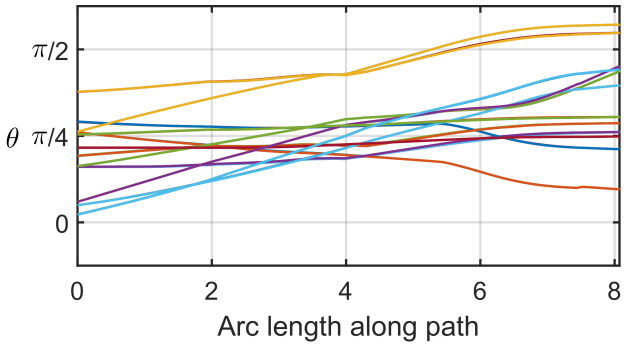

Figure 5.4: Mountain fold angles along a path from the saddle to the spherical configuration. The fold angles stay between their start (saddle configuration) and end (spherical configuration) values, indicating that angle stops can be placed on all mountain folds in both configurations without cutting off a kinematic path between the two configurations.

5.5.2 Spring parameter computation

Following the placement of unilateral constraints and springs, the spring parameters are systematically computed. First, the constraint gradients are computed in each configuration. Bilateral constraints for the rigid-folding plates of the kirigami pattern are formulated according to the kinematic model of Appendix A. Throughout the analysis, a single tile is fixed in space to remove rigid body motion; the fixed tile is highlighted in blue in Figure 5.5c. The corresponding $\boldsymbol{A}$ matrix in each configuration has $m = 18$ rows and $n_a = 48$ columns. The 48 columns of $\boldsymbol{A}$ are a

positively independent set of vectors in both configurations, indicating that removing any of the unilateral constraints would decrease the size of C. Positive independence can be checked through linear programming to determine if any vectors in the set belong to the cone defined by the others [101].

Next, facet enumeration is performed to compute the matrix $\boldsymbol{N}$ that defines the H-representation. Again, the lrslib [103] and its Matlab interface GeoCalcLib [105] are used to perform facet enumeration. The resulting H-representations have $h|_1 = 5,910,381$ half-spaces in the spherical configuration and $h|_2 = 10,626,252$ half-spaces in the saddle configuration, where $\boldsymbol{N}|_1$ has dimension $h|_1 \times m$ and $\boldsymbol{N}|_2$ has dimension $h|_2 \times m$.

The large difference in the number of half-spaces exemplifies the large variation in the output of the facet enumeration problem. In fact, the upper bound corresponding to $m = 18$ and $n_a = 48$, from Eq. (5.6), is $h_{max} = 123,047,496$, so the number of half-spaces in this problem is an order of magnitude below the upper bound for both target configurations.

Once the normal vectors of the H-representation are computed, the Chebyshev center linear program is solved to compute the optimal spring parameters. The linear program of Eq. (5.23) has 145 variables and 16,536,777 inequality constraints. The MOSEK solver [106] was used to compute a solution.

The resulting spring parameters corresponding to the Chebyshev center solution are plotted in Figure 5.5. The rest angles corresponding to springs with zero stiffness were set to zero for the sake of plotting. The corresponding Chebyshev radius is $r_c = 6.39\kappa_{max}$, which has units of Newtons if κ_{max} is specified in Nm/rad. This brings the guarantee that any force of magnitude less than r_c can be applied to the spherical or flat configuration without causing any displacements. This lower bound is especially powerful for complex structures such as this since it offers a single number that exactly quantifies the load-bearing capacity in the worst case loading direction. For reference, if a maximum stiffness of 0.230 Nm/rad is considered, corresponding to the torsion springs used in Chapter 6, the resulting Chebyshev radius is 1.47 N.

The Chebyshev radius provides a lower bound on the critical perturbation force; in most loading directions, the critical force is higher. Two loading directions are considered to demonstrate this. For a load applied upward to one of the corner vertices of the pattern, depicted in Figure 5.6, the critical force is $P^* = 31.6\kappa_{max}$ in

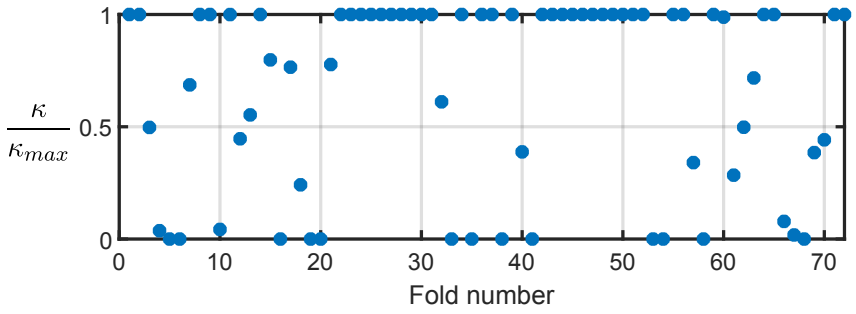

(a)

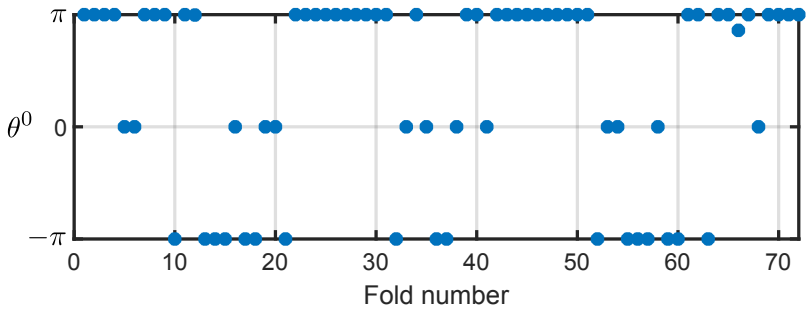

(b)

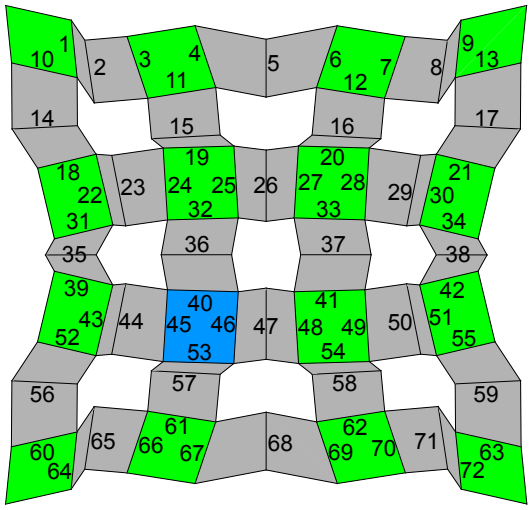

(c)

Figure 5.5: Chebyshev center solution. (a) Torsion spring stiffness values. (b) Torsion spring rest angles. (c) Fold numbering scheme, shown in the top view of the saddle configuration. The blue tile is fixed to remove rigid body motion.

the spherical configuration and $P^* = 33.2\kappa_{max}$ in the saddle configuration, which take units of Newtons if κ_{max} is specified in Nm/rad. This value can be computed by either Eq. (5.17) using the V-representation or Eq. (5.19) using the H-representation, both giving the same result.

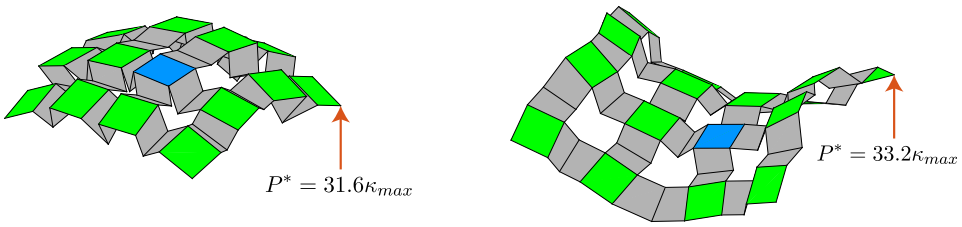

(a) (b)

Figure 5.6: Two load cases and their corresponding critical forces for the 18-DOF square tile pattern. (a) Spherical configuration. (b) Flat configuration.

5.6 Outlook for larger problems

While we have demonstrated the multi-configuration rigidity design process on an 18-DOF structure, there are possible computational limitations when considering even larger problems. It would certainly be feasible to solve problems at a larger scale, considering that the facet enumeration problem for the 18-DOF example was solved on a laptop without parallelization. The LRS algorithm for facet enumeration has demonstrated near linear speedups with parallelization on up to 1200 cores [107], leaving room for larger problems to be solved.

However, the combinatorial nature of polyhedral cones will eventually provide limits on what can practically be solved. This becomes evident by computing the upper bound on the number of half-spaces in the H-representation for the 84-DOF morphing surface pattern of Section 3.7.3. If unilateral constraints were placed on all 162 folds of the pattern, the upper bound for $n_a = 162$ and $m = 84$ is on the order of $h_{max} \approx 10^{32}$. Though the number of facets could be much lower, it requires solving the facet enumeration problem to find out. Methods have been developed to provide estimates for the number of facets without solving the full problem [108], which could be useful when approaching large problems. Of course, the number of unilateral constraints could be reduced to decrease the size of the computation, but this could decrease the load-bearing capacity. For discussion on the performance of facet enumeration algorithms, see [107, 109].

5.7 Conclusion

This chapter has extended theoretical formulations and design methodology for multi-configuration rigidity to accommodate statically indeterminate unilateral constraints. There are two equivalent representations for equilibrium with unilateral constraints, which represent a polyhedral cone. The V-representation can be di-

rectly computed from the constraint gradients, while the H-representation is useful for computing the lower bound on critical forces. The Chebyshev center spring design problem, which maximizes this lower bound in a set of target configurations, relies on the H-representation, and facet enumeration must be performed to convert between representations. Furthermore, it was demonstrated that placement of as many unilateral constraints as possible is advantageous for the sake of increasing the load bearing capacity of rigid configurations.

By accommodating for static indeterminacy, structures with many degrees of freedom and unilateral constraints can be considered. This is demonstrated through the design of an 18-DOF kirigami surface to have rigid spherical and saddle configurations. The resulting Chebyshev center design comes with the guarantee that any load smaller than the Chebyshev radius applied to either target configuration can be rigidly resisted. Furthermore, since the Chebyshev center design problem is cast as a linear program, it brings guarantees of optimality. Through this example, we show that multi-configuration rigidity is a practical tool for achieving load-bearing capacity in structures with high kinematic freedom, providing a path for using the kirigami surfaces synthesized in Chapter 3 as practical engineering structures.

Chapter 6

EXPERIMENTS AND UNCERTAINTY ANALYSIS OF A LINKAGE

6.1 Introduction

The concept of multi-configuration rigidity offers a promising path for designing structures to be both reconfigurable and capable of bearing loads. However, it is a mathematical concept that relies on the assumptions of rigid-body kinematics. It is crucial to understand how the concept of multi-configuration rigidity translates to physical structures and if the analytical critical force predictions, which assume all components of a structure are perfectly rigid, are valid for a physical structure. In reality, any physical structure is made of compliant elements. Furthermore, geometric imperfections and deviations from ideal spring parameters are unavoidable, motivating experimental study to validate theoretical predictions and quantify sensitivity to uncertainty.

Understanding the role of imperfections and uncertainty is an essential step towards engineering applications of reconfigurable structures. Tremendous efforts are made to characterize uncertainty of traditional engineering structures. As we develop the concept of multi-configuration rigidity, it is critical to explore the role of imperfections and uncertainty. Previous research has investigated imperfections in various types of discrete structures, including linkages [110–112], origami [113], and tensegrity structures [114]. These studies highlight the importance and potentially high impact of small imperfections on structural properties.

In this chapter, a prototype of the 2-DOF linkage from Chapter 4 is constructed and quantitatively studied. Probing experiments are performed, where the force-displacement curve is measured as a load is applied to a rigid configuration of the structure. These experiments demonstrate how multi-configuration rigidity translates to physical structures where no components can be perfectly rigid, as well as the sensitivity to imperfections. To obtain quantitative agreement with analytical predictions, geometric imperfections and spring parameters must be carefully characterized, highlighting the sensitivity to small parameter variations. To understand this sensitivity, an Monte Carlo analysis is performed to analyze the predicted critical reaction forces in the context of uncertain geometric and spring parameters.

This chapter provides an experimental grounding for the theoretical concepts of multi-configuration rigidity and constitutes a step towards practical application.

6.2 Prototype

To demonstrate the concept of multi-configuration rigidity in a physical structure, a prototype of the 2-DOF linkage was constructed. In Figure 6.1, the prototype is shown in each of the four rigid target configurations.

The bars of the linkage are constructed from 2.38 mm thick steel plates joined by steel pin hinges. Hinges 1 and 5 are connected to rectangular aluminum columns, which are mounted to a base plate. Two identical angle stops are placed on hinges 1 and 5, one on the top and one on the bottom of each hinge. The angle stops, which are made of aluminum cut by CNC mill, are mounted on the pins of hinges 1 and 5. Hinges 1 and 5 are free to rotate within the range of 0 and $\pi/4$ radians, but come into contact with the stops at 0 and $\pi/4$. The top angle stop on hinge 5 is shown from the top view at its limits in Figures 6.2a and 6.2b. The segments of the angle stops that make contact with the plate and mounting column are rounded. By rounding the edge of the angle stops, there is a well-defined line of contact between the stop and the plate/column. This is the result of an iterative design process; it was found in early design iterations of the angle stops that having a plane of contact between the stop and the plate/column was highly sensitive to misalignment. To accommodate the small hinge angles in configurations 3 and 4, hinges 2 and 4 were split in half to avoid self contact, which can be seen in Figure 6.1.

Hinges 2, 3, and 4 each have two identical torsion coil springs mounted around their pins. Each spring has a nominal stiffness of 0.115 Nm/rad and a rest angle of π. Thus, the spring parameters of the prototype are $\kappa_2 = \kappa_3 = \kappa_4 = 0.230$ Nm/rad and $\theta_2^0 = \theta_3^0 = \theta_4^0 = \pi$. This choice of spring parameters is guided by the Chebyshev center solution of Eq. (4.61), but the stiffness of hinges 2 and 4 is rounded up to $\kappa_{max} = 0.230$ Nm/rad so that identical springs can be used on each hinge. These spring parameters satisfy the rigidity conditions in all four target configurations, but are easier to physically implement than the exact Chebyshev center. A closeup photo of hinge 3 is shown in Figure 6.2c, which shows the springs mounted on the hinge. 3D printed mounting blocks (white) align and guide the legs of the springs as the hinge folds.

Qualitatively, the prototype behaves as expected; contact is maintained in all four target configurations to hold the structure in place. The following sections develop

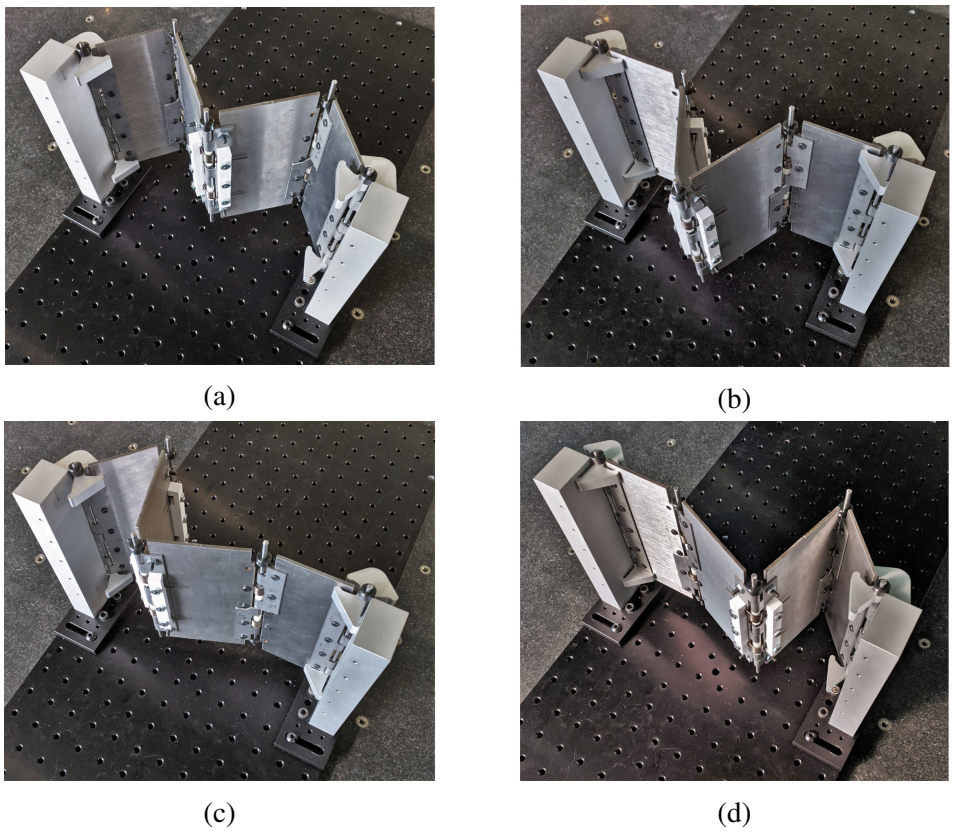

(a) (b)

(c) (d)

Figure 6.1: Prototype of the 2-DOF linkage. Target configurations 1 to 4 are shown in (a) to (d), from a perspective view.

quantitative experimental studies to characterize the behavior of the structure and compare to theoretical predictions.

6.3 Load cases

To quantitatively study the prototype, loads are applied to the structure as a means for comparison between experiment and theory. We focus our attention to configurations 1 and 2 and define a perturbation load case for each configuration. In configuration 1, a force is applied in the $-y$ direction on hinge 3, which corresponds to the perturbation direction $\boldsymbol{f}_p = [0, 0, 0, -1, 0, 0]^T$. The second load case is a force in the $+y$ direction on hinge 3 in target configuration 2, which corresponds to the perturbation direction $\boldsymbol{f}_p = [0, 0, 0, 1, 0, 0]^T$. The critical forces in each test case are denoted $P^*_{3y}|_1$ and $P^*_{3y}|_2$, respectively. The two load cases are illustrated in Figure 6.3. These perturbation force directions are chosen since they are straightforward to implement experimentally.

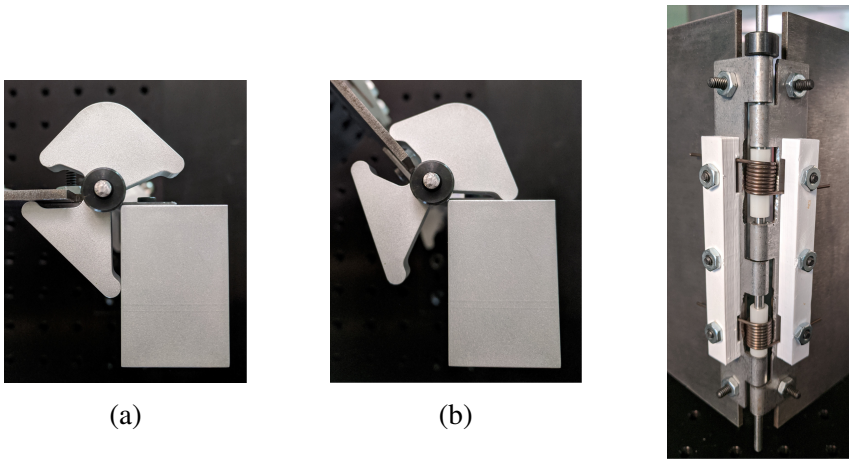

(a) (b) (c)

Figure 6.2: Components of the linkage prototype. (a) Top view of the angle stop on hinge 5 at $\theta_5 = 0$. (b) Top view of the angle stop on hinge 5 at $\theta_5 = \pi/4$. (c) Closeup of hinge 3 in configuration 1.

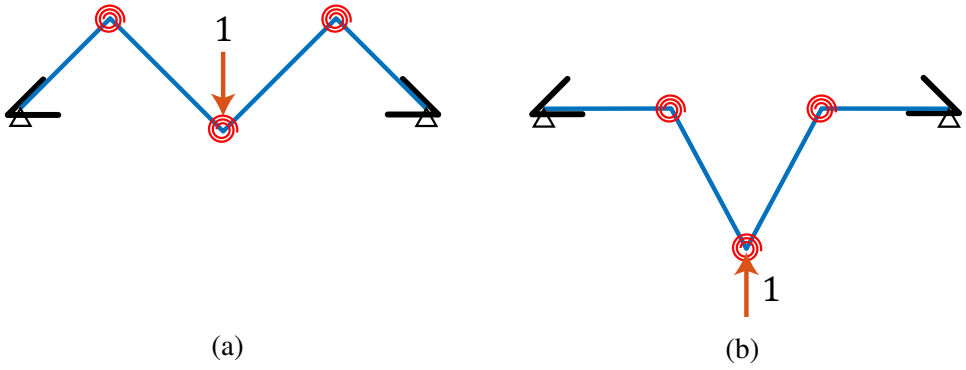

(a) (b)

Figure 6.3: Perturbation load cases. (a) Probing hinge 3 in the $-y$ in configuration 1. (b) Probing hinge 3 in the $+y$ direction in configuration 2.

Assuming ideal geometry in each configuration and nominal spring parameters of $\kappa = 0.230$ Nm/rad and $\theta^0 = \pi$, predictions for the critical forces can be computed by solving the linear program of Eq. (4.28). The resulting predictions are $P_{3y}|_1 = 4.09$ N and $P_{3y}|_2 = 6.61$ N. However, these critical forces are sensitive to geometric imperfections and variations in spring parameters, which are investigated in the following sections. Section 6.4 presents a detailed experimental characterization of the actual geometry and spring parameters of the prototype linkage. This characterization is used to update the analytical predictions, which is necessary to achieve agreement with the experiments of Section 6.5.

6.4 Experimental characterization

The linkage prototype inherently exhibits variations from the intended design parameters. For this structure, the geometric parameters (bar lengths and stop angles) along with the spring parameters (stiffnesses and rest angles) are of interest. We aim to understand the affect of variations in these parameters on the load-bearing capacity of the structure. To do so, the geometry and spring parameters are characterized experimentally. Based on the measured parameters, the analytical prediction for critical perturbation forces is updated to reflect the actual parameters of the structure.

There are several factors that lead to variations from ideal parameters in the prototype. Regarding the geometric parameters, the primary sources of imperfection are machine tolerances of components, clearance in the pin hinges, and misalignment in the bolts that fasten the plates to the hinges. Regarding the spring parameters, stock torsion springs are used that exhibit variations in stiffness and rest angle from the manufacturing process. Furthermore, misalignment in mounting of the springs on the hinges influences the effective stiffnesses and rest angles of the hinges.

6.4.1 Geometry measurement

To characterize the geometry of the prototype, both target configurations were scanned with a non-contact laser scanner (FaroArm Edge 14000 with the ScanArm HD attachment), producing a point cloud measurement of both configurations. The point cloud data was processed to compute vertex positions by computing the center point of each pin, allowing bar lengths to be computed. Additionally, planes were fit to each plate allowing hinge angles to be computed. From these planes, it was also determined that all of the plates are at most 0.18° from vertical. This indicates that out-of-plane effects are negligible and the prototype is effectively modeled with two-dimensional geometry.

The measured two-dimensional geometry of each configuration is plotted alongside the ideal geometry in Figure 6.4. Measured lengths and angles are listed in Table 6.1. The bar length measurements were all within 1 mm of their ideal values while the angle measurements had deviations up to 0.085 radians (4.85°). These deviations in stop angle reflect the sensitivity of angles to small misalignments, tolerances, and clearance in the pin-hinges. The stop angles are sensitive to these imperfections since the contact between the angle stops and the plates is relatively close to the axis of rotation of the hinge.

Table 6.1: Measured versus ideal geometric parameters

	Configuration 1		Configuration 2	
	Ideal	Measured	Ideal	Measured
L_1 (mm)	75	75.06	75	75.37
L_2 (mm)	94.5	94.49	94.5	94.02
L_3 (mm)	94.5	94.69	94.5	94.41
L_4 (mm)	75	75.99	75	74.80
L_5 (mm)	238.64	239.18	238.64	238.59
θ_1 (rad)	$\pi/4$	0.87	0	0.003
θ_5 (rad)	$\pi/4$	0.85	0	-0.023

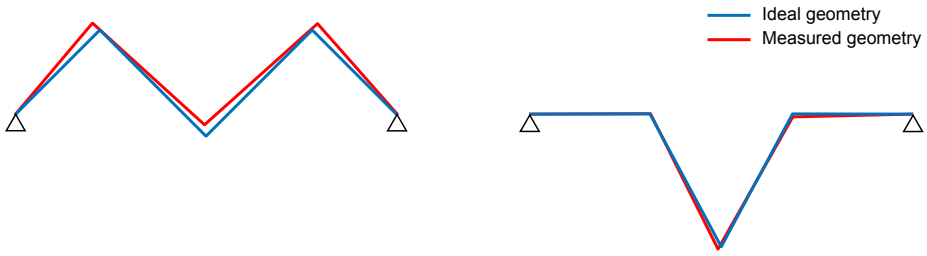

(a) (b)

Figure 6.4: Comparison of ideal linkage geometry to the measured geometry of the prototype for (a) target configuration 1 and (b) target configuration 2.

6.4.2 Spring parameter measurement

Along with deviations in geometric parameters, there are also deviations in the spring parameters. Stock torsion springs were used, with a nominal stiffness of 0.115 Nm/rad and rest angle of π radians, though the actual spring parameters deviate from their nominal values.

The moment-angle response of each spring was measured on the bending test machine shown in Figure 6.5a. Each of the six springs were characterized individually. To characterize a spring, the spring was mounted on a hinge connecting two plates. The spring mounting scheme is identical to the prototype mounting scheme, where a 3D printed mounting block, shown in white, guides the legs of the spring as the hinge folds. The plates on each side of the hinge were mounted to the test machine to measure the moment-angle relationship. Each plate was mounted above a hollow shaft outfitted with strain gauges connected to a Vishay P3 strain amplifier. The strain in each shaft was calibrated to an equivalent moment. One end of the test machine is fixed while the other is free to translate, as shown in Figure 6.5a. A rotation can be applied to each end by a gear and worm screw assembly. A rela-

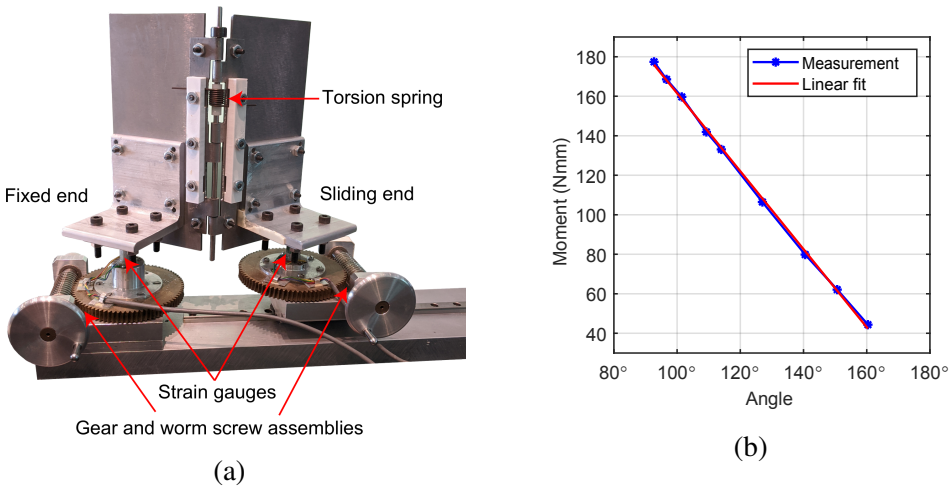

Figure 6.5: Experimental characterization of springs. (a) Experimental setup for moment-angle measurements. (b) Example of a moment-angle measurement for the top spring of hinge 2.

tive rotation was applied to the two plates such that the two shafts see equivalent moments indicating that a pure moment was applied to the hinge. As the relative rotation was incrementally increased, the moment-angle response of the hinge was measured.

One example of a measured moment-angle response is shown in Figure 6.5b corresponding to the top spring of hinge 2. As observed in the plot, the response is well captured by a linear fit, which is used to compute stiffness and rest angle values. The measured stiffness and rest angle values for all six springs are listed in Table 6.2. Note that two springs (referred to as top and bottom) are embedded on hinges 2, 3, and 4.

Table 6.2: Measured spring parameters

	Stiffness (Nm/rad)	Rest angle
Hinge 2 top	0.119	181°
Hinge 2 bottom	0.120	179°
Hinge 3 top	0.149	152°
Hinge 3 bottom	0.159	148°
Hinge 4 top	0.142	175°
Hinge 4 bottom	0.133	188°

6.4.3 Updated critical force predictions

Predictions for the critical forces $P^*_{3y}|_1$ and $P^*_{3y}|_2$ are computed to reflect the measured geometry and spring parameters of the prototype. To do so, the linearized

kinematics are computed about the measured target configurations, using the measured vertex positions, bar lengths, and stop angles. These computations follow the procedure of Appendix C, but using the measured instead of the ideal parameters. Updated predictions for critical forces are computed using the linear program of Eq. (4.28). The updated predictions are $P^*_{3y}|_1 = 3.01$ N and $P^*_{3y}|_2 = 5.65$ N.

6.5 Probing experiments

In this section, a set of experiments are presented where the prototype structure is loaded according to the two load cases of Figure 6.3 and the force-displacement response is measured as the structure is loaded. This provides a means for comparison and validation of analytical predictions for the critical forces.

The setup for the probing experiments is shown in Figure 6.6 in the two loading configurations. A linear actuator (Progressive Automations PA-14P) is used to probe the structure by applying a y-direction displacement to the pin of hinge 3. A force sensor (ATI Industrial Automation Nano17) is mounted to the linear actuator to measure the force applied to the structure as the actuator moves. A 3D printed probing tip is mounted to the force sensor, which makes contact with the pin of hinge 3. In configuration 1, a narrow probing tip was used, shown in red in Figure 6.6a. In configuration 2, a wider probing tip was used to accommodate a small amount of horizontal motion of the pin as the structure moves.

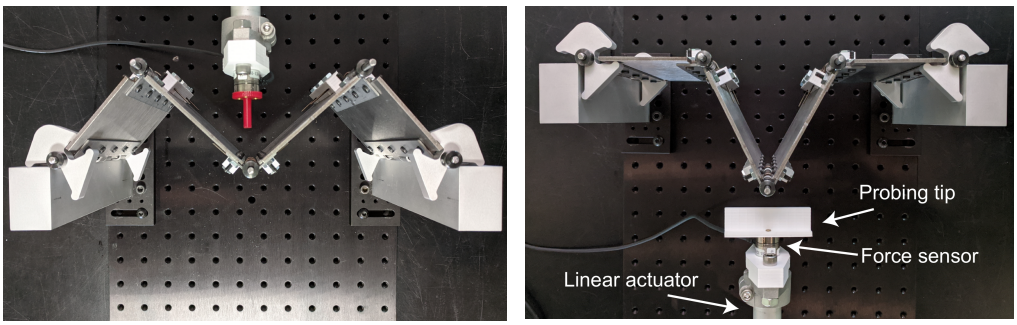

(a) (b)

Figure 6.6: Probing experiment setup, where a force sensor is attached to a linear actuator to measure a force-displacement curve along a perturbation direction. (a) Probing vertex 3 in the $-y$ direction in configuration 1. (b) Probing vertex 3 in the $+y$ direction in configuration 2.

While we are particularly interested in the initial response in each load case, the actuator continuously applied a displacement beyond this initial response to clearly distinguish when contact with the stops is lost. That is, the actuator kept moving

until the probing force became zero and the structure dynamically transitioned to the other rigid configuration. The force displacement curve is plotted in Figure 6.7 for each load case. Five trials were performed for each load case. The average of the five trials is plotted in blue, along with the envelope of the trials in gray.

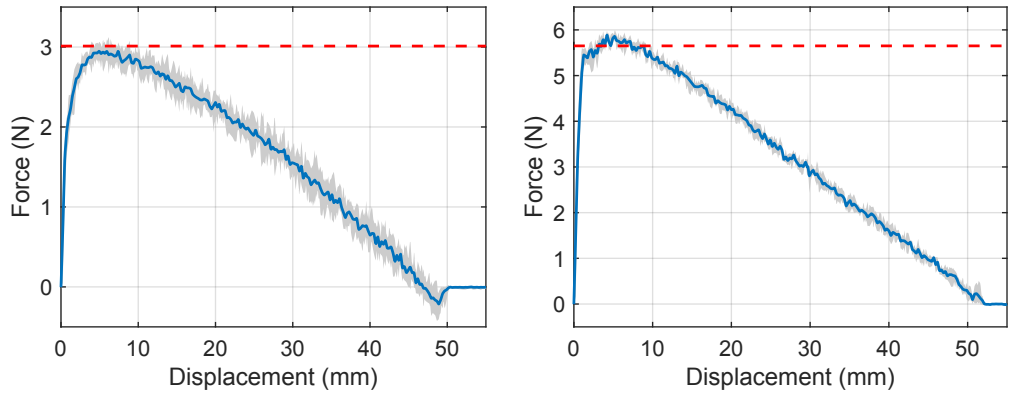

(a) (b)

Figure 6.7: Measured force-displacement curve for (a) load case 1 and (b) load case 2. The blue curve represents the mean of five measurements and the gray region is the envelope of the five measurements. The dashed red line is the analytical prediction of critical force for contact loss.

The force-displacement curve has a steep initial slope, which corresponds to the region where there is contact with the stops. Then, a maximum force is reached, where contact with the stops is lost. Beyond this point, the force decreases as the displacement increases. This is a displacement control experiment as long as the probing force is positive. Once the probing force becomes zero, contact between the probe and the hinge is lost and the structure dynamically transitions to the other rigid configuration. Note that the envelope of the force-displacement response over the five measurements is larger in load case 1 than in load case 2, though this is exaggerated in Figure 6.7 since the two plots are scaled differently.

The theoretical analysis of Chapter 4 assumes perfectly rigid bars and contact along with perfect pin-joint kinematics. Under these assumptions, the force-displacement curve is predicted to be initially vertical, until the critical force is reached and the structure begins to move. The analytical predictions for critical force (using the measured geometry and spring parameters) are plotted as dashed red lines in Figure 6.7. It is evident that the peak in the experimental force-displacement curve closely matches the analytical predictions. However, since the components of the prototype are not perfectly rigid, the configurations that are theoretically rigid manifest as

initially stiff. A contributing factor to the initial response is the imperfect contact between the angle stops and plates. There is a line of contact between the stop and the plate and contact may not instantaneously be lost; there may be a region of partial contact before the stop fully lifts off the plate. Furthermore, clearance in the pins of the hinges allows for some small movements of the prototype while maintaining contact with the stops.

Overall, these experiments validate that the modeling assumptions capture the load-bearing capacity of each target configuration. Despite the idealizations of the theoretical model, which assumes perfect pin-joint kinematics, rigid bars, and rigid stops, a meaningful prediction of the load-bearing capacity is achieved. However, mathematically initially rigid configurations manifest as initially stiff configurations due to the inherent compliance of the bars and stops along with clearance in the pin hinges. Furthermore, the detailed experimental characterization of Section 6.4 was necessary to obtain quantitative agreement between experiments and the analytical model.

6.6 Uncertainty analysis

The load bearing capacity of the prototype is sensitive to variations in the geometric and spring parameters. It is evident from the experimental characterization in Section 6.4 that there is uncertainty in these parameters, which influences the load bearing capacity of the prototype. This detailed experimental characterization was needed to achieve agreement between analytical and experimental critical force values. In this section, we investigate the influence of uncertainty on the critical forces for the two load cases. Specifically, we pose the following question: *if another prototype is constructed, what range of critical forces can be expected given uncertain geometric and spring parameters*? To answer this question, a Monte Carlo analysis is conducted, which quantifies sensitivity to parameter uncertainty.

The Monte Carlo analysis begins by sampling geometric and spring parameters from a distribution. Specifically, the bar lengths L_1, L_2, L_3, L_4, stop angles $\theta_1|_1$, $\theta_1|_2$, $\theta_5|_1$, $\theta_5|_2$, and spring parameters κ, θ^0 for all six springs are treated as uncertain. The experimental characterization of Section 6.4 provides a baseline for what ranges in parameters can be expected. Bar lengths within ± 1 mm of their ideal length and stop angles within $\pm 5^\circ$ of their ideal value are considered. A range of spring stiffnesses between 0.119 and 0.155 Nm/rad and rest angles between 148° and 188° are considered, which are the ranges of measured spring parameters in the prototype.

A more detailed uncertainty quantification procedure could produce tighter bounds on individual parameters, but this study adopts these reasonable bounds to highlight the influence of uncertainty.

For each realization in the Monte Carlo analysis, each parameter is sampled from a uniform distribution over the specified range. Based on the values of bar length and stop angles, vertex coordinates are computed for both target configurations. Constraint gradient matrices are then computed about this configuration, following the procedure of Appendix C but using the sampled parameters. Then, the linear program of Eq. (4.28) is evaluated for each load case to compute the critical forces.

An analysis of 50,000 realizations was performed. Histograms of the critical forces are plotted in Figure 6.8. The mean value of $P_{3y}|_1$ is 3.00 N with a standard deviation of 1.38 N. The mean value of $P_{3y}|_2$ is 3.91 N with a standard deviation of 2.00 N. Some realizations did not satisfy the rigidity conditions (equilibrium could not be satisfied with positive unilateral reactions). These realizations are omitted from the histograms leading to a sharp cutoff at a critical perturbation force of 0. In configurations 1 and 2, 1.74% and 2.33% of realizations did not satisfy the rigidity conditions.

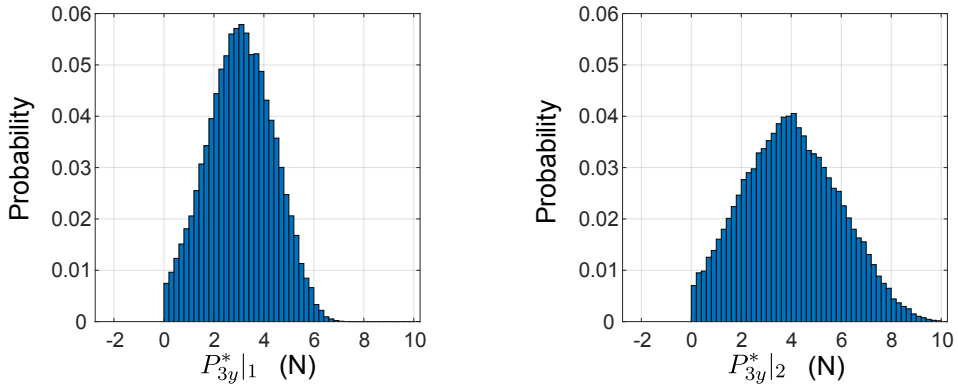

(a) (b)

Figure 6.8: Probability distributions of critical forces from a Monte Carlo analysis with 50,000 samples. (a) Critical force for load case 1. (b) Critical force for load case 2.

These results reflect a large variation in critical forces stemming from parameter uncertainty. Especially surprising is the result that a portion of the samples violated the rigidity conditions, suggesting that if another prototype was built, there is a chance that the target configurations are not all rigid configurations. This highlights

the need for understanding the role of parameter uncertainty, which can have large impact on the properties of a structure.

The large role of parameter uncertainty also emphasizes the value of the Chebyshev center design process. The Chebyshev center design represents the design with the largest load-bearing capacity. Variations from ideal spring parameters can be equivalently thought of as applying a perturbation load to a structure with ideal spring parameters. From this perspective, the Chebyshev center design is the most robust design to spring parameter uncertainty. However, robustness to geometric parameter uncertainty is not accounted for in the Chebyshev center design process and would be a useful path of future research.

6.7 Conclusion

This chapter presents experiments and an uncertainty analysis to investigate multi-configuration rigidity in the context of a physical structure. A set of experiments were performed where perturbation forces were applied to a 2-DOF linkage prototype. The probing experiments highlight that each mathematically rigid configuration has an initially stiff force-displacement response upon loading. However, the idealized theoretical model of the structure with rigid components and pin-joint kinematics produces accurate quantitative predictions for maximum load-bearing capacity of the target configurations, providing validation for the analytical predictions of critical forces.

To obtain agreement between the analytical predictions of the critical forces and the experiment, a detailed experimental characterization of the prototype was required, which involved measuring its spring parameters and geometry in each target configuration. This prompted further study of the influence parameter uncertainty on the critical forces in each configuration. A Monte Carlo analysis shed light on the large impact of parameter uncertainty on the load-bearing capacity of each configuration.

Chapter 7

CONCLUSIONS AND FUTURE WORK

7.1 Summary and main contributions

The research presented in this thesis provides a new framework for designing reconfigurable structures with many kinematic degrees of freedom. In the kirigami pattern synthesis process presented in Chapter 3, fold patterns capable of achieving several target surfaces are developed, highlighting the appeal of structures with many-DOF kinematics. To address the challenges associated with this high kinematic freedom, springs and unilateral constraints can be embedded to achieve initial rigidity in multiple target configurations. The geometry synthesis framework together with the multi-configuration rigidity design process provide a path to reconfigurable surfaces with load-bearing capacity in multiple configurations.

This proposed approach to reconfigurable structures advances the state-of-the-art by providing a systematic design process to achieve load-bearing configurations based on a quantitative metric, which is the lower bound on load-bearing capacity in each target configuration. Furthermore, the load-bearing capacity is experimentally verified on a prototype linkage structure, providing grounding for the design process in a physical structure. Finally, multi-configuration rigidity is appealing because it is scalable. The load-bearing capacity in a rigid configuration scales with the spring parameters. That is, larger load-bearing capacity can be achieved by considering stiffer springs, indicating that multi-configuration rigidity has potential for application at a range of scales. Collectively, this work provides a clear path to engineering structures with many kinematic degrees of freedom.

7.1.1 Geometry synthesis

In Chapter 3, a kirigami pattern synthesis framework was presented to generate fold patterns capable of achieving multiple curved surfaces. This represents a novel solution to an open problem of inverse design of a fold pattern that can achieve multiple target shapes.

Synthesis of this new family of kirigami patterns is framed as a tile arrangement problem. A constrained optimization problem is formulated to simultaneously arrange a set of tiles on multiple surfaces while enforcing compatibility between the

tile arrangements. Upon computing compatible tile arrangements that approximate each target surface, sub-folds are added to connect tiles in one arrangement, completing the fold pattern. The resulting fold patterns are capable of reconfiguring between all target surface tile arrangements. While these patterns are able to achieve multiple target surfaces with varying Gaussian curvature, in turn they exhibit many kinematic degrees of freedom.

The main contributions from this work are:

- A computational framework for inverse design of kirigami surfaces that can take on multiple target configurations.
- A prototype of a kirigami pattern that can take on six target surfaces, fabricated using 3D printed plates and pin hinges.

7.1.2 Multi-configuration rigidity

Chapters 4, 5, and 6 developed the concept of multi-configuration rigidity, where a reconfigurable structure is held rigidly by the prestress between embedded springs and unilateral constraints in multiple configurations. While the development of multi-configuration rigidity is specifically motivated by the many-DOF kirigami patterns of Chapter 3, theoretical formulations were presented from a general perspective.

Chapter 4 formulated a theory for multi-configuration rigidity in the case of statically determinate unilateral constraints. First, conditions were derived for rigidity of a single configuration due to a force applied to the structure that engages unilateral constraints. Rigidity can be achieved in multiple configurations if the force that engages the unilateral constraints is applied by embedded springs. This leads to a design problem where the parameters of embedded springs are chosen to satisfy rigidity in multiple target configurations. The Chebyshev center solution to this design problem is the design that maximizes the lower bound on critical perturbation forces, effectively maximizing the load-bearing capacity in all target configurations.

Chapter 5 extended the rigidity conditions and the Chebyshev center design process to the statically indeterminate case when unilateral constraint reactions are not unique. To accommodate static indeterminacy, the geometric structure of the equilibrium conditions as a convex polyhedral cone was exploited. One extra step in the spring design process is required in the statically indeterminate case, which is the conversion of the vector representation of the equilibrium cone to the half-space

representation, which is required to formulate the Chebyshev center linear program. Static indeterminacy is beneficial from the perspective of load-bearing capacity; the presence of more unilateral constraints generally leads to a larger lower bound on critical perturbation forces. This allows for the design of multi-configuration rigidity in large, many-DOF structures with many unilateral constraints. An example was presented designing an 18-DOF kirigami surface, which was synthesized in Chapter 3, to satisfy rigidity in a spherical and saddle-shaped configuration.

Finally, Chapter 6 presented experiments on a prototype of a 2-DOF linkage. Experiments were conducted to measure critical perturbation forces for certain load cases. The critical forces to overcome contact closely match between experiment and analytical prediction. However, detailed experimental characterization of the prototype geometry and spring parameters was required to achieve agreement, suggesting that the load-bearing capacity is sensitive to parameter uncertainty. This sensitivity is quantified in a Monte Carlo analysis, highlighting the potentially large effect of parameter uncertainty on load-bearing capacity of rigid configurations.

Collectively, the research presented in Chapters 4, 5, and 6 developed the concept of multi-configuration through theoretical, computational, and experimental analysis. We showed that multi-configuration rigidity offers a means of achieving load-bearing capacity in multiple target configurations of a structure with high kinematic freedom, and a systematic design process was presented to maximize load-bearing capacity.

The main contributions regarding multi-configuration rigidity are:

- A theoretical framework for rigidity of a structure due to unilateral constraints and a force for both statically determinate and indeterminate cases. The lower bound on critical forces offers a general characterization of the load-bearing capacity of rigid configurations.
- A systematic spring design framework to achieve rigidity in multiple configurations that maximizes load-bearing capacity, which is ultimately demonstrated on an 18-DOF kirigami surface.
- Experimental validation of critical perturbation loads on a 2-DOF linkage prototype.

7.2 Future work

This thesis lays a foundation for multi-DOF reconfigurable structures to be applied as engineering structures. Proof-of-concept for the geometry synthesis and

multi-configuration rigidity framework is presented through a series of prototypes, highlighting the feasibility of the contributions of this thesis. Several directions of future research can extend the work of this thesis towards the development of practical engineering structures.

The proof-of-concept prototypes presented in Chapters 2, 3, and 6 provide insights into realization of multi-configuration rigidity that can guide future work. The theory of multi-configuration rigidity relies on assumptions of perfect plate-hinge or pin-joint kinematics along with rigid unilateral constraints and rigid plates or bars. In Chapter 2, the prototype exhibited compliant hinges with undesirable deformation modes and the unilateral constraints had substantial compliance, which led to error in the shapes of the target configurations. In contrast, the linkage prototype of Chapter 6 exhibited stiff plates and contacts along with well-defined pin hinges, leading to a prototype whose load-bearing capacity quantitatively agrees with theoretical predictions.

Future prototypes of reconfigurable surfaces should focus on achieving clean kinematics and stiff components, which would lead to predictable target configurations and load-bearing capacity. Based on the prototyping insights developed throughout this work, a promising approach in future work is to further develop the concept of 3D printed plates with pin hinges presented in Chapter 3. The pin hinges are well-defined hinges that offer clean folding kinematics. Stiff materials could be used for the plates, which could range from hard plastics to metals depending on the scale of interest. One appeal of 3D printing is that angle stops could be directly printed into the plates, allowing for custom stop angles to be achieved in an integrated design. Springs could then be embedded in the structure, either as coil torsion springs mounted on the hinges or as elastic extensional springs placed throughout the structure. To increase load-bearing capacity, stiff springs could be used; practical limitations on spring stiffness would be useful to develop. While very stiff springs could be beneficial to achieve high load-bearing capacity, at a certain scale the large internal forces associated with stiff springs would be a limitation.

In addition to further developing prototyping concepts, future work on theoretical and computational aspects of geometry synthesis and multi-configuration rigidity can advance these concepts towards practical applications. Building from the geometry synthesis contributions of the thesis, one direction of future work is to further explore the design space. Relaxing tile shape constraints to allow, for example, non-equilateral triangular tiles could increase the freedom in the design problem

and enable new solutions. Furthermore, exploring the range of curvatures that can be achieved with a single fold pattern could give insights into the range of target surfaces that can be achieved.

Regarding multi-configuration rigidity, research on actuation and pathfinding is a natural next step. Actuation schemes between rigid configurations could be designed with the goal of achieving simplified actuation using fewer actuators than kinematic degrees of freedom since the energy in the springs provides a guide between rigid configurations.

Additionally, further exploring the spring and unilateral constraint design space would be a valuable extension of this work. Systematic unilateral constraint placement schemes that account for more than two target configurations poses a challenge that would be useful to address. Combining multi-stability and multi-configuration rigidity could be an effective approach for achieving several target configurations in complex structures, where target configurations could exhibit a mixture of smooth energy minima and boundary minima.

BIBLIOGRAPHY

[1] S. Barbarino, O. Bilgen, R. M. Ajaj, M. I. Friswell, and D. J. Inman, "A review of morphing aircraft," *Journal of Intelligent Material Systems and Structures*, vol. 22, no. 9, pp. 823–877, 2011.

[2] J. Sun, Q. Guan, Y. Liu, and J. Leng, "Morphing aircraft based on smart materials and structures: A state-of-the-art review," *Journal of Intelligent Material Systems and Structures*, vol. 27, no. 17, pp. 2289–2312, 2016.

[3] F. Previtali, A. F. Arrieta, and P. Ermanni, "Performance of a three-dimensional morphing wing and comparison with a conventional wing," *AIAA Journal*, vol. 52, no. 10, pp. 2101–2113, 2014.

[4] A. Karanouh and E. Kerber, "Innovations in dynamic architecture," *Journal of Facade Design and Engineering*, vol. 3, no. 2, pp. 185–221, 2015.

[5] J. T. Karras, C. L. Fuller, K. C. Carpenter, A. Buscicchio, D. McKeeby, C. J. Norman, C. E. Parcheta, I. Davydychev, and R. S. Fearing, "Pop-up mars rover with textile-enhanced rigid-flex PCB body," in *2017 IEEE International Conference on Robotics and Automation (ICRA)*, IEEE, 2017, pp. 5459–5466.

[6] D.-Y. Lee, J.-K. Kim, C.-Y. Sohn, J.-M. Heo, and K.-J. Cho, "High–load capacity origami transformable wheel," *Science Robotics*, vol. 6, no. 53, 2021.

[7] K. Zhang, Y. H. Jung, S. Mikael, J.-H. Seo, M. Kim, H. Mi, H. Zhou, Z. Xia, W. Zhou, S. Gong, *et al.*, "Origami silicon optoelectronics for hemispherical electronic eye systems," *Nature Communications*, vol. 8, no. 1, pp. 1–8, 2017.

[8] B. Wang, "Kirigami electronic eye for shape-adaptive imaging," *Matter*, vol. 4, no. 8, pp. 2653–2655, 2021.

[9] X. Liu, S. Yao, B. S. Cook, M. M. Tentzeris, and S. V. Georgakopoulos, "An origami reconfigurable axial-mode bifilar helical antenna," *IEEE Transactions on Antennas and Propagation*, vol. 63, no. 12, pp. 5897–5903, 2015.

[10] D. M. Elzey, A. Y. N. Sofla, and H. N. Wadley, "A bio-inspired high-authority actuator for shape morphing structures," in *Smart Structures and Materials 2003: Active Materials: Behavior and Mechanics*, International Society for Optics and Photonics, vol. 5053, 2003, pp. 92–100.

[11] S. Neuhaeuser, M. Weickgenannt, C. Witte, W. Haase, O. Sawodny, and W. Sobek, "Stuttgart smartshell–a full scale prototype of an adaptive shell structure," *Journal of the International Association for Shell and Spatial Structures*, vol. 54, no. 4, pp. 259–270, 2013.

[12] F. Connolly, C. J. Walsh, and K. Bertoldi, "Automatic design of fiber-reinforced soft actuators for trajectory matching," *Proceedings of the National Academy of Sciences*, vol. 114, no. 1, pp. 51–56, 2017.

[13] K. Miura, H. Furuya, and K. Suzuki, "Variable geometry truss and its application to deployable truss and space crane arm," *Acta Astronautica*, vol. 12, no. 7-8, pp. 599–607, 1985.

[14] G. Senatore, P. Duffour, P. Winslow, and C. Wise, "Shape control and whole-life energy assessment of an 'infinitely stiff' prototype adaptive structure," *Smart Materials and Structures*, vol. 27, no. 1, p. 015 022, 2017.

[15] T. Tachi, "Geometric considerations for the design of rigid origami structures," in *Proceedings of the International Association for Shell and Spatial Structures (IASS) Symposium*, Elsevier Ltd, vol. 12, 2010, pp. 458–460.

[16] E. A. P. Hernandez, D. J. Hartl, E. Akleman, and D. C. Lagoudas, "Modeling and analysis of origami structures with smooth folds," *Computer-Aided Design*, vol. 78, pp. 93–106, 2016.

[17] Y. Kim, H. Yuk, R. Zhao, S. A. Chester, and X. Zhao, "Printing ferromagnetic domains for untethered fast-transforming soft materials," *Nature*, vol. 558, no. 7709, pp. 274–279, 2018.

[18] N. S. Usevitch, Z. M. Hammond, M. Schwager, A. M. Okamura, E. W. Hawkes, and S. Follmer, "An untethered isoperimetric soft robot," *Science Robotics*, vol. 5, no. 40, 2020.

[19] D. E. Williams, C. Dorn, S. Pellegrino, and A. Hajimiri, "Origami-inspired shape-changing phased array," in *2020 50th European Microwave Conference (EuMC)*, IEEE, 2021, pp. 344–347.

[20] Y. Klein, E. Efrati, and E. Sharon, "Shaping of elastic sheets by prescription of non-euclidean metrics," *Science*, vol. 315, no. 5815, pp. 1116–1120, 2007.

[21] Y. M. Song, Y. Xie, V. Malyarchuk, J. Xiao, I. Jung, K.-J. Choi, Z. Liu, H. Park, C. Lu, R.-H. Kim, *et al.*, "Digital cameras with designs inspired by the arthropod eye," *Nature*, vol. 497, no. 7447, pp. 95–99, 2013.

[22] K. Liu, F. Hacker, and C. Daraio, "Robotic surfaces with reversible, spatiotemporal control for shape morphing and object manipulation," *Science Robotics*, vol. 6, no. 53, Art–No, 2021.

[23] J. Panetta, M. Konaković-Luković, F. Isvoranu, E. Bouleau, and M. Pauly, "X-shells: A new class of deployable beam structures," *ACM Transactions on Graphics (TOG)*, vol. 38, no. 4, pp. 1–15, 2019.

[24] J. W. Boley, W. M. van Rees, C. Lissandrello, M. N. Horenstein, R. L. Truby, A. Kotikian, J. A. Lewis, and L. Mahadevan, "Shape-shifting structured lattices via multimaterial 4d printing," *Proceedings of the National Academy of Sciences*, vol. 116, no. 42, pp. 20 856–20 862, 2019.

[25] C. Baek, A. O. Sageman-Furnas, M. K. Jawed, and P. M. Reis, "Form finding in elastic gridshells," *Proceedings of the National Academy of Sciences*, vol. 115, no. 1, pp. 75–80, 2018.

[26] M. Konaković, K. Crane, B. Deng, S. Bouaziz, D. Piker, and M. Pauly, "Beyond developable: Computational design and fabrication with auxetic materials," *ACM Transactions on Graphics (TOG)*, vol. 35, no. 4, pp. 1–11, 2016.

[27] T. Chen, J. Panetta, M. Schnaubelt, and M. Pauly, "Bistable auxetic surface structures," *ACM Transactions on Graphics (TOG)*, vol. 40, no. 4, pp. 1–9, 2021.

[28] P. Celli, C. McMahan, B. Ramirez, A. Bauhofer, C. Naify, D. Hofmann, B. Audoly, and C. Daraio, "Shape-morphing architected sheets with non-periodic cut patterns," *Soft Matter*, vol. 14, no. 48, pp. 9744–9749, 2018.

[29] T. Chen and K. Shea, "Computational design of multi-stable, reconfigurable surfaces," *Materials & Design*, vol. 205, p. 109 688, 2021.

[30] Y. Li, A. Chandra, C. J. Dorn, and R. J. Lang, "Reconfigurable surfaces employing linear-rotational and bistable-translational (lrbt) joints," *International Journal of Solids and Structures*, vol. 207, pp. 22–41, 2020.

[31] T. Tachi, "Designing freeform origami tessellations by generalizing resch's patterns," *Journal of Mechanical Design*, vol. 135, no. 11, 2013.

[32] S. J. Callens and A. A. Zadpoor, "From flat sheets to curved geometries: Origami and kirigami approaches," *Materials Today*, vol. 21, no. 3, pp. 241–264, 2018.

[33] K. Miura and R. J. Lang, "The science of miura-ori: A review," *Origami*, vol. 4, pp. 87–99, 2009.

[34] P. Dieleman, N. Vasmel, S. Waitukaitis, and M. van Hecke, "Jigsaw puzzle design of pluripotent origami," *Nature Physics*, vol. 16, no. 1, pp. 63–68, 2020.

[35] S. A. Zirbel, R. J. Lang, M. W. Thomson, D. A. Sigel, P. E. Walkemeyer, B. P. Trease, S. P. Magleby, and L. L. Howell, "Accommodating thickness in origami-based deployable arrays," *Journal of Mechanical Design*, vol. 135, no. 11, 2013.

[36] T. Tachi, "Generalization of rigid-foldable quadrilateral-mesh origami," *Journal of the International Association for Shell and Spatial Structures*, vol. 50, no. 3, pp. 173–179, 2009.

[37] L. H. Dudte, E. Vouga, T. Tachi, and L. Mahadevan, "Programming curvature using origami tessellations," *Nature Materials*, vol. 15, no. 5, pp. 583–588, 2016.

[38] X. Dang, F. Feng, P. Plucinsky, R. D. James, H. Duan, and J. Wang, "Inverse design of deployable origami structures that approximate a general surface," *International Journal of Solids and Structures*, 2021.

[39] R. D. Resch, *Self-supporting structural unit having a series of repetitious geometrical modules*, US Patent 3,407,558, 1968.

[40] R. D. Resch, "The topological design of sculptural and architectural systems," in *Proceedings of the June 4-8, 1973, National Computer Conference and Exposition*, 1973, pp. 643–650.

[41] T. Tachi, "Origamizing polyhedral surfaces," *IEEE Transactions on Visualization and Computer Graphics*, vol. 16, no. 2, pp. 298–311, 2009.

[42] E. Peraza Hernandez, D. Hartl, and D. Lagoudas, "Design and simulation of origami structures with smooth folds," *Proceedings of the Royal Society A: Mathematical, Physical and Engineering Sciences*, vol. 473, no. 2200, 2017.

[43] D. J. Balkcom and M. T. Mason, "Robotic origami folding," *The International Journal of Robotics Research*, vol. 27, no. 5, pp. 613–627, 2008.

[44] S. Jape, M. Garza, J. Ruff, F. Espinal, D. Sessions, G. Huff, D. C. Lagoudas, E. A. P. Hernandez, and D. J. Hartl, "Self-foldable origami reflector antenna enabled by shape memory polymer actuation," *Smart Materials and Structures*, vol. 29, no. 11, p. 115 011, 2020.

[45] Y. Zhu, M. Birla, K. R. Oldham, and E. T. Filipov, "Elastically and plastically foldable electrothermal micro-origami for controllable and rapid shape morphing," *Advanced Functional Materials*, vol. 30, no. 40, p. 2 003 741, 2020.

[46] E. Hawkes, B. An, N. M. Benbernou, H. Tanaka, S. Kim, E. D. Demaine, D. Rus, and R. J. Wood, "Programmable matter by folding," *Proceedings of the National Academy of Sciences*, vol. 107, no. 28, pp. 12 441–12 445, 2010.

[47] J.-H. Na, A. A. Evans, J. Bae, M. C. Chiappelli, C. D. Santangelo, R. J. Lang, T. C. Hull, and R. C. Hayward, "Programming reversibly self-folding origami with micropatterned photo-crosslinkable polymer trilayers," *Advanced Materials*, vol. 27, no. 1, pp. 79–85, 2015.

[48] Y. Li and S. Pellegrino, "A theory for the design of multi-stable morphing structures," *Journal of the Mechanics and Physics of Solids*, vol. 136, p. 103 772, 2020.

[49] C. Coulais, A. Sabbadini, F. Vink, and M. van Hecke, "Multi-step self-guided pathways for shape-changing metamaterials," *Nature*, vol. 561, no. 7724, pp. 512–515, 2018.

[50] A. Zareei, B. Deng, and K. Bertoldi, "Harnessing transition waves to realize deployable structures," *Proceedings of the National Academy of Sciences*, vol. 117, no. 8, pp. 4015–4020, 2020.

[51] R. Ghosh, H. Ebrahimi, and A. Vaziri, "Contact kinematics of biomimetic scales," *Applied Physics Letters*, vol. 105, no. 23, p. 233 701, 2014.

[52] J. K. Salisbury and B. Roth, "Kinematic and force analysis of articulated mechanical hands," *Journal of Mechanisms, Transmissions, Automation in Design*, vol. 105, no. 1, 1983.

[53] A. Bicchi, "On the closure properties of robotic grasping," *The International Journal of Robotics Research*, vol. 14, no. 4, pp. 319–334, 1995.

[54] J. C. Trinkle, "On the stability and instantaneous velocity of grasped frictionless objects," *IEEE Transactions on Robotics and Automation*, vol. 8, no. 5, pp. 560–572, 1992.

[55] J. M. McCarthy and G. S. Soh, *Geometric design of linkages*. Springer Science & Business Media, 2010, vol. 11.

[56] M. S. Bazaraa, H. D. Sherali, and C. M. Shetty, *Nonlinear programming: Theory and algorithms*. John Wiley & Sons, 2013.

[57] J. O. Jacobsen, G. Chen, L. L. Howell, and S. P. Magleby, "Lamina Emergent Torsional (LET) joint," *Mechanism and Machine Theory*, vol. 44, no. 11, pp. 2098–2109, 2009.

[58] I. L. Delimont, S. P. Magleby, and L. L. Howell, "Evaluating compliant hinge geometries for origami-inspired mechanisms," *Journal of Mechanisms and Robotics*, vol. 7, no. 1, 2015.

[59] X. Dang, F. Feng, P. Plucinsky, R. D. James, H. Duan, and J. Wang, "Inverse design of surfaces by deployable origami," *arXiv preprint arXiv:2008.02349*, 2020.

[60] R. J. Lang, "A computational algorithm for origami design," in *Proceedings of the Twelfth Annual Symposium on Computational Geometry*, 1996, pp. 98–105.

[61] F. Wang, X. Guo, J. Xu, Y. Zhang, and C. Chen, "Patterning curved three-dimensional structures with programmable kirigami designs," *Journal of Applied Mechanics*, vol. 84, no. 6, 2017.

[62] X. Liu, J. M. Gattas, and Y. Chen, "One-dof superimposed rigid origami with multiple states," *Scientific Reports*, vol. 6, no. 1, pp. 1–9, 2016.

[63] N. Benbernou, E. D. Demaine, M. L. Demaine, and A. Ovadya, "A universal crease pattern for folding orthogonal shapes," *arXiv preprint arXiv:0909.5388*, 2009.

[64] A. Ovadya, "Origami transformers: Folding orthogonal structures from universal hinge patterns," Ph.D. dissertation, Massachusetts Institute of Technology, 2010.

[65] D. M. Sussman, Y. Cho, T. Castle, X. Gong, E. Jung, S. Yang, and R. D. Kamien, "Algorithmic lattice kirigami: A route to pluripotent materials," *Proceedings of the National Academy of Sciences*, vol. 112, no. 24, pp. 7449–7453, 2015.

[66] B. G. Chen and C. D. Santangelo, "Branches of triangulated origami near the unfolded state," *Physical Review X*, vol. 8, no. 1, p. 011 034, 2018.

[67] D. Hilbert and S. Cohn-Vossen, *Geometry and the Imagination*, 87. American Mathematical Soc., 1999.

[68] A. I. Bobenko, J. M. Sullivan, P. Schröder, and G. Ziegler, *Discrete differential geometry*. Springer, 2008, vol. 38.

[69] R. J. Lang, *Twists, tilings, and tessellations: Mathematical methods for geometric origami*. CRC Press, 2017.

[70] K. Crane, F. De Goes, M. Desbrun, and P. Schröder, "Digital geometry processing with discrete exterior calculus," in *ACM SIGGRAPH 2013 Courses*, 2013, pp. 1–126.

[71] R. Connelly, "Rigidity," in *Handbook of convex geometry*, Elsevier, 1993, pp. 223–271.

[72] R. Connelly and W. Whiteley, "Second-order rigidity and prestress stability for tensegrity frameworks," *SIAM Journal on Discrete Mathematics*, vol. 9, no. 3, pp. 453–491, 1996.

[73] B. Roth and W. Whiteley, "Tensegrity frameworks," *Transactions of the American Mathematical Society*, vol. 265, no. 2, pp. 419–446, 1981.

[74] C. R. Calladine, "Buckminster fuller's "tensegrity" structures and clerk maxwell's rules for the construction of stiff frames," *International Journal of Solids and Structures*, vol. 14, no. 2, pp. 161–172, 1978.

[75] R. Connelly, E. D. Demaine, and G. Rote, "Infinitesimally locked self-touching linkages with applications to locked trees," *Contemporary Mathematics*, vol. 304, pp. 287–312, 2002.

[76] A. Charnley, C. Lemke, and O. C. Zienkiewicz, "Virtual work, linear programming and plastic limit analysis," *Proceedings of the Royal Society of London. Series A. Mathematical and Physical Sciences*, vol. 251, no. 1264, pp. 110–116, 1959.

[77] K. Miura and S. Pellegrino, *Forms and Concepts for Lightweight Structures*. Cambridge University Press, 2020.

[78] S. Boyd and L. Vandenberghe, *Convex optimization*. Cambridge University Press, 2004.

[79] K. G. Murty, "Ball centers of special polytopes," *Department of Industrial ad Operations Engineering, University of Michigan*, 2009.

[80] G. C. Goodwin, H. Haimovich, D. E. Quevedo, and J. S. Welsh, "A moving horizon approach to networked control system design," *IEEE Transactions on Automatic Control*, vol. 49, no. 9, pp. 1427–1445, 2004.

[81] K. E. Lucas-Marcillo, D. A. P. Guingla, W. Barra, R. L. P. De Medeiros, E. M. Rocha, D. A. Vaca-Benavides, S. J. R. Orellana, and E. V. H. Muentes, "Novel robust methodology for controller design aiming to ensure DC microgrid stability under CPL power variation," *IEEE Access*, vol. 7, pp. 64 206–64 222, 2019.

[82] M. Doumpos, C. Zopounidis, and E. Galariotis, "Inferring robust decision models in multicriteria classification problems: An experimental analysis," *European Journal of Operational Research*, vol. 236, no. 2, pp. 601–611, 2014.

[83] H. Wu, W. Wang, H. Ye, and Z. Wang, "State estimation for Markovian jump linear systems with bounded disturbances," *Automatica*, vol. 49, no. 11, pp. 3292–3303, 2013.

[84] M. Jordan, J. Lewis, and A. G. Dimakis, "Provable certificates for adversarial examples: Fitting a ball in the union of polytopes," *arXiv preprint arXiv:1903.08778*, 2019.

[85] J. C. Maxwell, "L. on the calculation of the equilibrium and stiffness of frames," *The London, Edinburgh, and Dublin Philosophical Magazine and Journal of Science*, vol. 27, no. 182, pp. 294–299, 1864.

[86] S. Pellegrino and C. R. Calladine, "Matrix analysis of statically and kinematically indeterminate frameworks," *International Journal of Solids and Structures*, vol. 22, no. 4, pp. 409–428, 1986.

[87] M. von Scheven, E. Ramm, and M. Bischoff, "Quantification of the redundancy distribution in truss and beam structures," *International Journal of Solids and Structures*, vol. 213, pp. 41–49, 2021.

[88] A. Eriksson and A. G. Tibert, "Redundant and force-differentiated systems in engineering and nature," *Computer Methods in Applied Mechanics and Engineering*, vol. 195, no. 41-43, pp. 5437–5453, 2006.

[89] F. Biondini, D. M. Frangopol, and S. Restelli, "On structural robustness, redundancy, and static indeterminacy," in *Structures Congress 2008: Crossing Borders*, 2008, pp. 1–10.

[90] J. Quirant, "Selfstressed systems comprising elements with unilateral rigidity: Selfstress states, mechanisms and tension setting," *International Journal of Space Structures*, vol. 22, no. 4, pp. 203–214, 2007.

[91] J. Quirant, K. Aoual, and R. Laporte, "Tensegrity systems: The application of linear programmation in search of compatible selfstress states," *Journal of the International Association for Shell and Spatial Structures*, vol. 44, no. 1, pp. 33–50, 2003.

[92] G. M. Ziegler, *Lectures on polytopes*. Springer Science & Business Media, 2012, vol. 152.

[93] K. Fukuda, "Frequently asked questions in polyhedral computation," *ETH, Zurich, Switzerland*, 2004.

[94] K. Fukuda and A. Prodon, "Double description method revisited," in *Franco-Japanese and Franco-Chinese Conference on Combinatorics and Computer Science*, Springer, 1995, pp. 91–111.

[95] D. Avis and K. Fukuda, "Reverse search for enumeration," *Discrete Applied Mathematics*, vol. 65, no. 1-3, pp. 21–46, 1996.

[96] D. Avis and K. Fukuda, "A pivoting algorithm for convex hulls and vertex enumeration of arrangements and polyhedra," *Discrete & Computational Geometry*, vol. 8, no. 3, pp. 295–313, 1992.

[97] P. McMullen, "The maximum numbers of faces of a convex polytope," *Mathematika*, vol. 17, no. 2, pp. 179–184, 1970.

[98] M. M. Bayer *et al.*, "Combinatorial aspects of convex polytopes," in *Handbook of convex geometry*, Elsevier, 1993, pp. 485–534.

[99] J. V. Burke and J. J. Moré, "On the identification of active constraints," *SIAM Journal on Numerical Analysis*, vol. 25, no. 5, pp. 1197–1211, 1988.

[100] C. Davis, "Theory of positive linear dependence," *American Journal of Mathematics*, vol. 76, no. 4, pp. 733–746, 1954.

[101] J. Dattorro, *Convex optimization & Euclidean distance geometry*. Meboo Publishing, 2010.

[102] Z. Guo, T. Tachi, and H. Yu, "Folding process planning of rigid origami using the explicit expression and rapidly exploring random tree method," *Journal of Mechanisms and Robotics*, pp. 1–51, 2021.

[103] D. Avis, *Lrslib*, 2021. [Online]. Available: `http://cgm.cs.mcgill.ca/~avis/C/lrs.html`.

[104] K. Fukuda, "Cdd/cdd+ reference manual," *Institute for Operations Research, ETH-Zentrum*, pp. 91–111, 1997.

[105] R. Schaich, *Geocalclib: A matlab interface for the lrs library*, 2018. [Online]. Available: `http://worc4021.github.io/`.

[106] MOSEK ApS, *The MOSEK optimization toolbox for MATLAB manual. Version 9.0.* 2019. [Online]. Available: `http://docs.mosek.com/9.0/toolbox/index.html`.

[107] D. Avis and C. Jordan, "Mplrs: A scalable parallel vertex/facet enumeration code," *Mathematical Programming Computation*, vol. 10, no. 2, pp. 267–302, 2018.

[108] D. Avis and L. Devroye, "Estimating the number of vertices of a polyhedron," *Information Processing Letters*, vol. 73, no. 3-4, pp. 137–143, 2000.

[109] D. Avis, D. Bremner, and R. Seidel, "How good are convex hull algorithms?" *Computational Geometry*, vol. 7, no. 5-6, pp. 265–301, 1997.

[110] V. Parenti-Castelli and S. Venanzi, "Clearance influence analysis on mechanisms," *Mechanism and Machine Theory*, vol. 40, no. 12, pp. 1316–1329, 2005.

[111] M.-J. Tsai and T.-H. Lai, "Accuracy analysis of a multi-loop linkage with joint clearances," *Mechanism and Machine Theory*, vol. 43, no. 9, pp. 1141–1157, 2008.

[112] S. Dubowsky, M. Norris, E. Aloni, and A. Tamir, "An analytical and experimental study of the prediction of impacts in planar mechanical systems with clearances," *Journal of Mechanisms, Transmissions, and Automation in Design*, vol. 106, no. 4, pp. 444–451, 1984.

[113] K. Liu, L. S. Novelino, P. Gardoni, and G. H. Paulino, "Big influence of small random imperfections in origami-based metamaterials," *Proceedings of the Royal Society A*, vol. 476, no. 2241, p. 20 200 236, 2020.

[114] J. Cai, R. Yang, X. Wang, and J. Feng, "Effect of initial imperfections of struts on the mechanical behavior of tensegrity structures," *Composite Structures*, vol. 207, pp. 871–876, 2019.

[115] M. Schenk and S. D. Guest, "Origami folding: A structural engineering approach," *Origami*, vol. 5, pp. 291–304, 2011.

[116] K. Liu and G. Paulino, "Nonlinear mechanics of non-rigid origami: An efficient computational approach," *Proceedings of the Royal Society A: Mathematical, Physical and Engineering Sciences*, vol. 473, no. 2206, p. 20 170 348, 2017.

[117] S. Pellegrino, "Structural computations with the singular value decomposition of the equilibrium matrix," *International Journal of Solids and Structures*, vol. 30, no. 21, pp. 3025–3035, 1993.

[118] T. Tachi, "Simulation of rigid origami," *Origami*, vol. 4, no. 08, pp. 175–187, 2009.

[119] E. A. P. Hernandez, D. J. Hartl, and D. C. Lagoudas, *Active Origami: modeling, design, and applications*. Springer, 2018.

[120] Y. Li, "Motion paths finding for multi-degree-of-freedom mechanisms," *International Journal of Mechanical Sciences*, p. 105 709, 2020.

Appendix A

PLATE-HINGE KINEMATICS

The kinematics of structures composed of rigid plates connected by hinges can be captured by a set of bilateral constraints representing pin-jointed rigid bars [48, 115]. To develop a set of kinematic constraints, the edges of each plate are treated as rigid bars. Then, rigid bars are added to triangulate any non-triangular plate, as illustrated in Figure A.1. The bars added to triangulate plates are treated as fixed hinges to ensure that the plates remain planar. The corresponding set of bilateral constraints is

$$\boldsymbol{h}(\boldsymbol{x}) = \boldsymbol{0}, \tag{A.1}$$

where

$$h_i(\boldsymbol{x}) = \begin{cases} L_i(\boldsymbol{x}) - L_{0i} & i = 1, ..., n_B \\ \varphi_i(\boldsymbol{x}) & i = n_B + 1, ..., n_B + n_H. \end{cases} \tag{A.2}$$

The plate-hinge structure containing n vertices is parameterized by vertex coordinates $\boldsymbol{x} \in \mathbb{R}^{3n}$. The lengths $\boldsymbol{L} \in \mathbb{R}^{n_B}$ of the n_B bars are fixed at $\boldsymbol{L}_0 \in \mathbb{R}^{n_B}$, enforcing that the bars are inextensible. The rotations $\boldsymbol{\varphi} \in \mathbb{R}^{n_H}$ about the n_H bars added to triangulate the non-triangular plates are restricted to zero. The total number of bilateral constraints is $n_b = n_B + n_H$.

The bilateral constraint gradients $\boldsymbol{C}^b \in \mathbb{R}^{n_b \times 3n}$, which form the compatibility matrix of the bilateral constraints, are given by

$$\boldsymbol{C}^b = \frac{\partial \boldsymbol{h}}{\partial \boldsymbol{x}} = \begin{bmatrix} \dfrac{\partial \boldsymbol{l}}{\partial \boldsymbol{x}} \\ \dfrac{\partial \boldsymbol{\varphi}}{\partial \boldsymbol{x}} \end{bmatrix}. \tag{A.3}$$

The gradients of bar lengths and hinge rotations with respect to $\boldsymbol{x}$ make up $\boldsymbol{C}^b$.

To define the gradients of the bar lengths, consider bar k with length L_k whose endpoints are defined by $\boldsymbol{x}_i = [x_i \; y_i \; z_i]^T$ and $\boldsymbol{x}_j = [x_j \; y_j \; z_j]^T$. The gradient of the

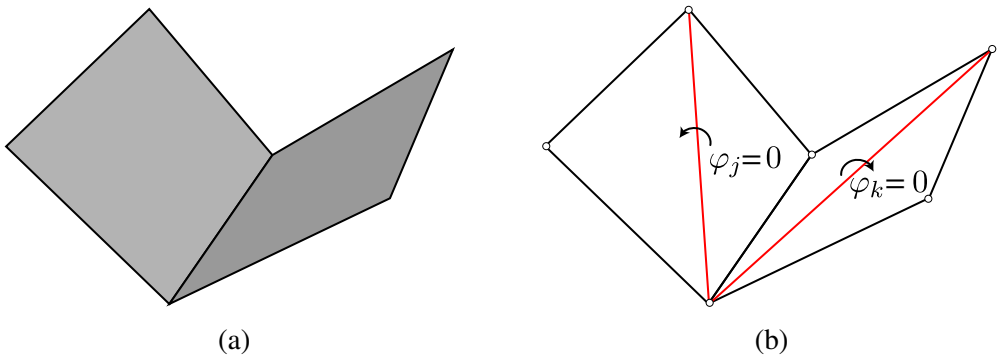

Figure A.1: Pin-jointed bar model for plate-hinge kinematics. (a) A hinge connecting two quadrilateral plates. (b) The equivalent pin-jointed bar model of the plates. The red lines represent bars added to triangulate the two plates. The bilateral constraints enforce that all bars, including both the black and red segments, have fixed lengths and that the angles about the added bars, shown in red, remain at zero.

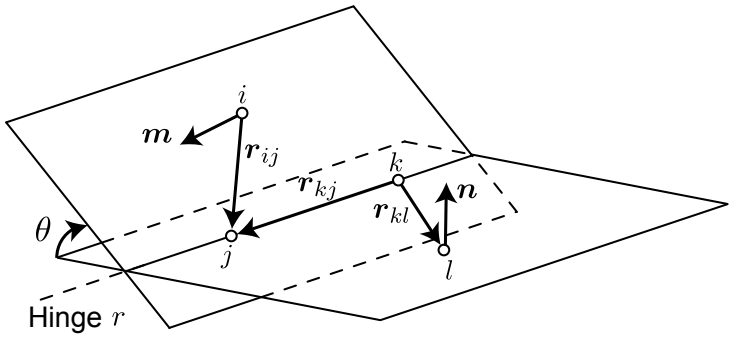

Figure A.2: Diagram of a hinge for defining angle gradients, based on [116].

length of the bar with respect to its endpoints is

$$\frac{\partial L_k}{\partial x_i} = \begin{bmatrix} \dfrac{x_i - x_j}{L_k} & \dfrac{y_i - y_j}{L_k} & \dfrac{z_i - z_j}{L_k} \end{bmatrix} \tag{A.4}$$

$$\frac{\partial L_k}{\partial x_j} = \begin{bmatrix} \dfrac{x_j - x_i}{L_k} & \dfrac{y_j - y_i}{L_k} & \dfrac{z_j - z_i}{L_k} \end{bmatrix}. \tag{A.5}$$

The gradients of L_k with respect the endpoints of bar k represent the only nonzero entries in row k of $\boldsymbol{C}^b$.

The gradients of the angle of a hinge are defined with respect to four points that define the hinge. Consider a general hinge r in three-dimensional space, as shown in Figure A.2. Four points can be used to define the hinge. Points $\boldsymbol{x}_j$ and $\boldsymbol{x}_k$ are two points that define the rotation axis of the hinge while points $\boldsymbol{x}_i$ and $\boldsymbol{x}_l$ each lie on one of the plates that intersect at the hinge. The gradient of hinge angle with respect

to these four points, which is derived in [116], takes the form

$$\frac{\partial \theta}{\partial \boldsymbol{x}_i} = -\frac{\|\boldsymbol{r}_{kj}\|}{\|\boldsymbol{m}\|^2}\boldsymbol{m}, \tag{A.6}$$

$$\frac{\partial \theta}{\partial \boldsymbol{x}_l} = \frac{\|\boldsymbol{r}_{kj}\|}{\|\boldsymbol{n}\|^2}\boldsymbol{n}, \tag{A.7}$$

$$\frac{\partial \theta}{\partial \boldsymbol{x}_j} = -\left(\frac{\boldsymbol{r}_{ij}\cdot\boldsymbol{r}_{kj}}{\|\boldsymbol{r}_{kj}\|^2} - 1\right)\frac{\partial \theta}{\partial \boldsymbol{x}_i} + \frac{\boldsymbol{r}_{kl}\cdot\boldsymbol{r}_{kj}}{\|\boldsymbol{r}_{kj}\|^2}\frac{\partial \theta}{\partial \boldsymbol{x}_l}, \tag{A.8}$$

$$\frac{\partial \theta}{\partial \boldsymbol{x}_k} = -\left(\frac{\boldsymbol{r}_{kl}\cdot\boldsymbol{r}_{kj}}{\|\boldsymbol{r}_{kj}\|^2} - 1\right)\frac{\partial \theta}{\partial \boldsymbol{x}_l} + \frac{\boldsymbol{r}_{ij}\cdot\boldsymbol{r}_{kj}}{\|\boldsymbol{r}_{kj}\|^2}\frac{\partial \theta}{\partial \boldsymbol{x}_i}, \tag{A.9}$$

where $\boldsymbol{r}_{pq} = \boldsymbol{x}_p - \boldsymbol{x}_q$ and the normal vectors $\boldsymbol{m}$ and $\boldsymbol{n}$ are given by $\boldsymbol{m} = \boldsymbol{r}_{ij} \times \boldsymbol{r}_{kj}$ and $\boldsymbol{n} = \boldsymbol{r}_{kj} \times \boldsymbol{r}_{kl}$. Here, we adopt the convention of [48] for defining the hinge angle. Equations (A.6)-(A.9) can be used to compute the components of $\boldsymbol{C}^b$ associated with the fixed hinges.

Using the compatibility matrix, the linearized bilateral constraints about a configuration $\boldsymbol{x}_t$ take the form

$$\boldsymbol{C}^b\boldsymbol{d} = \boldsymbol{0}, \tag{A.10}$$

where $\boldsymbol{d} = \boldsymbol{x} - \boldsymbol{x}_t \in \mathbb{R}^{3n}$ is a displacement of the vertices and the gradients that define the compatibility matrix are evaluated at $\boldsymbol{x}_t$.

The singular value decomposition (SVD) of the compatibility matrix can be utilized to compute its null-space, which gives the first-order compatible directions, or the mechanisms of the structure [117]. The SVD is given by

$$\begin{bmatrix}\boldsymbol{C}^b \\ \boldsymbol{C}^h\end{bmatrix} = \boldsymbol{U}\boldsymbol{V}\boldsymbol{W}^T. \tag{A.11}$$

The right singular vector matrix $\boldsymbol{W}$ is composed of two sub-matrices

$$\boldsymbol{W} = \begin{bmatrix}\boldsymbol{W}_{r_c} & \boldsymbol{W}_m\end{bmatrix} \tag{A.12}$$

where $\boldsymbol{W}_{r_c}$ has r_c columns and r_c is the rank of the compatibility matrix. The matrix $\boldsymbol{W}_m$ has m columns, which form an orthogonal basis of the m-dimensional null space of the compatibility matrix. The number of kinematic degrees of freedom is defined as m, which corresponds to the number of linear mechanisms of the structure.

Appendix B

KINEMATIC PATHFINDING

A kinematic simulation framework for multi-DOF plate-hinge structures is formulated in the context of the bar-hinge model of Appendix A. A pathfinding algorithm is outlined, which can simulate reconfiguration of a fold pattern between target configurations.

The objective of the kinematic simulations is to verify that a path exists between target configurations of a fold pattern corresponding to different target surfaces. To simulate rigid folding between configurations, a kinematic pathfinding algorithm is outlined. Several pathfinding techniques have been developed to simulate rigid folding of origami [118–120]. Specifically, we follow the work of [120] to perform pathfinding simulations.

In the problem at hand, the initial configuration of the pattern $\boldsymbol{x}^1$ is known, which contains all vertex coordinates of the fold pattern, including both the tile and sub-fold vertices. A path is sought from $\boldsymbol{x}^1$ to a configuration with target tile vertex coordinates $\boldsymbol{v}_t \in \mathbb{R}^{3n_{vt}}$.

A step toward the target tile vertices is given by

$$\boldsymbol{d}^i_j = \begin{cases} (\boldsymbol{v}_t)_j - \boldsymbol{x}^i_j & j \leq n_{vt} \\ 0 & j > n_{vt}. \end{cases} \tag{B.1}$$

Here, $\boldsymbol{d}^i$ is a displacement of only the vertices on the tiles. By project $\boldsymbol{d}^i$ onto the null space of the compatibility matrix, a first-order-compatible displacement is

$$\boldsymbol{d}^i_m = \boldsymbol{W}_m|_i (\boldsymbol{W}_m)^T_i \boldsymbol{d}^i, \tag{B.2}$$

where $\boldsymbol{W}_m|_i$ is $\boldsymbol{W}_m$ evaluated at configuration $\boldsymbol{x}^i$. Finally, an incremental step toward the target surface that satisfies the linearized constraints is

$$\tilde{\boldsymbol{x}}^{i+1} = \boldsymbol{x}^i + \eta \hat{\boldsymbol{d}}^i_m, \tag{B.3}$$

where

$$\hat{\boldsymbol{d}}^i_m = \frac{\boldsymbol{d}^i_m}{||\boldsymbol{d}^i_m||} \tag{B.4}$$

and η is the step size. Since the step is taken within the space of linear mechanisms, it will induce higher order errors in the bilateral constraints. Correction steps can iteratively be applied until the constraints of Eq. (A.2) are satisfied. The correction step is taken orthogonal to the null space of the compatibility matrix,

$$\boldsymbol{d}_c(\tilde{\boldsymbol{x}}^{i+1}) = -\boldsymbol{W}_{rc}|_i \, (\boldsymbol{V}_{rc})_i^{-1} \, (\boldsymbol{U}_{rc})_i^T \begin{bmatrix} \boldsymbol{e}(\tilde{\boldsymbol{x}}^{i+1}) \\ \varphi(\tilde{\boldsymbol{x}}^{i+1}) \end{bmatrix} \tag{B.5}$$

where $\boldsymbol{e} = \boldsymbol{L} - \boldsymbol{L}_0$ is the extension of the bars.

A pathfinding algorithm is summarized in Algorithm 1. The algorithm returns a set of configurations $\{\boldsymbol{x}^i\}$ along the path from the initial configuration to the final target configuration.

Algorithm 1 Kinematic pathfinding algorithm

while $||\boldsymbol{d}^i|| > \epsilon_1$ **do**
  Compute $\hat{\boldsymbol{d}}_m^i$ from Eqs. (B.2)-(B.4)
  $\tilde{\boldsymbol{x}}_{i+1} \leftarrow \boldsymbol{x}_i + \eta \hat{\boldsymbol{d}}_m^i$
  while $\left\| \begin{bmatrix} \boldsymbol{e} \\ \varphi \end{bmatrix} \right\| > \epsilon_2$ **do**
    $\tilde{\boldsymbol{x}}_{i+1} \leftarrow \tilde{\boldsymbol{x}}_{i+1} + \boldsymbol{d}_c(\tilde{\boldsymbol{x}}_{i+1})$
    $\boldsymbol{e} \leftarrow \boldsymbol{L}(\tilde{\boldsymbol{x}}_{i+1}) - \boldsymbol{L}_0$
    $\varphi \leftarrow \varphi(\tilde{\boldsymbol{x}}_{i+1})$
  end while return $\boldsymbol{x}_{i+1} = \tilde{\boldsymbol{x}}_{i+1}$
  $i \leftarrow i + 1$
end while

The outer while loop increments the steps along the path, terminating when the configuration is within a tolerance ϵ_1 of target tile vertex coordinates. The inner while loop iteratively applies correction steps until the bilateral constraints are satisfied within tolerance ϵ_2.

Appendix C

2-DOF LINKAGE MATRIX COMPUTATIONS

This appendix supplies details on the computation of the matrices supporting the 2-DOF linkage example. The bilateral constraints of Eq. (4.58) take the form of fixed-length bar constraints. The gradients of bar lengths, also known as the compatibility matrix of the bars, takes the form

$$\boldsymbol{C}^b = \frac{\partial \boldsymbol{L}}{\partial \boldsymbol{x}} = \begin{bmatrix} \frac{x_2}{L_1} & \frac{y_2}{L_1} & 0 & 0 & 0 & 0 \\ \frac{x_2-x_3}{L_2} & \frac{y_2-y_3}{L_1} & \frac{x_3-x_2}{L_2} & \frac{y_3-y_2}{L_1} & 0 & 0 \\ 0 & 0 & \frac{x_3-x_4}{L_3} & \frac{y_3-y_4}{L_3} & \frac{x_4-x_3}{L_3} & \frac{y_4-y_3}{L_3} \\ 0 & 0 & 0 & 0 & \frac{x_4}{L_4} & \frac{y_4}{L_4} \end{bmatrix}. \tag{C.1}$$

When evaluated in the four target configurations, the compatibility matrix of the bars takes the values

$$\begin{aligned} \boldsymbol{C}^b|_1 &= \begin{bmatrix} 0.7071 & 0.7071 & 0 & 0 & 0 & 0 \\ -0.7071 & 0.7071 & 0.7071 & -0.7071 & 0 & 0 \\ 0 & 0 & -0.7071 & -0.7071 & 0.7071 & 0.7071 \\ 0 & 0 & 0 & 0 & -0.7071 & 0.7071 \end{bmatrix} \\ \boldsymbol{C}^b|_2 &= \begin{bmatrix} 1 & 0 & 0 & 0 & 0 & 0 \\ -0.4728 & 0.8812 & 0.4728 & -0.8812 & 0 & 0 \\ 0 & 0 & -0.4728 & -0.8812 & 0.4728 & 0.8812 \\ 0 & 0 & 0 & 0 & -1 & 0 \end{bmatrix} \\ \boldsymbol{C}^b|_3 &= \begin{bmatrix} 0.7071 & 0.7071 & 0 & 0 & 0 & 0 \\ -0.2630 & 0.9648 & 0.2630 & -0.9648 & 0 & 0 \\ 0 & 0 & -0.9169 & -0.3991 & 0.9169 & 0.3991 \\ 0 & 0 & 0 & 0 & -1 & 0 \end{bmatrix} \\ \boldsymbol{C}^b|_4 &= \begin{bmatrix} 1 & 0 & 0 & 0 & 0 & 0 \\ -0.9169 & 0.3991 & 0.9169 & -0.3991 & 0 & 0 \\ 0 & 0 & -0.2630 & -0.9648 & 0.2630 & 0.9648 \\ 0 & 0 & 0 & 0 & -0.7071 & 0.7071 \end{bmatrix}, \end{aligned} \tag{C.2}$$

where $\boldsymbol{C}^b|_i$ denotes the bar compatibility matrix evaluated in configuration i.

Orthonormal bases for the null spaces of $\boldsymbol{C}^b|_1$, $\boldsymbol{C}^b|_2$, $\boldsymbol{C}^b|_3$, and $\boldsymbol{C}^b|_4$ are computed as

$$\begin{aligned}
\boldsymbol{W}_m|_1 &= \begin{bmatrix} 0.4512 & -0.2155 \\ -0.4512 & 0.2155 \\ 0.6667 & 0.2357 \\ -0.2357 & 0.6667 \\ 0.2155 & 0.4512 \\ 0.2155 & 0.4512 \end{bmatrix} & \boldsymbol{W}_m|_2 &= \begin{bmatrix} 0 & 0 \\ -0.7166 & 0.0498 \\ 0.5172 & 0.6059 \\ -0.4391 & 0.3749 \\ 0 & 0 \\ -0.1616 & 0.6999 \end{bmatrix} \\
\boldsymbol{W}_m|_3 &= \begin{bmatrix} 0.5290 & -0.0548 \\ -0.5290 & 0.0548 \\ 0.2864 & 0.3331 \\ -0.5952 & 0.1605 \\ 0 & 0 \\ 0.0627 & 0.9259 \end{bmatrix} & \boldsymbol{W}_m|_4 &= \begin{bmatrix} 0 & 0 \\ 0.4302 & -0.8223 \\ 0.0702 & 0.4337 \\ 0.5914 & 0.1741 \\ 0.4797 & 0.2297 \\ 0.4797 & 0.2297 \end{bmatrix},
\end{aligned} \tag{C.3}$$

where each have $m = 2$ columns corresponding to the two mechanisms of the linkage. Note that this choice for the basis of the mechanisms is not unique. The gradients of the unilateral constraints of Eq. (4.59) must be defined separately for each target configuration since each configuration has different active unilateral constraints. In each target configuration, the gradients of the active unilateral constraints are

$$\begin{aligned}
\boldsymbol{C}^u|_1 &= \begin{bmatrix} \frac{\partial\theta_1}{\partial x_2} & \frac{\partial\theta_1}{\partial y_2} & 0 & 0 & 0 & 0 \\ 0 & 0 & 0 & 0 & \frac{\partial\theta_5}{\partial x_4} & \frac{\partial\theta_5}{\partial y_4} \end{bmatrix}_1 \\
\boldsymbol{C}^u|_2 &= \begin{bmatrix} -\frac{\partial\theta_1}{\partial x_2} & -\frac{\partial\theta_1}{\partial y_2} & 0 & 0 & 0 & 0 \\ 0 & 0 & 0 & 0 & -\frac{\partial\theta_5}{\partial x_4} & -\frac{\partial\theta_5}{\partial y_4} \end{bmatrix}_2 \\
\boldsymbol{C}^u|_3 &= \begin{bmatrix} \frac{\partial\theta_1}{\partial x_2} & \frac{\partial\theta_1}{\partial y_2} & 0 & 0 & 0 & 0 \\ 0 & 0 & 0 & 0 & -\frac{\partial\theta_5}{\partial x_4} & -\frac{\partial\theta_5}{\partial y_4} \end{bmatrix}_3 \\
\boldsymbol{C}^u|_4 &= \begin{bmatrix} -\frac{\partial\theta_1}{\partial x_2} & -\frac{\partial\theta_1}{\partial y_2} & 0 & 0 & 0 & 0 \\ 0 & 0 & 0 & 0 & \frac{\partial\theta_5}{\partial x_4} & \frac{\partial\theta_5}{\partial y_4} \end{bmatrix}_4.
\end{aligned} \tag{C.4}$$

To evaluate the active unilateral constraint gradients, the derivative of an angle with respect to the points that define the angle must be computed. In the two-dimensional setting, Figure C.1 defines three points, $\boldsymbol{p}_1$, $\boldsymbol{p}_2$, and $\boldsymbol{p}_3$, which define the angle θ. The unit normal vectors to segments $\boldsymbol{p}_1\boldsymbol{p}_2$ and $\boldsymbol{p}_2\boldsymbol{p}_3$ are $\hat{\boldsymbol{N}}_{12}$ and $\hat{\boldsymbol{N}}_{23}$, respectively. The derivative of θ with respect to the points $\boldsymbol{p}_1$, $\boldsymbol{p}_2$, and $\boldsymbol{p}_3$ are given by

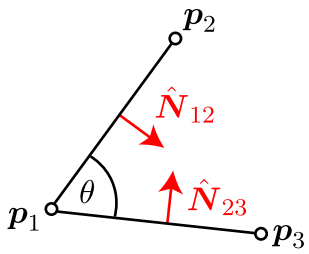

Figure C.1: Definitions for computation of the gradient of a hinge angle with respect the points that define the hinge in two dimensions.

$$\frac{\partial \theta}{\partial \boldsymbol{p}_1} = -\frac{\hat{\boldsymbol{N}}_{12}}{||\boldsymbol{p}_1\boldsymbol{p}_2||} - \frac{\hat{\boldsymbol{N}}_{23}}{||\boldsymbol{p}_2\boldsymbol{p}_3||} \tag{C.5}$$

$$\frac{\partial \theta}{\partial \boldsymbol{p}_2} = \frac{\hat{\boldsymbol{N}}_{12}}{||\boldsymbol{p}_1\boldsymbol{p}_2||} \tag{C.6}$$

$$\frac{\partial \theta}{\partial \boldsymbol{p}_3} = \frac{\hat{\boldsymbol{N}}_{23}}{||\boldsymbol{p}_2\boldsymbol{p}_3||}. \tag{C.7}$$

These equations for hinge angle gradients represent a simplified version of Eqs. (A.6)-(A.9) for the two-dimensional setting. Equations (C.6) and (C.7) allow the active unilateral constraint gradients to be evaluated in the four target configurations. By inserting numerical values for each configuration, we obtain

$$\begin{aligned}
\boldsymbol{C}^u|_1 &= \begin{bmatrix} -0.0094 & 0.0094 & 0 & 0 & 0 & 0 \\ 0 & 0 & 0 & 0 & 0.0094 & 0.0094 \end{bmatrix} \\
\boldsymbol{C}^u|_2 &= \begin{bmatrix} 0 & -0.0133 & 0 & 0 & 0 & 0 \\ 0 & 0 & 0 & 0 & 0 & -0.0133 \end{bmatrix} \\
\boldsymbol{C}^u|_3 &= \begin{bmatrix} -0.0094 & 0.0094 & 0 & 0 & 0 & 0 \\ 0 & 0 & 0 & 0 & 0 & -0.0133 \end{bmatrix} \\
\boldsymbol{C}^u|_4 &= \begin{bmatrix} 0 & -0.0133 & 0 & 0 & 0 & 0 \\ 0 & 0 & 0 & 0 & 0.0094 & 0.0094 \end{bmatrix}.
\end{aligned} \tag{C.8}$$

Now, the matrix $\boldsymbol{A} = \boldsymbol{W}_m^T \boldsymbol{C}^{uT}$ can be computed in each configuration,

$$\begin{aligned}
\boldsymbol{A}|_1 &= \begin{bmatrix} -0.0085 & 0.0041 \\ 0.0041 & 0.0085 \end{bmatrix} \qquad \boldsymbol{A}|_2 = \begin{bmatrix} 0.0096 & 0.0022 \\ -0.0007 & -0.0093 \end{bmatrix} \\
\boldsymbol{A}|_3 &= \begin{bmatrix} -0.0100 & -0.0008 \\ 0.0010 & -0.0123 \end{bmatrix} \qquad \boldsymbol{A}|_4 = \begin{bmatrix} -0.0057 & 0.0090 \\ 0.0110 & 0.0043 \end{bmatrix}.
\end{aligned} \tag{C.9}$$

The normal vectors to the polyhedral cone that defines the rigidity conditions, which are the rows of $\boldsymbol{A}^{-1}$, are

$$\begin{aligned}
\boldsymbol{A}^{-1}|_1 &= \begin{bmatrix} \boldsymbol{n}_1^T|_1 \\ \boldsymbol{n}_2^T|_1 \end{bmatrix} = \begin{bmatrix} -95.7107 & 45.7107 \\ 45.7107 & 95.7107 \end{bmatrix} \\
\boldsymbol{A}^{-1}|_2 &= \begin{bmatrix} \boldsymbol{n}_1^T|_2 \\ \boldsymbol{n}_2^T|_2 \end{bmatrix} = \begin{bmatrix} 106.3629 & 24.5553 \\ -7.5637 & -108.8982 \end{bmatrix} \\
\boldsymbol{A}^{-1}|_3 &= \begin{bmatrix} \boldsymbol{n}_1^T|_3 \\ \boldsymbol{n}_2^T|_3 \end{bmatrix} = \begin{bmatrix} -99.5437 & 6.7458 \\ -8.3288 & -80.4400 \end{bmatrix} \\
\boldsymbol{A}^{-1}|_4 &= \begin{bmatrix} \boldsymbol{n}_1^T|_4 \\ \boldsymbol{n}_2^T|_4 \end{bmatrix} = \begin{bmatrix} -34.9212 & 72.9415 \\ 88.4042 & 46.2510 \end{bmatrix}.
\end{aligned} \tag{C.10}$$

Finally, we can define the compatibility matrix of the springs $\boldsymbol{C}^s$, introduced in Eq. (4.34). Since this example has only torsion springs, the spring compatibility matrix contains the derivatives of the hinge angles with respect to the vertex coordinates. It is given by

$$\boldsymbol{C}^s = \frac{\partial \boldsymbol{\theta}}{\partial \boldsymbol{x}} = \begin{bmatrix}
\frac{\partial \theta_1}{\partial x_2} & \frac{\partial \theta_1}{\partial y_2} & 0 & 0 & 0 & 0 \\
\frac{\partial \theta_2}{\partial x_2} & \frac{\partial \theta_2}{\partial y_2} & \frac{\partial \theta_2}{\partial x_3} & \frac{\partial \theta_2}{\partial y_3} & 0 & 0 \\
\frac{\partial \theta_3}{\partial x_2} & \frac{\partial \theta_3}{\partial y_2} & \frac{\partial \theta_3}{\partial x_3} & \frac{\partial \theta_3}{\partial y_3} & \frac{\partial \theta_3}{\partial x_4} & \frac{\partial \theta_3}{\partial y_4} \\
0 & 0 & \frac{\partial \theta_4}{\partial x_3} & \frac{\partial \theta_4}{\partial y_3} & \frac{\partial \theta_4}{\partial x_4} & \frac{\partial \theta_4}{\partial y_4} \\
0 & 0 & 0 & 0 & \frac{\partial \theta_5}{\partial x_4} & \frac{\partial \theta_5}{\partial y_4}
\end{bmatrix}. \tag{C.11}$$

Using the identities of Eqs. (C.5), (C.6), and (C.7), the derivatives of angles with respect to the vertex coordinates can be evaluated as

$$
\begin{aligned}
\boldsymbol{C}^s|_1 &= \begin{bmatrix} -0.0094 & 0.0094 & 0 & 0 & 0 & 0 \\ 0.0019 & -0.0170 & 0.0075 & 0.0075 & 0 & 0 \\ -0.0075 & -0.0075 & 0 & 0.0151 & 0.0075 & -0.0075 \\ 0 & 0 & -0.0075 & 0.0075 & -0.0019 & -0.0170 \\ 0 & 0 & 0 & 0 & 0.0094 & 0.0094 \end{bmatrix} \\
\boldsymbol{C}^s|_2 &= \begin{bmatrix} 0.0000 & 0.0133 & 0 & 0 & 0 & 0 \\ -0.0094 & -0.0184 & 0.0094 & 0.0050 & 0 & 0 \\ -0.0094 & -0.0050 & 0 & 0.0101 & 0.0094 & -0.0050 \\ 0 & 0 & -0.0094 & 0.0050 & 0.0094 & -0.0184 \\ 0 & 0 & 0 & 0 & 0 & 0.0133 \end{bmatrix} \\
\boldsymbol{C}^s|_3 &= \begin{bmatrix} -0.0094 & 0.0094 & 0 & 0 & 0 & 0 \\ -0.0009 & -0.0122 & 0.0103 & 0.0028 & 0 & 0 \\ -0.0103 & -0.0028 & 0.0060 & 0.0126 & 0.0043 & -0.0098 \\ 0 & 0 & -0.0043 & 0.0098 & 0.0043 & -0.0231 \\ 0 & 0 & 0 & 0 & 0 & 0.0133 \end{bmatrix} \\
\boldsymbol{C}^s|_4 &= \begin{bmatrix} 0 & 0.0133 & 0 & 0 & 0 & 0 \\ -0.0043 & -0.0231 & 0.0043 & 0.0098 & 0 & 0 \\ -0.0043 & -0.0098 & -0.0060 & 0.0126 & 0.0103 & -0.0028 \\ 0 & 0 & -0.0103 & 0.0028 & 0.0009 & -0.0122 \\ 0 & 0 & 0 & 0 & 0.0094 & 0.0094 \end{bmatrix}.
\end{aligned}
\tag{C.12}
$$